

# POLITECNICO DI TORINO

Master's Degree in AEROSPACE ENGINEERING



Master's Degree Thesis

## Experimental investigation of the aerodynamics performance of an Unmanned Aerial Vehicle rotorblade in non-ideal conditions

Supervisors

Prof. GIOACCHINO CAFIERO

Prof. GAETANO IUSO

Ing. ALESSANDRO GRAVA

Candidate

MARCO PICILLO

OCTOBER 2023

*I would like to dedicate this thesis to my loving parents*

## Acknowledgements

I would like to acknowledge Professors Gioacchino Cafiero, Jacopo Serpieri, Gaetano Iuso and Ph.D. student Alessandro Grava for giving me the opportunity to carry out this thesis in an exciting environment and for supporting me throughout the entire period spent in the laboratory.

But most of all I would like to thank Ph.D. student Enrico Amico for sharing his insatiable passion for engineering with me and for making me understand that there are two types of people: those who stay silent and work, and those who just talk.

## **Abstract**

The purpose of the Urban Air Mobility is to provide a safe and efficient transportation system to improve daily life in large urban contexts. The main applications can vary from air taxi to last-mile delivery. In this context drones open a wide range of new opportunities that were unthinkable decades ago, with applications that cover many fields, from military to agriculture and healthcare. The majority of the applications cited above are covered by means of small rotary-wing drones. These architectures are characterized by low thrust loading and poor efficiency due to the regime in which they operate, characterized by predominant viscous effects. For these reasons, in this thesis will be investigated both numerically, by means of CFD, and experimentally, by means of Particle Image Velocimetry (PIV) and load cells, the performance of a small-scale propeller in hover and in cross-flow in order to understand the mechanisms of performance degradation and the effects on the wake flowfield.

# Contents

<b>List of Figures</b>	<b>vii</b>
<b>List of Tables</b>	<b>xi</b>
<b>1 Introduction</b>	<b>1</b>
1.1 The role of drones in modern society . . . . .	2
1.2 Theoretical background . . . . .	4
1.2.1 Wake topology of propellers . . . . .	5
1.2.2 Rotors at low Reynolds number . . . . .	10
1.2.3 Numerical methods . . . . .	14
<b>2 Experimental and numerical setup</b>	<b>20</b>
2.1 Introduction . . . . .	20
2.2 Experimental setup . . . . .	20
2.3 Numerical setup . . . . .	24
<b>3 Wind tunnel characterization</b>	<b>31</b>
3.1 Introduction . . . . .	31
3.2 Ferrari wind tunnel . . . . .	32
3.3 Flow characteristics . . . . .	33
3.4 Considerations on the flow quality and model positioning . . . . .	42
<b>4 Results</b>	<b>44</b>
4.1 Introduction . . . . .	44
4.2 Hovering performance . . . . .	44

---

4.2.1	Thrust and Torque . . . . .	44
4.2.2	Wall flow features . . . . .	51
4.2.3	Wake topology . . . . .	57
4.3	Axial inflow performance . . . . .	63
4.3.1	Thrust and Torque . . . . .	63
4.3.2	Wall flow features . . . . .	68
4.4	Cross-flow performance . . . . .	70
4.4.1	Wake topology . . . . .	70
<b>5</b>	<b>Conclusions</b>	<b>73</b>
	<b>References</b>	<b>74</b>
	<b>Appendix A Images</b>	<b>76</b>

# List of Figures

1.1	Drones' classification [1]. . . . .	2
1.2	Drones' applications [1]. . . . .	3
1.3	Different types of MAVs. . . . .	4
1.4	Complexity of the wake of a drone in different configurations (iso-surfaces of Q-criterion) [2]. . . . .	5
1.5	Complexity of the wake of a drone in different configurations (velocity magnitude) [2]. . . . .	5
1.6	. . . . .	6
1.7	Counterrotating vortex [3]. . . . .	7
1.8	Tip vortex motion [4]. . . . .	7
1.9	Radial and axial displacement [5] (left), [6] (right). . . . .	8
1.10	Vortex pairing sequence [3]. . . . .	9
1.11	Relative magnitude of various aircraft [7]. . . . .	10
1.12	Airfoil separation characteristics at different Re [8]. . . . .	11
1.13	Effect of Re on airfoil lift to drag ratio [8]. . . . .	12
1.14	Airfoil lift to drag ratio [9]. . . . .	12
1.15	[10] . . . . .	14
1.16	Comparison between $k - \omega$ SST and $k - \omega$ SST-CC in predicting the tip vortex characteristics of a wing with a NACA 0012 airfoil [11]. . .	17
1.17	Multiple reference frame technique [12] (left) and computational domain [13] (right). . . . .	18
2.1	An example of a PIV apparatus. . . . .	21
2.2	Experimental setup. . . . .	22
2.3	. . . . .	22

2.4	X-Y is the interrogation plane. On the right the rotor setup. x-y is the body reference frame, fixed with the propeller. (1) propeller, (2) motor, (3) load cell, (4) torque cell, (5) servo. . . . .	23
2.5	Numerical domain and refinement regions. . . . .	25
2.6	Cartesian mesh. . . . .	27
2.7	Cartesian mesh. . . . .	27
2.8	Wall $Y^+$ values. . . . .	29
2.9	Mesh quality metrics. . . . .	29
2.10	Mesh independence study. . . . .	30
3.1	Ferrari wind tunnel . . . . .	32
3.2	Pressure and velocity correlations. . . . .	33
3.3	Schematic of the wind tunnel and reference system. (red: x, blue: z, green: y). . . . .	34
3.4	Position A and B of the hot wire probe in the test section. . . . .	34
3.5	Hot-wire probe operational distance range, in grey a schematic of the hot-wire probe. . . . .	35
3.6	Velocity profiles, position A (Purple: 500 rpm, orange: 900 rpm, blue: 1350 rpm, green: 1800 rpm). . . . .	37
3.7	Non-dimensional velocity profiles, position A (Purple: 500 rpm, orange: 900 rpm, blue: 1350 rpm, green: 1800 rpm). . . . .	37
3.8	Turbulence intensity profiles, position A (Purple: 500 rpm, orange: 900 rpm, blue: 1350 rpm, green: 1800 rpm). . . . .	38
3.9	Velocity profiles, position B (Purple: 500 rpm, orange: 900 rpm, blue: 1350 rpm, green: 1800 rpm). . . . .	39
3.10	Non-dimensional velocity profiles, position B (Purple: 500 rpm, orange: 900 rpm, blue: 1350 rpm, green: 1800 rpm). . . . .	39
3.11	Turbulence intensity profiles, position B (Purple: 500 rpm, orange: 900 rpm, blue: 1350 rpm, green: 1800 rpm). . . . .	40
3.12	Turbulence power spectra, position B (Purple: 500 rpm, orange: 900 rpm, blue: 1350 rpm, green: 1800 rpm). . . . .	41
3.13	Probability density function, 500 rpm. . . . .	41
3.14	Non-dimensional mean velocity profiles in center test section compared with propeller size. . . . .	42

4.1	Thrust and torque as a function of rotational speed. . . . .	45
4.2	Thrust and torque coefficients as a function of Reynolds number. . . . .	46
4.3	Blade element [14]. . . . .	46
4.4	$C_T$ (left) and $C_Q$ (right) distribution along the half-span. . . . .	47
4.5	Schematic of the method [15]. . . . .	48
4.6	Inflow angle in Hover for 5000 and 7000 rpm. . . . .	49
4.7	$C_l$ and $C_d$ distributions along the blade span for different rotational speed. . . . .	50
4.8	Power loading as a function of disk loading. . . . .	51
4.9	Wall shear stress, 2000 rpm. . . . .	52
4.10	Wall shear stress, 5000 rpm. . . . .	52
4.11	Wall shear stress, 7020 rpm. . . . .	53
4.12	Planes location along the blade span. . . . .	53
4.13	Wall shear stress (x direction) at the root. . . . .	53
4.14	Wall shear stress (x direction) at mid-span. . . . .	54
4.15	Wall shear stress (x direction) at the tip. . . . .	54
4.16	Separated flow region (black) on the upper surface. 1: 2000 rpm, 2: 3610 rpm, 3: 5000 rpm and 4: 7020 rpm. . . . .	55
4.17	Ratio between separated flow area and total upper surface area ( $A_s/A_u$ ) as a function of disk loading. . . . .	56
4.18	$A_s/A_u$ function of Reynolds number. . . . .	56
4.19	Mean axial velocity flow field (PIV). . . . .	57
4.20	Mean axial velocity flow field (PIV). . . . .	57
4.21	Mean axial velocity profiles. . . . .	58
4.22	Mean axial velocity profiles. . . . .	58
4.23	$U/U_{max}$ as a function of $x/R$ for a fixed $y/R$ coordinate equal to 0.3. . . . .	59
4.24	Mean out of plane vorticity field (PIV). . . . .	59
4.25	Mean out of plane vorticity field (PIV). . . . .	60
4.26	Mean out of plane vorticity profiles. Black square represent the maximum vorticity. . . . .	60

4.27 Mean out of plane vorticity profiles. Black square represent the maximum vorticity. . . . .	61
4.28 Reynolds stresses (PIV). . . . .	61
4.29 Reynolds stresses (PIV). . . . .	62
4.30 Thrust and torque coefficients as a function of the advance ratio. . . .	63
4.31 Efficiency of the propeller. . . . .	64
4.32 Thrust and torque coefficients along the blade as a function of the advance ratio (CFD). . . . .	65
4.33 Thrust and torque coefficients along the blade as a function of the advance ratio (CFD). . . . .	65
4.34 Axial velocity interpolation, hover (left), $J=0.24$ right. . . . .	66
4.35 Axial velocity interpolation, $J=0.47$ . . . . .	66
4.36 Inflow angle . . . . .	67
4.37 $C_l$ and $C_d$ distributions along the blade span for different $J$ . . . . .	67
4.38 Wall shear stress for $J=0$ (left) and $J=0.24$ (right) at 5000 rpm. . . .	68
4.39 Wall shear stress for $J=0.47$ (left) and $J=0.71$ (right) at 5000 rpm. . .	68
4.40 Separated flow regions (black) at 5000 rpm. 1: $J=0$ , 2: $J=0.24$ , 3: $J=0.47$ , 4: $J=0.71$ . . . . .	69
4.41 Effect of $J$ on separated flow regions and $C_Q$ . . . . .	69
4.42 Mean axial velocity flow field (PIV), 1 m/s cross-flow. . . . .	70
4.43 Mean axial velocity flow field (PIV), 1 m/s cross-flow. . . . .	70
4.44 Mean axial velocity flow field (PIV), 3 m/s cross-flow. . . . .	71
4.45 Mean axial velocity flow field (PIV), 3 m/s cross-flow. . . . .	71
4.46 Mean axial velocity profiles, 3 m/s cross-flow. . . . .	72
4.47 Mean axial velocity profiles, 3 m/s cross-flow. . . . .	72
A.1 Representative flow visualization of the rotor wake in hover [16]. . . .	77

# List of Tables

2.1	Stationary domain analysis (D=0.1524 m). . . . .	26
2.2	Rotating domain analysis (D=0.1524 m). . . . .	26
2.3	Mesh base size (c=0.011304 m). . . . .	27
2.4	Mesh independence study. . . . .	29
3.1	Reynolds numbers (D = 40 cm). . . . .	36
3.2	Summary of the flow characteristics in A . . . . .	38
3.3	Flow characteristics in B . . . . .	40
4.1	Numerical vs. experimental comparison for thrust and torque prediction. $\Omega$ is the rotational speed, $T_e$ is the thrust obtained experimentally and $T_n$ is the thrust obtained numerically. The same nomenclature is applied for the torque Q. . . . .	45
4.2	Test cases in hover. . . . .	57

# Chapter 1

## Introduction

Technology is playing a significant role in the process of globalization, and one particular technology that stands out is drone technology. This technology is experiencing a continuous increase in utilization across a wide spectrum of fields, including agriculture, healthcare, and the military. Drones offer the capability to gather real-time data in agriculture, empowering farmers to make well-informed decisions about the utilization of resources on their farms [17]. Moreover, drones have the potential to revolutionize healthcare by facilitating the aerial delivery of essential medical supplies such as blood, vaccines, medications, and laboratory samples to remote and isolated regions, particularly in developing nations during health emergencies. In the military context, drones play a crucial role in enhancing security and surveillance by monitoring and tracking the movements of adversaries, aiding in the identification of targets for potential strikes.

While the advantages of drone technology are clear, it's important to acknowledge that improper usage can lead to harm to individuals and property. Inadequate training of drone operators and technical malfunctions during flight can result in injuries and damages. Additionally, there is a concern that drones could be commandeered by extremists to divert payloads for their own gain, posing potential security risks.

In this chapter some applications and a general classification of Unmanned Aerial Vehicles (UAVs) is presented in section 1.1, together with the role of fluid dynamics in designing such vehicles and challenges that need to be overcome. Section 1.2 focuses on rotary-wing drones, providing a theoretical background in understanding fluid dynamics features of propellers implemented in Micro Air Vehicles and numerical methods employed to represent those features, that is the object of this thesis.

## 1.1 The role of drones in modern society

Since their first developments, drones have revolutionized flight, opening a huge spectrum of new opportunities that were unthinkable decades ago. Drones applications, which go from military uses to observation, exploration, meteorology and logistics, are nowadays growing fast thanks to new technological developments in different fields [18]. Over the past few decades, the emergence of a compact aerial device, that is Micro Air Vehicles has led to a rise in the demand for intelligence-driven operations. Consequently, significant attempts are currently underway to create highly mission-specific, miniature air drones.

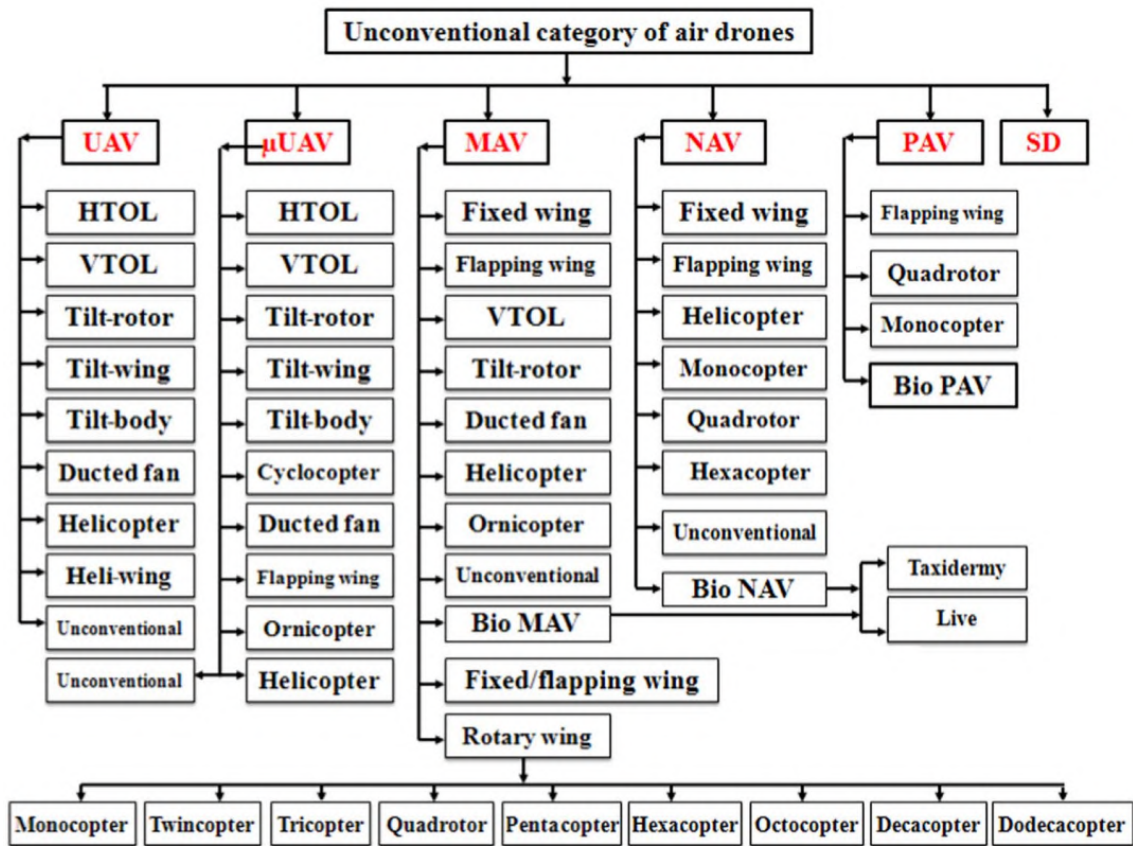


Fig. 1.1 Drones' classification [1].

These endeavors have yielded a diverse range of small drones, exhibiting various architectures and flight capabilities, as shown in figure 1.1. In general, drones can be classified based on their performance characteristics. Key design parameters such as weight, wing span, wing loading, range, maximum altitude, speed, endurance, and production costs play a major role in distinguishing various types of drones and facilitating useful classification metrics. Furthermore, drones can be sorted based also on the type of engines they employ, in particular UAVs use fuel engines, while MAVs use electrical motors.

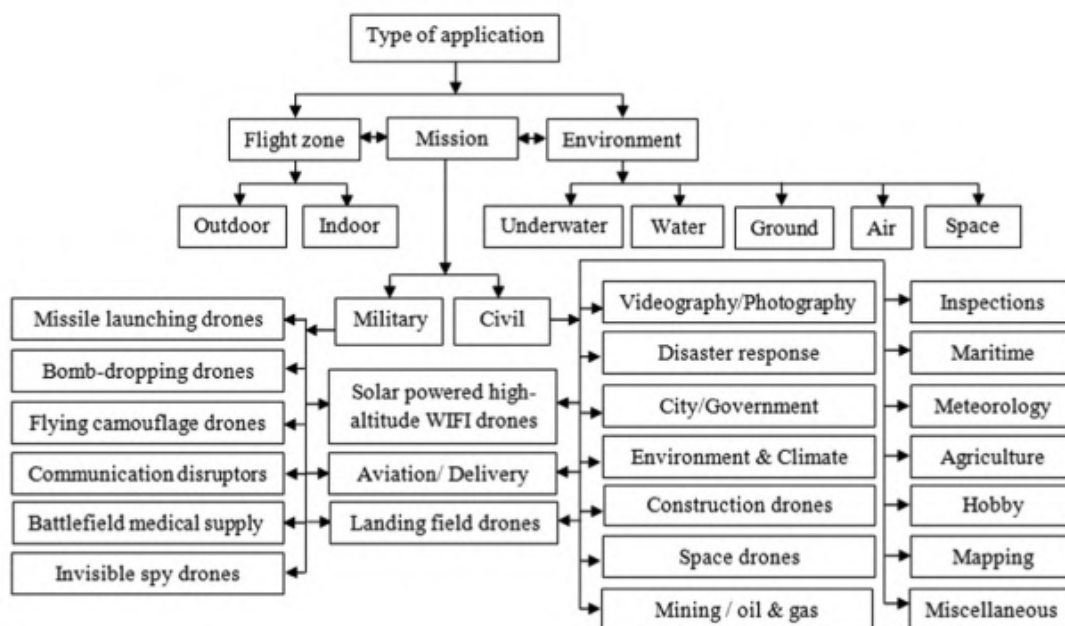


Fig. 1.2 Drones' applications [1].

As shown in figure 1.2, drones have a wide range of purposes, also in our daily life. These applications can be classified in several ways, including the type of mission, type of the flying zone and type of the environment [1]. Among the several employments of drones, mailing and delivery services seems to become important realities. In particular, last-mile deliveries consist in a rapid package delivery from local distribution hubs to a receiving vessel. This application, that could revolutionize also the urban mobility, could have a viable market by 2030, as reported in the market study conducted by McKinsey & Company [19]. Other applications consist in environmental protection, such as managing national parks and tracking wildlife, observe and monitor the climate change, but they can also be employed for recognition and investigation of natural disasters. Beside conventional applications, drones can be employed in some unconventional missions. For example, Tokyo's Metropolitan Police Department unveiled its anti-drones which are used to take down naughty or offensive drones from the sky. Furthermore, drones can be used as runways for other drones, can be applied to guide or scare birds away from airports and can also be used to clean windows and solar panels.

The majority of the applications cited above are covered by means of rotary-wing drones. Such drones can perform forward flight, vertical take-off and landing and have the capability of hovering flight, some common architectures are shown in figure 1.3. Even if rotary wings have simple control systems, their main disadvantage is the power consumption; in fact there are several challenges in designing these drones when their size and consequently weight are decreased. For instance, when they have low thrust loading and the efficiency of rotors is poor. For these reasons

it is important to conduct experimental and numerical analyses in order to predict the behaviour of these systems also in non-ideal conditions, such as cross-flow and gusts. Here is where the work of this thesis is placed, which aims to study and characterize the flow field of a small-sized rotor under various operating conditions, in order to provide a better understanding of fluid dynamics features of rotors and help engineers to design more efficient and less energy consuming drones, in attempt to expand the market and the applications of these systems.

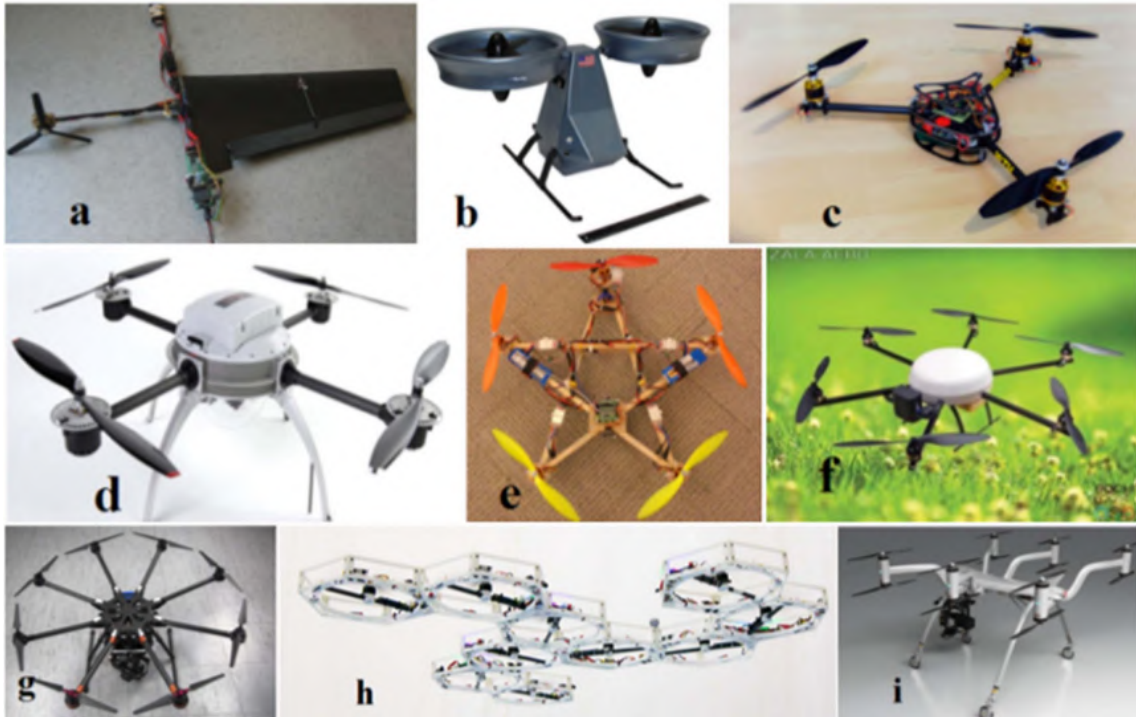


Fig. 1.3 Different types of MAVs.

## 1.2 Theoretical background

Predicting rotorcraft performance remains a challenging task. The aerodynamic flows involved are inherently characterized by unsteadiness, non-linearity and complexity. For example, a propeller blade could encounter its own tip vortex followed by the tip vortex of other blades. This complexity intensifies when aerodynamic interactions occur between multiple rotors and the fuselage, as can be seen in figures 1.4 and 1.5. Moreover, small multi-rotor vehicles experience low efficiencies both in hover and cruise [2],[20] due to the low Reynolds number regimes in which they operate. For this reason, it is important to characterize both numerically and experimentally the flowfield features of small-sized propellers.

This section aims at providing a better understanding of the wake topology of a propeller, how it affects the performance of the rotor and the differences in small-sized (MAVs) and big-sized (helicopters) rotors wake flowfield.

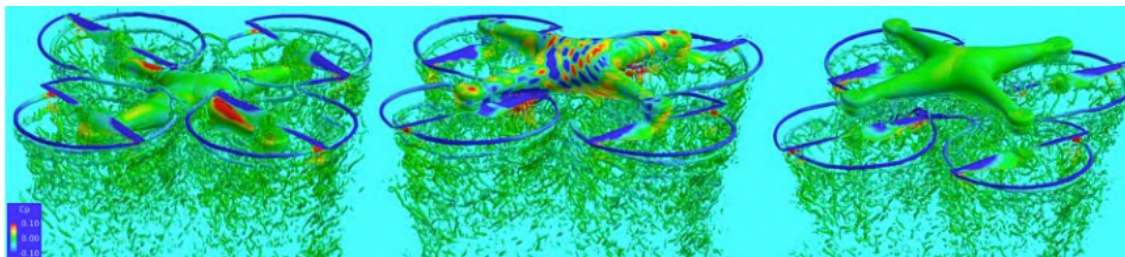


Fig. 1.4 Complexity of the wake of a drone in different configurations (iso-surfaces of Q-criterion) [2].

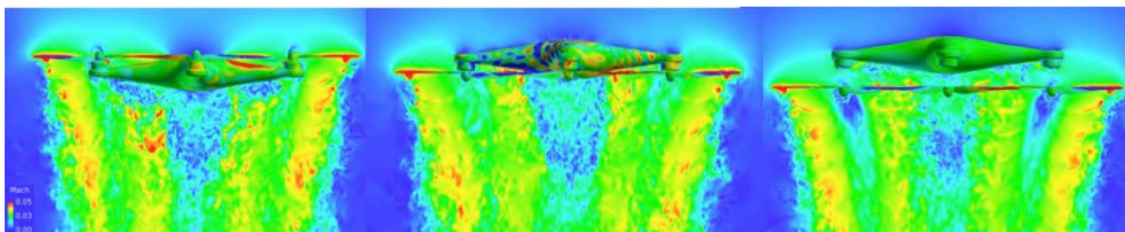


Fig. 1.5 Complexity of the wake of a drone in different configurations (velocity magnitude) [2].

### 1.2.1 Wake topology of propellers

The wake flowfield developing downstream a rotor can be decomposed in three major fields: near, mid and far wake. In particular, the near wake is the region where the flow leaves the rotor blade and completes the formation of the first trailing edge vortices, together with the first tip vortices (see figure A.1 in Appendix A). An accurate solution of this field is needed to correctly predict the airloads and the rotor vibrations. In fact, according to [3] and [21], it was found that the rotor performance is mainly sensitive to this near wake features, that is because a rotor wake follows a trajectory that periodically passes near its own generating rotor blades before being convected downstream by the induced axial flow.

The mid wake is instead representative of the region where the flow interacts with the body. Here the trailing edge vortices have begun to evolve in a coherent structure denominated "Vortex sheet", while the tip vortices still remain discernable in their own structure. The correct computation of this region's flowfield permits to accurately evaluate the interaction forces between the rotor wake and the body which sustains the rotor, which could be for example an helicopter fuselage or a drone frame. Finally, the far wake is where wake-environment interactions such as ground effect and brownout take place. This effects could non-negligibly affect the performances, so

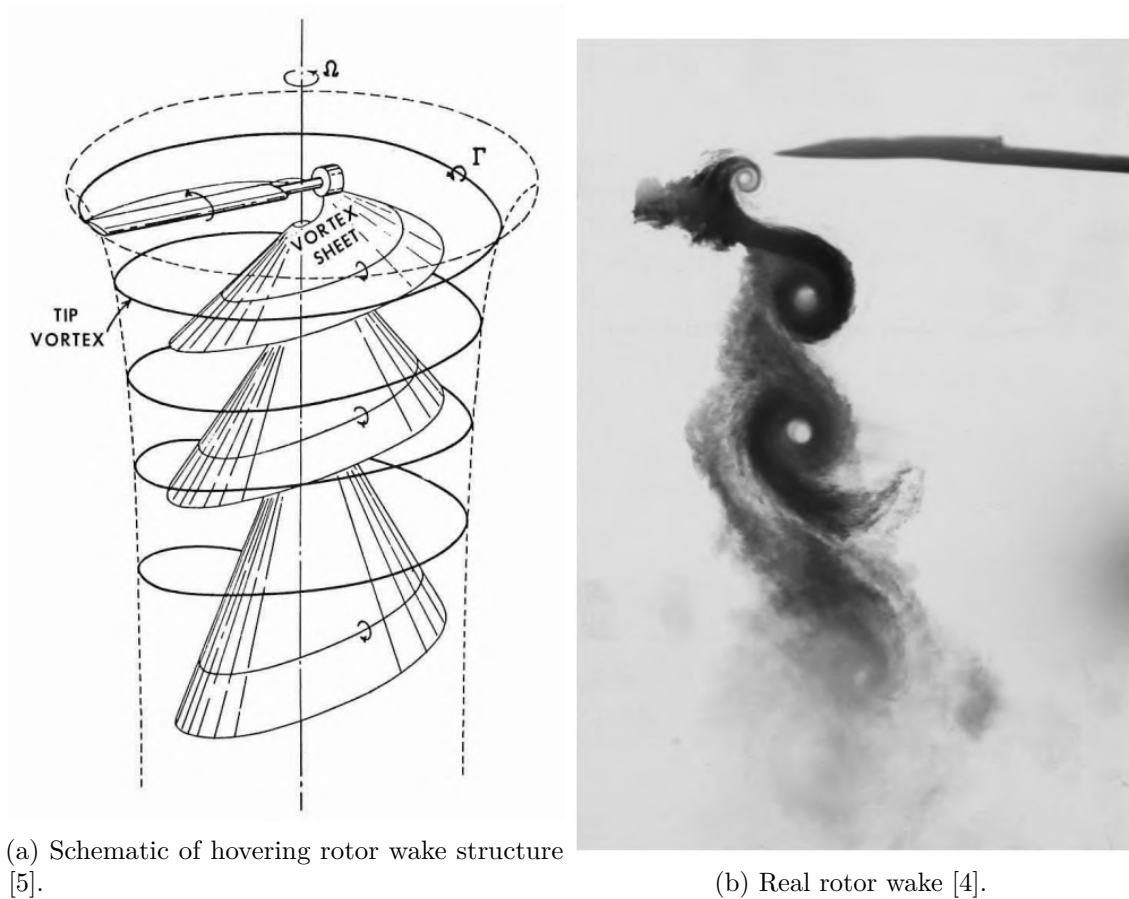


Fig. 1.6

it is important to take them into account. However, in this region the tip vortices and trailing edge ones are mixed together in a turbulent structure, so it is consequently more difficult to accurately compute the flowfield.

The primary features of a rotor wake are the tip vortex, which arises from the rolling up of the vortex sheet shed from the tip region of the blade, and the vortex sheet shed from the inboard section of the blade [5], a schematic representation of the main features of a propeller wake can be seen in figure 1.6.

Although the tip vortex and the vortex sheet shed from the trailing edge of the blade are separate entities, they influence each other. In fact, because of the velocity induced by the tip vortex, the axial advection velocity near the tip of the inner vortex sheet is greater than that of the tip vortex. The axial velocity of the inner vortex sheet increases also with the radial position, resulting in a linear cross section. An important aspect, that distinguish rotary-wings from fixed-wings, is the counterrotating vortex (figure 1.7) formed at the edge of the inboard vortex sheet, whose strength approaches 50% of that of the tip vortex [3]. The presence of the counterrotating vortex is well demonstrated in the case of highly loaded and untwisted blades, and it is likely to be caused by aspects of rotation, such as radial acceleration. The presence of the counter-rotating vortex is of particular importance

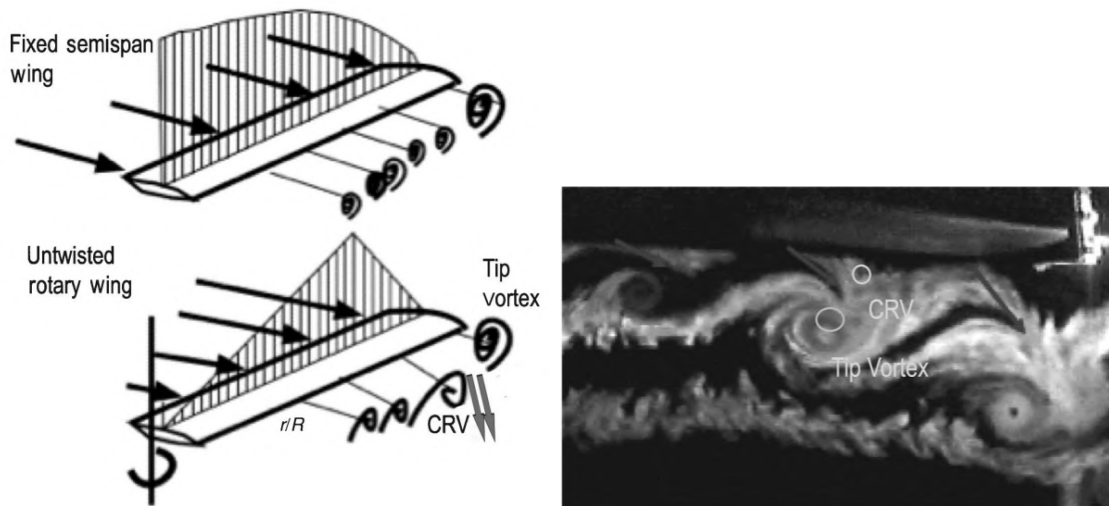


Fig. 1.7 Counterrotating vortex [3].

because of the possible influence on the structure of the wake, with strong effect on the induced velocities and the thrust that the rotor develops. In fact, where the inboard vortex sheet rolls into the counter-rotating vortex, a strong downward flow is induced and this effect causes difficulties in compute the strength of the tip vortex: if the induced velocity is used as a parameter for computing tip vortex strength, then the calculations will result in a high estimation of this quantity.

Now that the main actors of a rotor wake are clear, let's see how these features evolve downstream in the wake. Once the tip vortex leaves the blade, it initially moves inward, toward the rotation axis of the rotor, and stays close under the blades; as a consequence, the next blade's tip to come round experiences an upwash, increasing the incidence and finally intensifying the tip vortex strength [4].

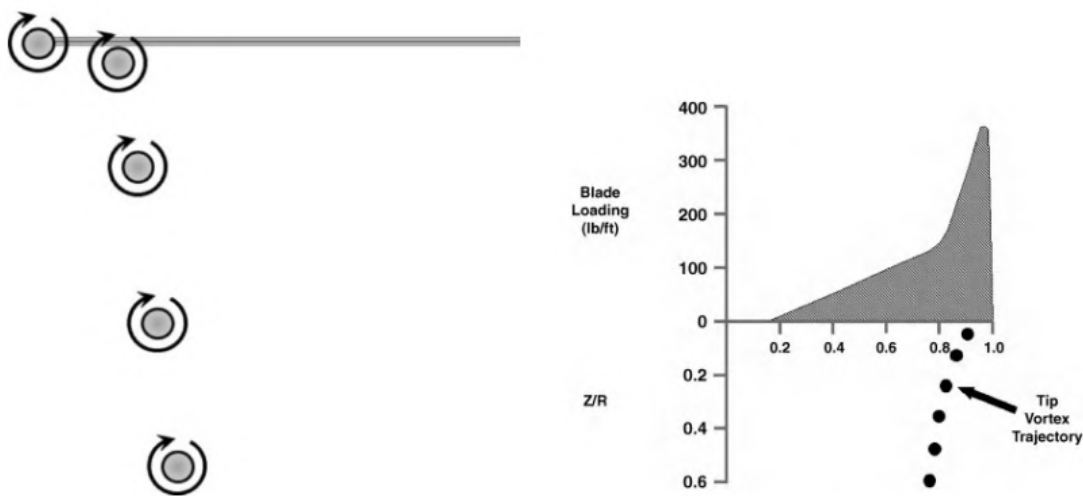


Fig. 1.8 Tip vortex motion [4].

The axial transport velocity remains relatively constant in the near wake before and after the passage of the subsequent blade, but with different values; in fact, in figure 1.9 it is possible to notice a linear variation of the axial displacement of the tip vortex with respect to the wake azimuth. This axial velocity increases linearly with increasing blade loading and decreases moderately with increasing blade twist; furthermore, the axial velocity is insensitive to variations in the number of blades [5]. Regarding the radial displacement of the tip vortex, many authors such as [5] and [6] confirm an exponential decay as the wake azimuth (wake age) is increased, this contraction appears to be a function of the rotor disk loading: more the loading, more the contraction. Regarding the inboard vortex sheet, the axial velocity of the sheet become greater with increasing the disk loading and increasing the blade twist.

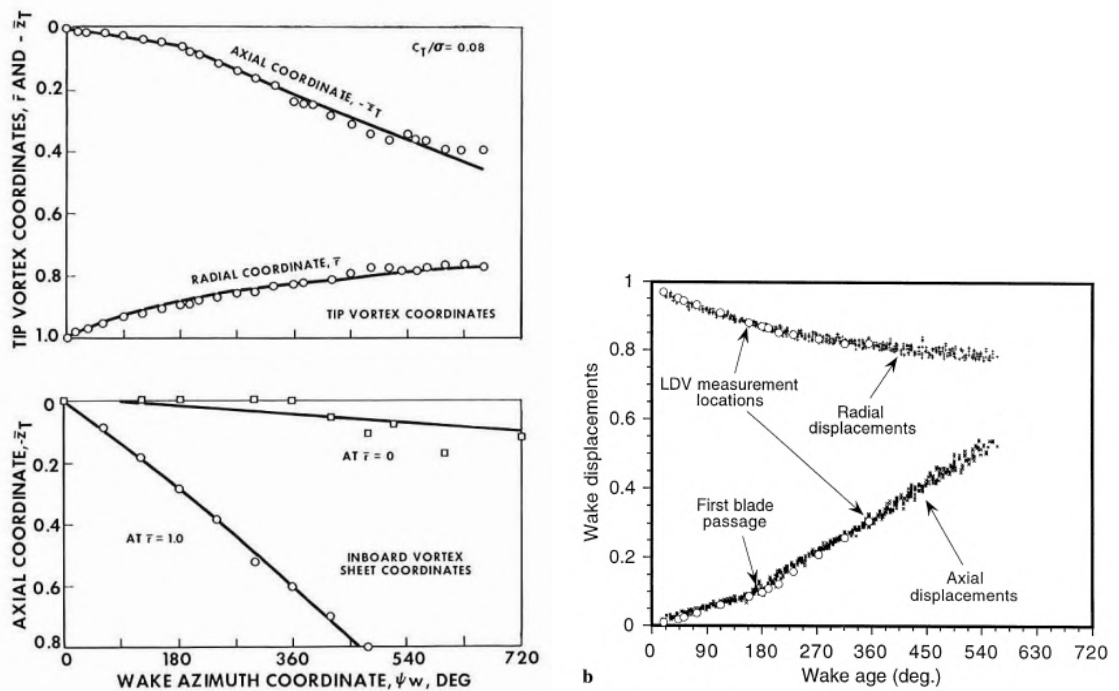


Fig. 1.9 Radial and axial displacement [5] (left), [6] (right).

According to the experiments conducted in [21], the initial size of the tip vortex core is approximately 10% of the blade chord and increasing the wake age it becomes bigger, following a square root function of wake age, with the tip vortex that tends to have an elliptical shape; whereas the inner vortex sheet remains visible until a wake age of 30 degree. As the tip vortex travels downstream an increase in aperiodic motion occurs. This aperiodic and isotropic motion [6] it is a precursor of the instability of the far wake. In particular, the transition to the far wake has been shown to occur through a deterministic vortex pairing rather than a chaotic way. When the tip vortices interact, they roll around each other. The rollup process continues until the cores come close together and then loss definition in the merger. The

merged vortices could then weaken much quicker than their components did before merger, and this delineates the start of the far wake.

The discrete structures present in the far wake might undergo fragmentation, in a similar manner to shear layer growth. Even as these mechanisms become more intricate with a higher count of blades, they adhere to deterministic explanations until vortex merging take place. In figure 1.10 it is shown the process of vortex pairing for a 2 blade rotor.

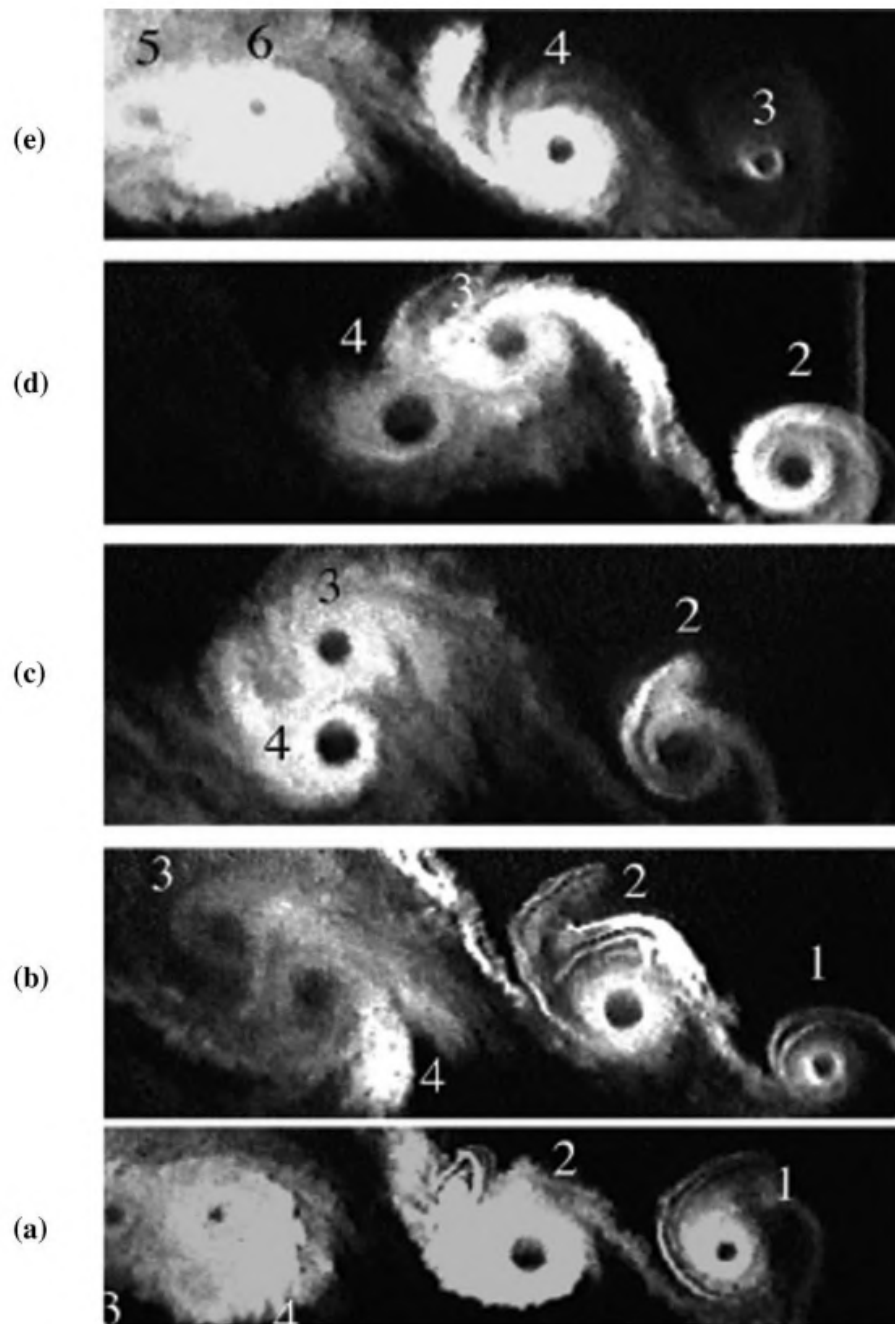


Fig. 1.10 Vortex pairing sequence [3].

Finally, wake geometry is insensitive to independent variations of tip speed and aspect ratio, and the influence of number of blades is limited to the wake azimuth angle at which the axial velocities increase significantly. On the other side, the performance of a rotor is sensitive to the tip vortex geometry. This is particularly true in hover flight for rotors with high number of blades.

## 1.2.2 Rotors at low Reynolds number

The aerodynamics of rotary-wing vehicles in regimes' typical of MAVs' are very different from those in higher Reynolds number regimes, such as helicopters (see figure 1.11). In fact, if compared to helicopters, MAVs experience a poor hover efficiency [22].

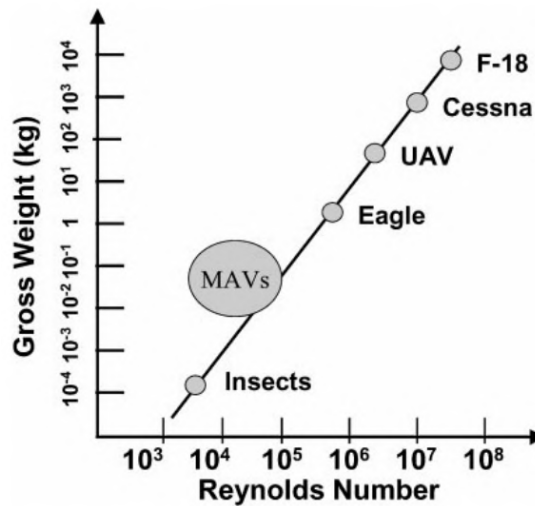


Fig. 1.11 Relative magnitude of various aircraft [7].

Since the Reynolds number represents the ratio between inertial and viscous forces, MAVs operate in regimes where viscous forces are dominant. Consequently, the boundary layer physics such as flow separation and re-attachment zones on the airfoil vary. In [7] it is proved that profile drag for low Reynolds regime is significantly stronger (45%) than full-scale helicopters (30%). These effects can be attributed to an increase in viscous drag of the airfoil and flow separation susceptibility of the boundary layer, fact it is known that the sensitivity of airfoil performance at different Reynolds number is related to the boundary-layer characteristics.

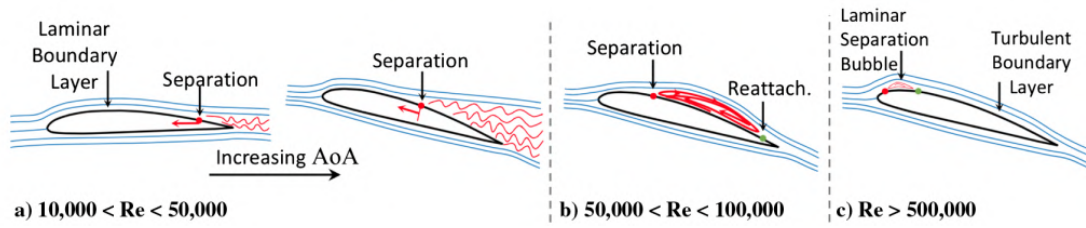


Fig. 1.12 Airfoil separation characteristics at different Re [8].

Referring to figure 1.12, it is possible to notice that at conventional Reynolds numbers (c), the laminar flow that travels over the upper surface of the airfoil experiences a large adverse pressure gradient close to the leading edge; because of the low kinetic energy of a laminar boundary layer, the flow separates as a shear layer. The shear layer then gains momentum from the free stream and reattaches as a turbulent boundary layer, originating a laminar separation bubble (LSB). Even though the turbulent boundary layer is more energetic than the laminar one, at high angles of attack it separates closer to the trailing edge, resulting in increased pressure drag and decreased lift.

At lower Reynolds numbers (b), as a consequence of the higher contribution of viscous effects, both the separation bubble and the turbulent boundary layer grow in size, resulting in increased parasitic drag. The separated shear layer still gains enough energy from the free stream to be able to reattach as a turbulent boundary layer. Nevertheless the reattachment point is very far from the leading edge. As the angle of attack increases, the reattachment point moves in the direction of the trailing edge, creating a very large separation bubble. When the airfoil is close to stall, the flow fluctuates between separation and reattachment, causing an unsteady aerodynamic phenomenon: lift and drag are difficult to quantify.

In the case of low Reynolds numbers (a), as the angle of attack increases, the separation point moves in the direction of the leading edge, resulting in a shear layer. The shear layer in this case is unable to reattach as a turbulent boundary layer, resulting in high drag and poor lift. The separation region then increases in size as the Reynolds number is decreased for a given angle of attack.

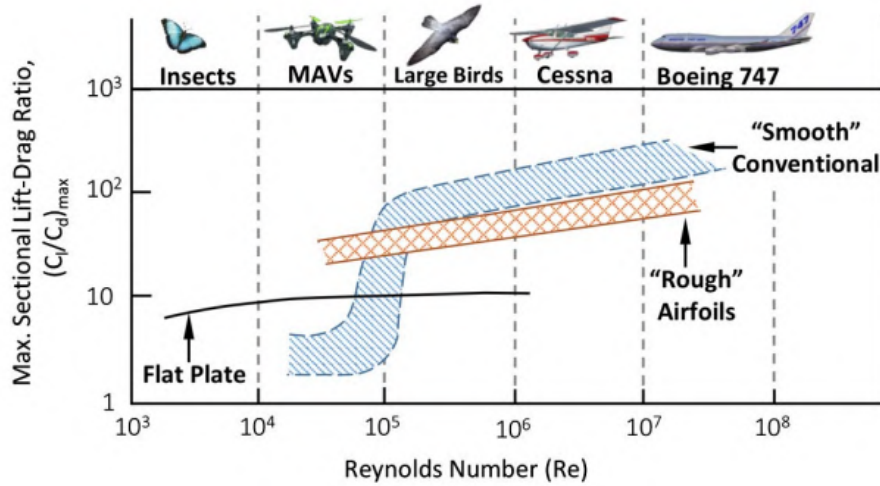


Fig. 1.13 Effect of Re on airfoil lift to drag ratio [8].

It is evident also from figure 1.13 that downsizing an airfoil drastically reduces its aerodynamic efficiency in terms of lift to drag ratio, so an airfoil suitable for high-Re applications is not suited for low-Re regimes, reducing the overall efficiency of the drone and so, reducing the power consumption. These effects are easy to see in a polar curve, like figure 1.14, where it is possible to notice a relatively flat behaviour of the efficiency. The low lift to drag ratio could be a consequence of the laminar separation bubble in a wide portion of the blade. In particular, at this low-Re regimes, the profile drag has a larger influence over the total power required by the rotor. This is why also a reduction in induced power does not influence so much the rotor performance.

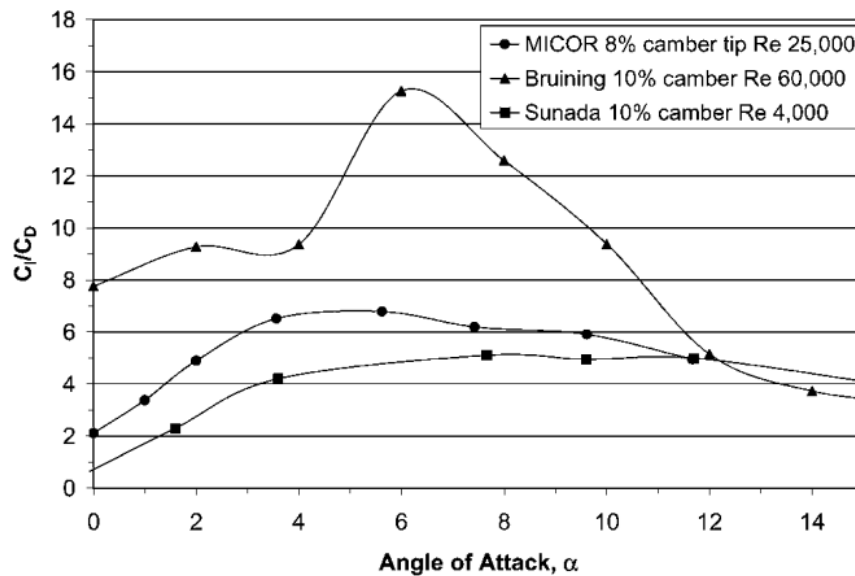


Fig. 1.14 Airfoil lift to drag ratio [9].

An estimate of the efficiency of a rotor in hover is the figure of merit (FM), that is the ratio between the ideal power and the actual required power of the rotor. This parameter should be used as a comparative measure between two rotors at the same blade loading [10].

$$FM = \frac{C_T^{3/2}}{C_P \sqrt{2}} \quad (1.1)$$

Where  $C_T$  is the thrust coefficient and  $C_P$  the power coefficient, defined as:

$$C_T = \frac{T}{\rho A \Omega^2 R^2} \quad (1.2)$$

$$C_P = \frac{P}{\rho A \Omega^3 R^3} = \frac{\tau \Omega}{\rho A \Omega^3 R^3} \quad (1.3)$$

Where  $\tau$  is the torque and  $\Omega$  the rotational speed. Experimentally, if we can measure  $T$  and  $\tau$  then it is possible to compute the figure of merit.

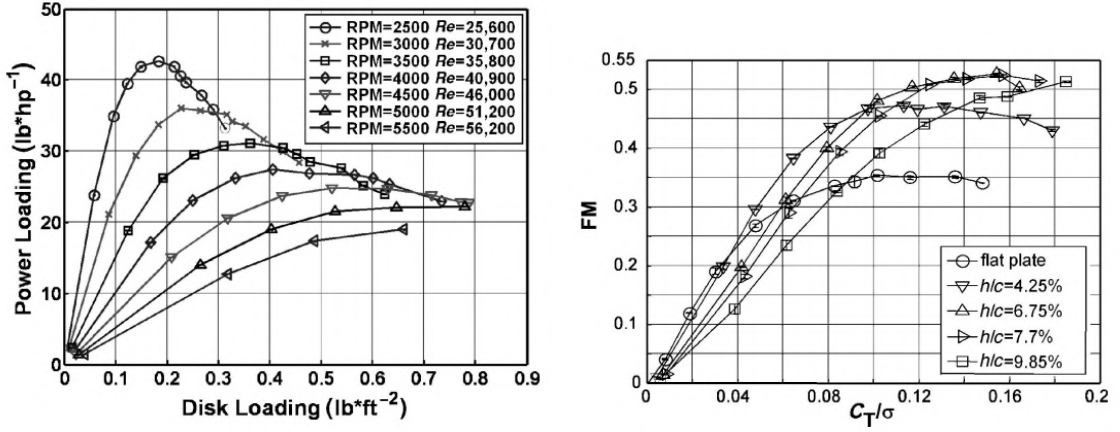
Another key factor is the power loading, defined as the ratio between thrust and power required to hover.

$$PL = \frac{T}{P} = \frac{C_T}{C_P} \frac{1}{\Omega R} = FM \sqrt{\frac{2\rho}{DL}} \quad (1.4)$$

Where DL is the disk loading. The propeller efficiency could be also defined introducing the advance ratio  $J$ , defined as  $J = V/(\Omega D)$ .

$$\eta = J \frac{C_T}{C_P} \quad (1.5)$$

Disk loading, figure of merit and power loading could be used as comparative metrics for testing different type of aifoils and to study the effect of the Reynolds number for different propeller geometries. Some examples could be found in [9], [22] and [10] (figure 1.15).



(a) Power loading as a function of disk loading. (b) Cambered airfoil performance at  $Re=40900$ .

Fig. 1.15 [10]

### 1.2.3 Numerical methods

Small-scale propellers behaviour is difficult to predict via simulations. A great amount of this difficulty arises from the dependence of the performance on the Reynolds number [23], previously discussed. In literature different approaches for determining the aerodynamic performance of a propeller are proposed. In general, the problem of determining the performance parameters of a propeller could be addressed in three ways: analytical approach, experimental approach and numerical approach. All of these three approaches have advantages and disadvantages. In particular, an analytical approach is limited only to high Reynolds applications, such as helicopters, whereas an experimental approach could be expensive and time consuming. Although no one method is better than another, a numerical approach seems to be the most immediate way of studying this problem, this is strongly supported by the technological improvements made in computer sciences, with the effect of computational cost reduction.

Nowadays the numerical methods adopted range from low-fidelity (actuator disk, blade element theory, blade element momentum theory) to high-fidelity (3D CFD). Momentum theory and blade element theory are approximations to estimate  $C_T$  and  $C_P$ , but are based on important fluid simplifications; on the other hand, many numerical studies that involved small-scale propellers proved that RANS (Reynolds-Averaged Navier-Stokes) can provide good agreement with experimental data in predicting thrust and torque [24]. RANS equations use the Reynolds decomposition, which states that the variable of interest could be seen as a sum of an average part and a fluctuating term.

$$\nabla \cdot \bar{\mathbf{U}} = 0 \quad (1.6)$$

$$\nabla \cdot \bar{\mathbf{u}'} = 0 \quad (1.7)$$

$$\rho \frac{D\bar{U}}{Dt} + \rho \nabla \cdot (\overline{\mathbf{u}'\mathbf{u}'}) = \rho \mathbf{g} - \nabla \bar{p} + \mu \nabla^2 \bar{U} \quad (1.8)$$

Equations 1.6 and 1.7 are the RANS continuity equations for the average part and fluctuating part of the flow respectively, equation 1.8 is the RANS momentum equation for an incompressible flow. The process of averaging give rise to a term  $(\nabla \cdot \overline{\mathbf{u}'\mathbf{u}'})$  that represents the divergence of the Reynolds stresses, caused by the fluctuating part of the flow. These stresses act like added shear stresses and should be modeled adding a turbulent viscosity to the fluid conventional viscosity. This method of modelling and taking into account the effect of the turbulence on the mean flow is based on the Boussinesq approximation.

The most common turbulence models are the  $k - \epsilon$ ,  $k - \omega$  and  $k - \omega$  SST. The  $k - \epsilon$  model introduces two more equations in order to close the system of equations. The first equation is the transport equation for the turbulence kinetic energy and the other one for the turbulence dissipation rate.

$$\frac{\partial(\rho k)}{\partial t} + \nabla \cdot (\rho U k) = \nabla \cdot \left[ \left( \mu + \frac{\mu_t}{\sigma_k} \right) \nabla k \right] + P_k + P_b - \rho \epsilon + S_k \quad (1.9)$$

$$\frac{\partial(\rho \epsilon)}{\partial t} + \nabla \cdot (\rho U \epsilon) = \nabla \cdot \left[ \left( \mu + \frac{\mu_t}{\sigma_k} \right) \nabla \epsilon \right] + C_1 \frac{\epsilon}{k} (P_k + C_3 P_b) - C_2 \rho \frac{\epsilon^2}{k} + S_\epsilon \quad (1.10)$$

Solving for  $\epsilon$  and  $k$  gives  $\mu_t$ , that is the turbulence viscosity.

$$\mu_t = C_\mu \frac{\rho k^2}{\epsilon} \quad (1.11)$$

The  $k - \epsilon$  model uses empirical damping functions in the viscous sub-layer (thanks to coefficients  $C_1, C_2$  and  $C_\mu$ ). These functions provide inaccurate results if the flow is characterized by strong adverse pressure gradients. In particular the  $k - \epsilon$  model under these conditions is not able to predict correctly the separation point and so the friction coefficient. For this reason the  $k - \omega$  turbulence model was introduced. In this case  $\epsilon$  is replaced by the specific dissipation rate  $\omega$ .

$$\omega = \frac{\epsilon}{C_\mu k} \quad (1.12)$$

$$\frac{\partial(\rho \omega)}{\partial t} + \nabla \cdot (\rho U \omega) = \nabla \cdot \left[ \left( \mu + \frac{\mu_t}{\sigma_k} \right) \nabla \omega \right] + \frac{\gamma}{\gamma_t} P_k - \beta \rho \omega^2 \quad (1.13)$$

The  $k - \omega$  turbulence model is more accurate than  $k - \epsilon$ , but has the disadvantage of a strong dependence of the turbulence intensity of the free stream: small changes in the turbulence intensity could lead to big changes in  $\mu_t$ . In order to overcome this

deficit, the  $k - \omega$  SST turbulence model was introduced. This model is a blending of  $k - \omega$  and  $k - \epsilon$  models. Here the equations are:

$$\frac{\partial(\rho k)}{\partial t} + \nabla \cdot (\rho U k) = \nabla \cdot \left[ \left( \mu + \frac{\mu_t}{\sigma_k} \right) \nabla k \right] + P_k + P_b - \rho \epsilon + S_k \quad (1.14)$$

$$\frac{\partial(\rho \omega)}{\partial t} + \nabla \cdot (\rho U \omega) = \nabla \cdot \left[ \left( \mu + \frac{\mu_t}{\sigma_k} \right) \nabla \omega \right] + \frac{\gamma}{\gamma_t} P_k - \beta \rho \omega^2 + 2(1 - F_1) \frac{\rho \sigma_{\omega_2}}{\omega} \nabla k : \nabla \omega \quad (1.15)$$

$F_1$  in the blending function, if  $F_1 = 0$  the  $k - \epsilon$  model is used, if  $F_1 = 1$  then the  $k - \omega$  model is used.

The models introduced above are "fully turbulent" models. Another important class of turbulent models are those that take into account also laminar flows or not fully turbulent flows, for example boundary layers in which a wide portion of the flow is laminar. Here, the Transitional  $k - \omega$  SST model uses the same equation of the  $k - \omega$  SST with a difference in the production and dissipation terms of the equations.

$$\frac{\partial(\rho k)}{\partial t} + \nabla \cdot (\rho U k) = \nabla \cdot \left[ \left( \mu + \frac{\mu_t}{\sigma_k} \right) \nabla k \right] + P_k - D_k \quad (1.16)$$

$$\frac{\partial(\rho \omega)}{\partial t} + \nabla \cdot (\rho U \omega) = \nabla \cdot \left[ \left( \mu + \frac{\mu_t}{\sigma_k} \right) \nabla \omega \right] + \frac{\gamma}{\gamma_t} P_k - \beta \rho \omega^2 + 2(1 - F_1) \frac{\rho \sigma_{\omega_2}}{\omega} \nabla k : \nabla \omega \quad (1.17)$$

Here  $\gamma$  is the turbulence intermittency. If  $P_k = 0$  the flow is laminar, if  $P_k = 1$  the flow is fully turbulent. This model requires one more equation that represents the transport of  $\gamma$  and one for the transport of  $\overline{Re_{\theta,t}}$ , which is the Reynolds number (referred to the momentum thickness) at which the transition occurs.

$$\frac{\partial(\rho \gamma)}{\partial t} + \nabla \cdot (\rho U \gamma) = \nabla \cdot \left[ \left( \mu + \frac{\mu_t}{\sigma_\gamma} \right) \nabla \gamma \right] + P_\gamma - D_\gamma \quad (1.18)$$

$$\frac{\partial(\rho \overline{Re_{\theta,t}})}{\partial t} + \nabla \cdot (\rho U \overline{Re_{\theta,t}}) = \nabla \cdot \left[ \left( \mu + \frac{\mu_t}{\sigma_{\theta,t}} \right) \nabla \overline{Re_{\theta,t}} \right] + P_{\theta,t} \quad (1.19)$$

Any cell in the domain will have a specific value of  $\overline{Re_{\theta,t}}$ , then it is computed the Reynolds number at which the intermittency begin to become greater: if this value crosses a threshold then the turbulence production term will be activated.

One of the major disadvantages of the turbulence models based on the Boussinesq approximation (Turbulent Viscosity Hypothesis) is that they don't take into account

and they can't capture the effects of the curvature of the flow. This limit has been overcome modifying the turbulent kinetic energy production term. In this case a function named  $f_{r1}$  multiply the turbulent kinetic energy production term  $P_k$ . If the function is 0 (convex curvature) the production term is negligible, if the function is set to 1.25 (concave curvature) the production term become important.

$$f_{rot} = (1 + C_{r1}) \frac{2r^*}{1 + r^*} \left[ 1 - C_{r3} \tan^{-1} C_{r2} \tilde{r} \right] - C_{r1} \quad (1.20)$$

$$f_{r1} = \max[\min(f_{rot}, 1.25), 0] \quad (1.21)$$

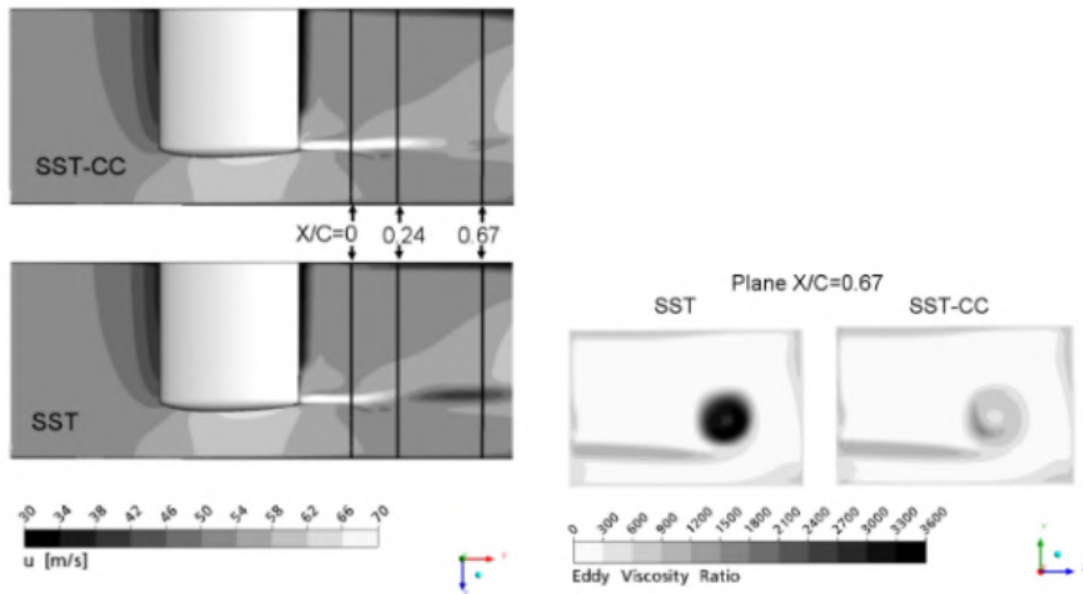


Fig. 1.16 Comparison between  $k - \omega$  SST and  $k - \omega$  SST-CC in predicting the tip vortex characteristics of a wing with a NACA 0012 airfoil [11].

The  $k - \omega$  SST-CC (curvature correction) has been tested in a wide range of simulations and test cases demonstrating to provide more accurate results with respect to the traditional  $k - \omega$  SST [12]. In particular, the old model seems to overestimate the intensity of a tip vortex and so the decay of axial velocity of the vortex, due to an overestimate in the turbulence activity in the vortex, this behaviour can be seen in figure 1.16.

The nature of the flow developed by a rotating rotor is unsteady. This implies a simulation with a dynamic mesh, which is typically very computationally expensive. An alternative is studying the problem with a moving reference frame fixed with respect to the rotor (figure 1.17), in which the flow could be modelled as a steady-state [25].

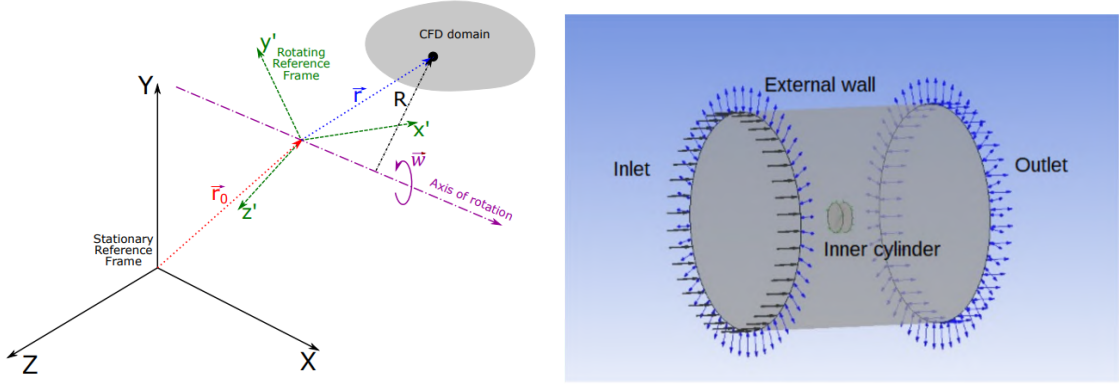


Fig. 1.17 Multiple reference frame technique [12] (left) and computational domain [13] (right).

The rotating fluid around the rotor, in which the blades and the hub are relatively stationary, is set as the moving reference frame. The connection between the stationary and rotating part of the computational domain is controlled by a mesh interface, which has no physical meaning, but is required only for the simulation [26]. For this type of simulation the momentum equation is modified in order to include the effect of rotation experienced by the cells in the moving reference frame domain. In particular, in the moving reference frame:

$$\mathbf{U} = \mathbf{U}_r + \boldsymbol{\Omega} \times \mathbf{r} \quad (1.22)$$

Where  $\mathbf{U}_r$  is the relative velocity and  $\boldsymbol{\Omega} \times \mathbf{r}$  the tangential velocity. The fundamental idea is to resolve the Navier-Stokes equations in terms of  $\mathbf{U}_r$  for every cell in the moving reference frame and then compute the absolute velocity  $\mathbf{U}$ .

$$\nabla \cdot (\mathbf{U}_r \mathbf{U}_r) = -\frac{1}{\rho} \nabla p + \nabla \cdot (\nu \nabla \mathbf{U}_r) - \boldsymbol{\Omega} \times \boldsymbol{\Omega} \times \mathbf{r} - 2\boldsymbol{\Omega} \times \mathbf{U}_r \quad (1.23)$$

The two extra terms represent the Coriolis force and centrifugal effects. Typically the moving reference frame technique is referred to as frozen rotor because the rotor position remains fixed in space. A more accurate, but more computationally consuming, is the sliding mesh technique, in which the rotor moves together with the elements inside the rotating zone to represent the actual rotational effect. The sliding mesh technique can represent also the transient effects such as vortex shedding, while the moving reference frame technique is not able to resolve and is not able to represent the actual rotational effects because relative motion between the rotating zone and adjacent zone is not taken into account and furthermore because the MRF approach can only provide the time averaged steady-state solution. Even though the MRF approach is less accurate with respect to the sliding mesh approach, it is able to well predict thrust and power consumption of propellers, with the big advantage of very fast simulations.

In conclusion, the numerical method adopted for the simulation of a rotor should be chosen thinking of the problem. BET and BEMT models are very easy and fast methods to use, but their use is limited to specific cases with a reliability that decreases with the increase in the advance ratio. Furthermore, these methods require input parameters from experimental studies, which make them difficult to use in absence of experimental data. On the other hand, CFD simulations are highly used to study the aerodynamics of rotors. In particular, the moving reference frame technique seems to represent a good compromise between computational costs and accuracy, in particular when 3D effects and turbulence are taken into account. However, CFD simulation reliability depends on the mesh size and quality, domain size, physical formulation, turbulence model adopted and solution type.

# Chapter 2

## Experimental and numerical setup

### 2.1 Introduction

The following chapter has the purpose of introducing the experimental and numerical setup adopted for the experiments, describing its main components and functions, as well as the motivations that led to certain choices. More in detail, section 2.2 will briefly discuss the operating principle of the Particle Image Velocimetry (PIV) technique and its constituent components. Following that, the rotor support on which the experimental analyses will be conducted will be presented. Finally, in section 2.3, the numerical setup will be introduced, including the choice of computational domain dimensions, the mesh, and the numerical models used for the analyses.

### 2.2 Experimental setup

The main advantages of pneumatic or anemometric measurement techniques are their ease of use. However, these techniques have the disadvantage of being intrusive and point-based, not allowing for mapping of the entire flow field. In order to overcome these limitations, optical techniques have been developed, which provide information on the entire flow field without errors due to intrusiveness. The Particle Image Velocimetry (PIV) falls into this category of techniques.

PIV is based on evaluating the displacement of tracing particles, which move with the flow, in order to indirectly determine the velocity field. A typical PIV setup consists of several subsystems, including: seeding, a laser source, a camera, optical lenses, and image processing software, as shown in figure 2.1. In practice, small particles on the order of microns are injected into the flow field. The investigation region is illuminated by a laser sheet, and a camera is positioned perpendicular to it to capture the scene. Typically, the interrogation region is illuminated twice by two

laser pulses separated by a certain time interval  $\Delta t$ , which depends on the studied phenomenon. At this point, the illuminated particles are photographed for each laser flash, and the scene is recorded on a camera frame.

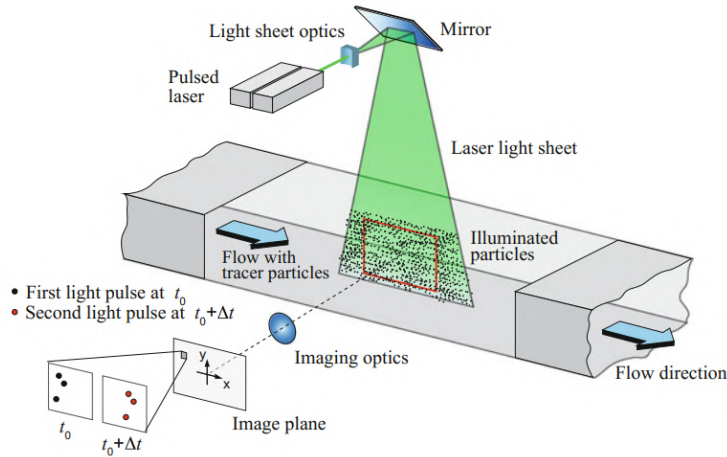


Fig. 2.1 An example of a PIV apparatus.

Consequently, two images representing the flow field at time  $t$  and  $t + \Delta t$  are obtained. These two images are then divided into appropriately sized interrogation windows. Each window in the image captured at time  $t$  is compared to the corresponding window in the image at time  $t + \Delta t$  to evaluate the cross-correlation coefficient, which represents the most probable displacement of the particles. Given the time  $\Delta t$  and the pixels per millimeter, each interrogation window will be associated with a velocity vector.

In this thesis, planar PIV was used to study the wake topology and fluid dynamics characteristics of a drone propeller under different operating conditions. Figure 2.2 shows the PIV setup. A Dantec Dynamics Nd: YAG Dual Power 200 laser, operating in dual pulse mode with a pulse energy of 200 mJ and a repetition rate of 15 Hz, was employed to illuminate the tracer particles. To create a thin laser sheet, the laser beam was manipulated using an optical setup comprising a spherical lens with a focal length of 1000 mm and a cylindrical lens with a focal length of -50 mm. To capture images of the tracing particles, a synchronized Andor Zyla 5.5Mpix sCMOS camera with a sensor size of  $2560 \times 2160$  pixels<sup>2</sup> and a pixel size of  $6.5 \mu\text{m}$  was employed. The camera operated in double exposure mode and had an acquisition frequency of 15 Hz. To capture the images, a Tokina 100 mm Macro lens with an aperture value of  $f = 11$  was attached to the camera. The investigation area covered a region of approximately  $15 \times 16.8$  cm in the x-y plane (refer to figure ), which corresponds to an optical/spatial resolution of roughly 16 pixels per millimeter. For seeding the flow upstream of the contraction (see figure 2.3a), a Laskin nozzle was employed, which

generated particles of approximately  $1\ \mu\text{m}$  in size. These particles were dispersed using the high-performance seeding fluid "PIVLIGHT."



Fig. 2.2 Experimental setup.



(a) Seeding system.

(b) Andor Zyla 5.5Mpix sCMOS camera.

Fig. 2.3

The experiments were conducted in an open-loop wind tunnel, which will be extensively described in chapter 3. Below, the rotor setup will be described more in detail.

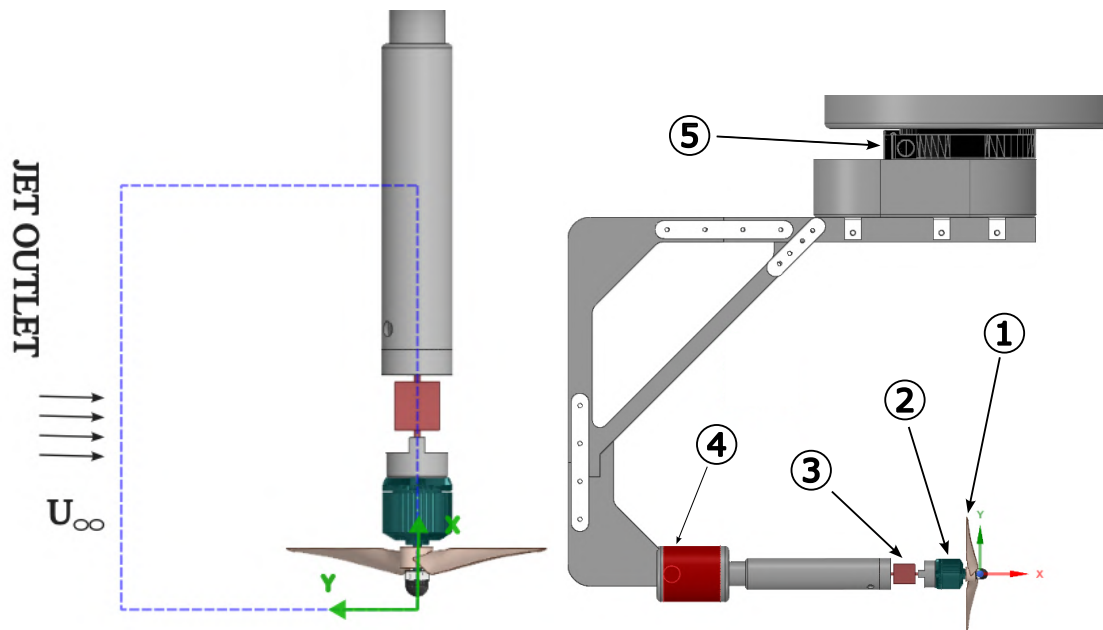


Fig. 2.4 X-Y is the interrogation plane. On the right the rotor setup. x-y is the body reference frame, fixed with the propeller. (1) propeller, (2) motor, (3) load cell, (4) torque cell, (5) servo.

The main components, as illustrated in Figure 2.4, are briefly described. The propeller used in the experiments has a radius  $R$  of 7.5 cm and a NACA 4412 airfoil, the propeller was fabricated using 3D printing technology with VisiJet Armor M2G-CL resin. The rotor setup consists of several components and subsystems. A TRX370 1000KV brushless motor with a diameter of 2.8 cm and a maximum power of 150 W is used as the main driving force. The motor is controlled by an external electronic speed control (ESC) controller, which receives input commands through an Arduino Uno board. To measure the rotational speed of the motor shaft, a Hobbywing RPM sensor is employed. This sensor is connected to two of the three phases of the brushless motor and detects voltage changes within a 0.1-second time interval. The information is then converted into RPM values. The RPM sensor has a rated output ranging from 1000 to 300,000 RPM for 2-pole motors.

The rotor, including the motor and the propeller, is mounted on a 3D printed support made of polylactic acid (PLA). The support is designed to minimize vibrations caused by the rotating propeller. Additionally, the support incorporates two load sensors. The first is a bi-directional axial load cell LSB200 Futek, excited with 5 VDC, used for measuring thrust. It has a rated output of 2.5 N with a non-linearity and hysteresis of  $\pm 0.1\%$  of the rated output. The operating temperature range

of the load cell is 223-365 K. The second sensor is a torque sensor TFF400 Futek, excited with 10 VDC, used for measuring torque. It has a rated output of 0.07 Nm with a non-linearity and hysteresis of  $\pm 0.2\%$  of the rated output. The torque sensor operates within the temperature range of 223-365 K.

Finally, the PLA support is connected to an Optosigma OSMS-120YAW servo motor, which allows for a  $360^\circ$  rotation around a vertical axis passing through the propeller's hub. This feature enables the propeller to be positioned and fixed within the test section when rotated.

## 2.3 Numerical setup

According to [12], there are several approaches to studying rotor aerodynamics: analytical, numerical, and experimental. The analytical approach is not suitable for analyzing small-sized rotors, as these theoretical approaches are based on the simplification of high Reynolds numbers. In this thesis, both numerical and experimental approaches are used, highlighting how the two approaches complement each other.

Among all the numerical methods adopted in rotor aerodynamics studies, CFD simulations remain the most widely used, as discussed in chapter 2. Numerical studies conducted on small rotors have revealed that a Reynolds-averaged Navier-Stokes (RANS) approach can provide adequate and satisfactory results in terms of thrust and torque; for this reason the Multi Reference Frame approach (Frozen rotor) is implemented in this thesis. In particular, in this section will be discussed the chosen domain, the dimensions, the boundary conditions, the mesh and the turbulence model adopted for the analysis, with particular emphasis to the reasons that led to concrete choices.

One choice concerns the shape and the dimension of the computational domain. Many authors adopt different shapes: rectangular [27], cylindrical [12][24][25][13] and bullet type. No shape appear to be better than another, the choice is driven primary by the problem. As already discussed, the computational domain is composed of different sub-domains: external domain and rotating domain. In particular, the external domain is stationary, while in the rotating reference frame the rotation is simulated by writing the RANS equations in an appropriate reference frame. The stationary domain and the rotating domain are linked by an appropriate interface, while the propeller is fixed in space and time. Clearly, the smaller the domain, the better in terms of computational costs, but it is not necessarily the same for the accuracy of the solution obtained. For this reason, in this section will be investigated the influence of the computational domain size, both stationary and rotating, on the

solution. After the optimum size is reached, different meshes will be compared with the final purpose of a compromise between computational costs and accuracy.

A typical domain is represented in figure 2.5a. It is composed of two cylindrical regions with different dimensions: the rotating region and the stationary region. In this phase of the analysis the dimensions A,B and C are varied in order to investigate the influence of the dimensions of the stationary domain on the solution. The mesh and the mesh refinement regions in figure 2.5b, which will be discussed later, remain unchanged during this analysis.

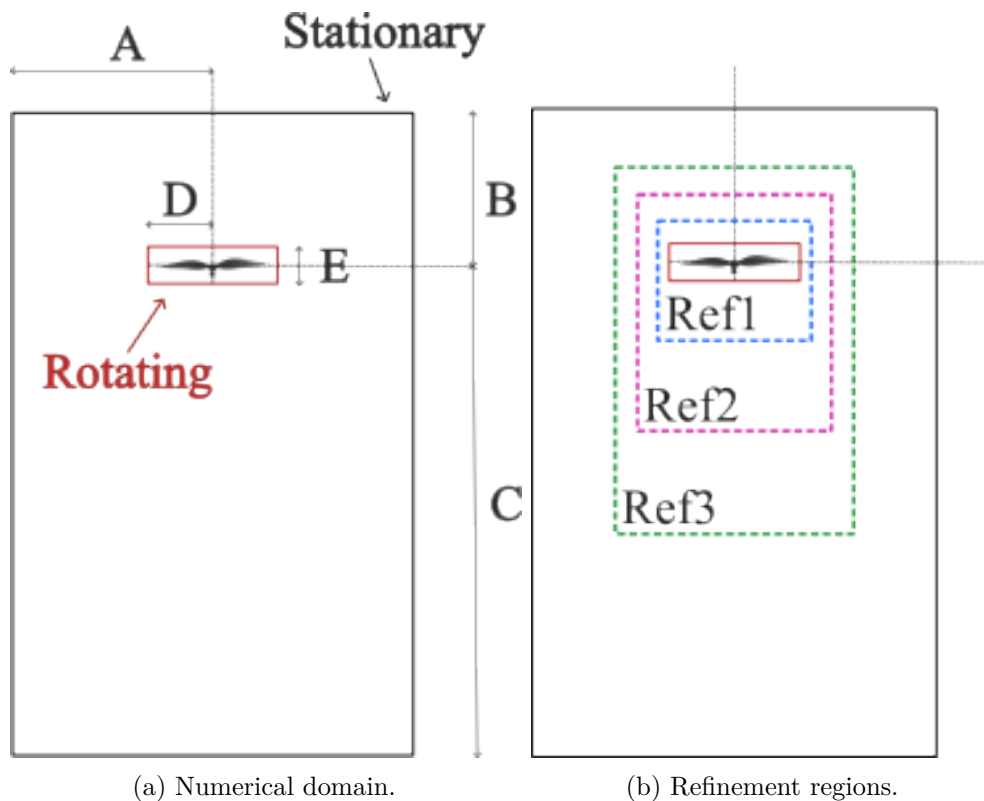


Fig. 2.5 Numerical domain and refinement regions.

Once the proper dimensions of the stationary domain are chosen, we will investigate the influence of the rotating domain and the influence of the mesh size on the solution, in order to reach an optimum in terms of computational costs and accuracy. Table 2.1 summarize the domain size investigated, where  $D$  is the diameter of the propeller. The thrust  $T$  is used as a reference parameter, while  $\epsilon$  is the error with respect to the reference (*Dom1*).

Table 2.1 Stationary domain analysis (D=0.1524 m).

	A	B	C	T [N]	$\epsilon$ [%]
Dom1	5D	7D	13D	0.4269	0
Dom2	4D	5D	10D	0.4270	0
Dom3	3D	4D	7D	0.4270	0

The analysis is conducted at a fixed rotational speed equal to 5000 rpm, in hovering. The dimensions D and E of the rotating domain are both fixed and equal to 0.56D and 0.23D respectively. As can be seen, the thrust experience a very little variation with respect to the reference value. These results allow the selection of a smaller domain, for example *Dom2* or *Dom3*, for the analysis, thus reducing the number of cells and so the computational cost.

Another question to address regards the rotational domain thickness. This is a crucial problem in multiple reference frames simulations, in particular for small propellers and rotors with 2 blades [25]. In particular, a rapid transition from a rotating frame to a stationary one could result in an unphysical numerical diffusion of the conservative quantities, causing a change in the flow characteristics around the propeller. For this reason, the dimension E of the rotating domain will be varied maintaining constant the other parameters. Table 2.2 summarize the results obtained.

Table 2.2 Rotating domain analysis (D=0.1524 m).

	D	E	T [N]	$\epsilon$ [%]
Rot1	0.56D	0.23D	0.4269	0
Rot2	0.56D	0.11D	0.3630	15
Rot3	0.56D	0.36D	0.4269	0

From table 2.2 it can be seen that the rotating domain size affects the solution. In particular, small domains seems to underestimate the thrust of the propeller.

Once the proper size of the stationary and rotating domain are selected, we focus on the mesh optimization. For this study a cartesian mesh has been chosen. The base size of each cell is a fraction of the airfoil chord at 75% of the propeller radius  $c$ , see equation 2.1. This base size is then multiplied by a magnification factor for the regions where the cell size could be bigger. Ref1, Ref2 and Ref3 are three cylindrical refinement regions, in order to better capture the wake of the propeller. The size of these regions and the influence on the results will be discussed later. Table 2.3 summarize the base size for each region.

$$B_s = \frac{c}{100} \quad (2.1)$$

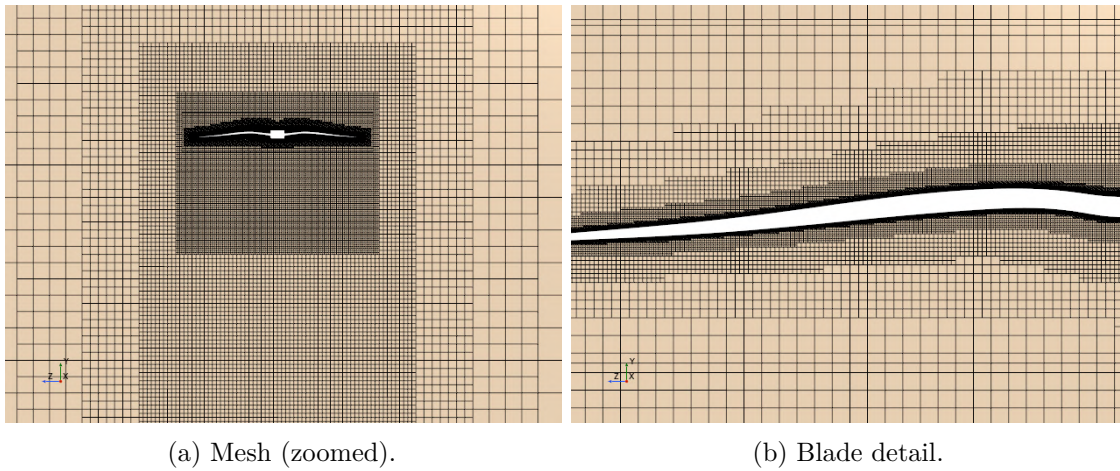


Fig. 2.6 Cartesian mesh.

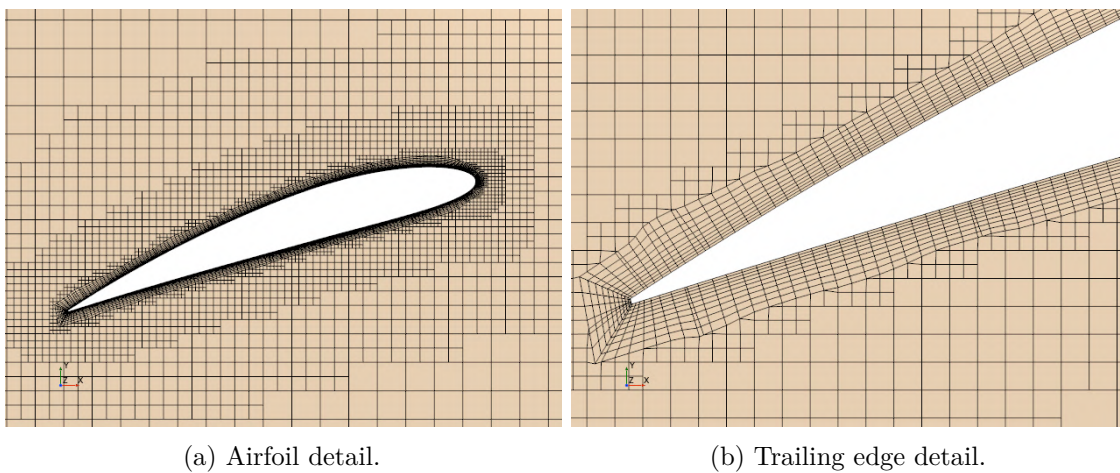


Fig. 2.7 Cartesian mesh.

Table 2.3 Mesh base size ( $c=0.011304$  m).

	Base size
Stationary	$256B_s$
Rotating	$B_s$
Ref1	$16B_s$
Ref2	$32B_s$
Ref3	$64B_s$

Regarding the boundary layer, the target was to reach a  $Y+$  value below 1 all over the surface of the propeller, in order to resolve the whole boundary layer and not

use wall functions. More in detail, the  $Y+$  represents the non-dimensional distance between the wall and the centroid of the first cell. The target  $Y+$  should be chosen considering the turbulence model adopted. The general procedure for determining the distance of the centroid of the first cell is the following: Firstly the Reynolds number is needed.

$$Re = \frac{\rho UL}{\mu} \quad (2.2)$$

Once the Reynolds is computed we calculate some viscous parameters.

$$C_f = [2\text{Log}_{10}(Re) - 6.5]^{-2.3} \quad (2.3)$$

$$\tau_w = \frac{1}{2}\rho V^2 C_f \quad (2.4)$$

$$u_\tau = \sqrt{\frac{\tau_w}{\rho}} \quad (2.5)$$

Finally the total height of the first cell is computed.

$$y_H = 2 \frac{y^+ \mu}{\rho u_\tau} \quad (2.6)$$

Once the first height is computed, we can determine the number of layers by computing the boundary layer total thickness. If  $Re < 5e + 5$ .

$$\delta_{BL} = \frac{4.91L}{\sqrt{Re_L}} \quad (2.7)$$

If  $Re > 5 \cdot 10^5$ :

$$\delta_{BL} = \frac{0.38L}{Re^{1/5}} \quad (2.8)$$

It is important to notice that if we adopt a full turbulent model, we have to calculate the boundary layer thickness with the second equation, even if the Reynolds number of the simulation is less than  $5 \cdot 10^5$ . Finally, selected a proper stretching factor ( $G$ ), we can compute the number of layers ( $N$ ).

$$\delta_{BL} = \sum_{k=0}^{N-1} y_H G^k = y_H \frac{1 - G^N}{1 - G} \quad (2.9)$$

In conclusion, a total of 10 layers with a near wall thickness of  $2 \cdot 10^{-5}$  m and a total thickness of 0.001 m has been selected as input values for the prism layer mesh. As can be seen in figure ??, the wall  $Y+$  values are well below 1 for most of the propeller surface.

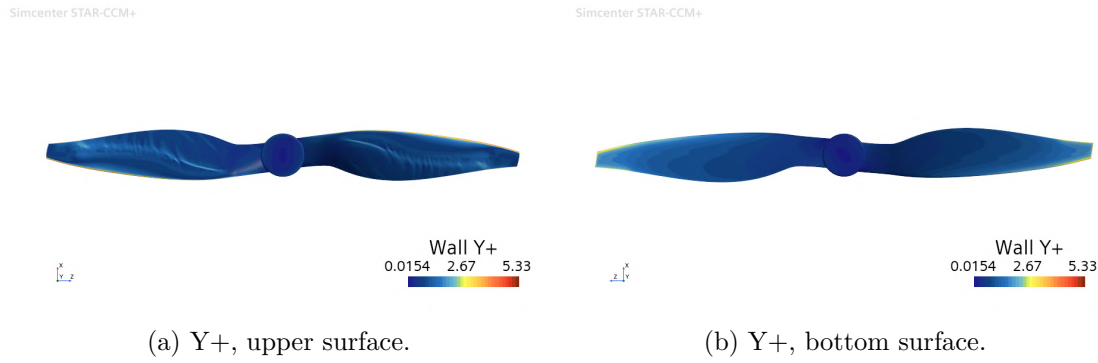


Fig. 2.8 Wall Y+ values.

In general, as we take in consideration some quality metrics, as skewness angle of the cells and cell quality index, the overall mesh quality is more than acceptable, see figure 2.9. Even if the mesh quality is high, the present mesh has a high number of cells, approximately 8.2 million if we consider *Dom1*. This considerations suggest a mesh independence study, in order to reduce the number of cells while maintaining the same quality.

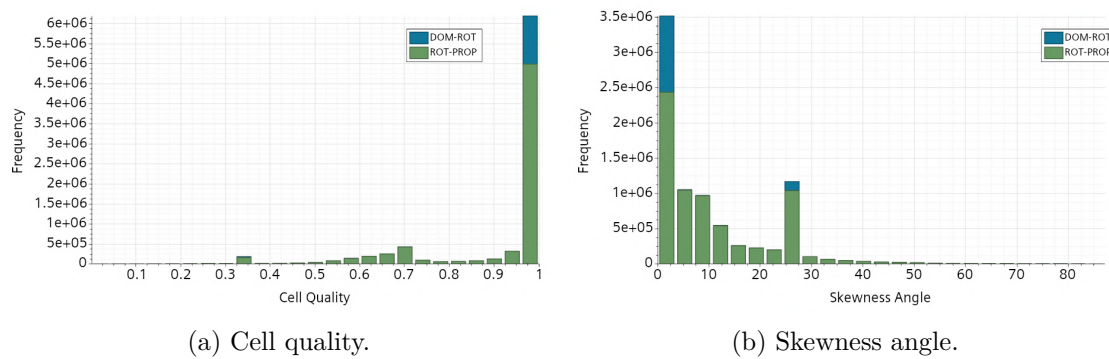


Fig. 2.9 Mesh quality metrics.

A grid independence study should be parametric, that is a parameter is varied while the others are fixed. Following this way, it is possible to study the dependence of the mesh on a specific parameter. In the present study the base size is chosen as the variable parameter.

Table 2.4 Mesh independence study.

	Base size	Number of cells	T [N]	$\epsilon$
Mesh1	$c/100$	8.16e6	0.4269	0
Mesh2	$c/80$	5.60e6	0.4231	0.89
Mesh3	$c/60$	3.57e6	0.4208	1.43
Mesh4	$c/40$	1.96e6	0.4101	3.93

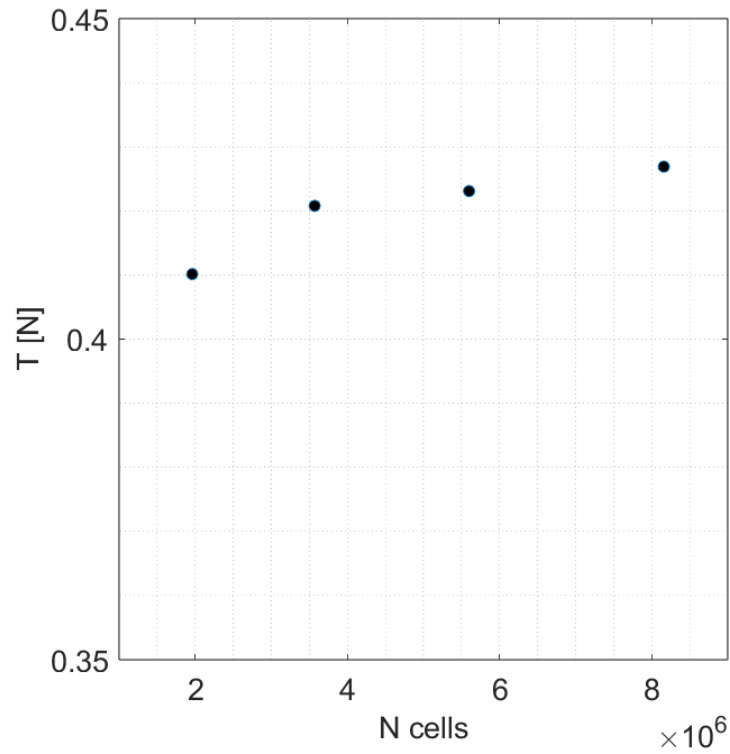


Fig. 2.10 Mesh independence study.

Figure 2.10 and table 2.4 show the results of the mesh independence study. Four different meshes have been tested, and it is clear that *Mesh2* represents a good compromise between computational costs and solution accuracy. For this reason it is possible to conclude that for a reliable numerical simulation, it is suggested to select the dimensions of the stationary domain according to table 2.1, in particular for dimension A, 3 to 4 diameters of the propeller should be selected, for dimension B, 4 to 5 diameters and for dimension C 7 to 10 diameters should work fine. Regarding the rotating domain size it has been proven that the size affects the results, this is particularly true for small dimensions, so a D dimension of 0.56 diameters and an E dimension of 0.23 diameters seems to be a good compromise. Finally, a base size of  $c/80$  it is suggested, in order to reduce the computational costs, saving more or less 2.5 million cells, with a difference of less than 1% in thrust with respect to the finest mesh.

# Chapter 3

## Wind tunnel characterization

### 3.1 Introduction

Wind tunnels are used to study the aerodynamic properties of objects in a controlled environment. They consist of a test section, where a model is placed, and a wind tunnel that generates a flow of air or other fluid over the model. The flow is then monitored and analyzed to determine the aerodynamic characteristics and performance of the object, such as drag, lift and pressure distribution.

Wind tunnels can be used to test a wide range of objects, from small models of aircraft, automobiles, and building structures, to large-scale models of industrial equipment and sports equipment. They are widely used in fields such as aeronautical and aerospace engineering, mechanical engineering, and sports science, to design and optimize the performance of various systems and products.

There are various types of wind tunnels, including open-circuit, closed-circuit, subsonic, supersonic, hypersonic, and transonic wind tunnels, each designed to test objects in different flow regimes. Open-circuit wind tunnels draw air in from the environment, while closed-circuit wind tunnels recirculate air through the tunnel.

In addition to testing physical models, wind tunnels can also be used to study numerical simulations and computational fluid dynamics (CFD) models. By comparing the results of these simulations with experimental data obtained in wind tunnels, engineers can validate and improve the accuracy of their simulation models.

Because of the critical role of wind tunnels in advancing the understanding of fluid dynamics and aerodynamics, in this chapter will be discussed the main features of "*Ferrari*" wind tunnel, an open circuit wind tunnel located in the "*Modesto Panetti*" laboratory, part of the Department of Mechanical and Aerospace engineering (DIMEAS) of the Polytechnic university of Turin. This wind tunnel has been used in this project in order to study the aerodynamics performance of a rotorblade in

different configurations and conditions. In particular, in this chapter we focus our attention on the wind tunnel characterization, that is the process of measuring and analyzing the properties of a wind tunnel, such as flow quality, speed, and turbulence, in order to ensure that it is operating within specified limits and is suitable for its intended use.

## 3.2 Ferrari wind tunnel

The wind tunnel consists of 1.14 meters long contraction with a contraction ratio of 3.5 : 1 with an inlet diameter of 0.75 meters and an exit jet diameter of 0.4 meters. The test section has a cubic shape with a length of 0.9 meters, while the diffuser has a diffusing ratio of 1 : 2.4. A 7 blades fan is mounted downstream the diffuser and it is run by a three-phase asynchronous motor with a maximum power of 7.5 kW. In the contraction section are mounted two metallic meshes to reduce the turbulence intensity of the flow. The wind speed range is approximately 2.5 – 25 m/s.

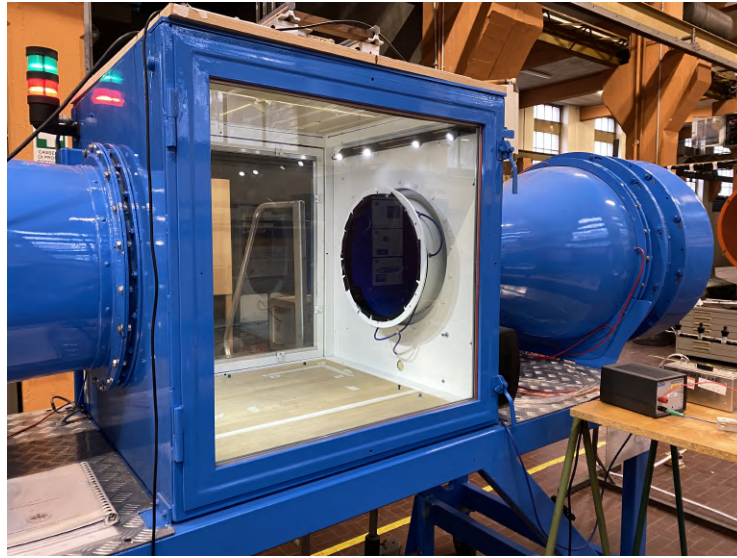


Fig. 3.1 Ferrari wind tunnel

In figure 3.2 it's shown the relation between the angular speed of the fan and the wind speed, and the relationship between the difference of pressure measured at the ring ( $\Delta P_{RG}$ ) and the pressure difference measured by the Pitot tube, that is ( $\Delta P_{PT}$ ). Figure 3.2 (a) is obtained by varying the fan rotational speed from 0 to 2200 round per minute. At each rotational speed the wind speed is obtained by means of a Pitot tube and a pressure transducer. The acquisition time has been settled to 60 seconds with an acquisition frequency of 16.7 Hz.  $\Delta P_{RG}$  represent the pressure difference at the ring, that is the difference of pressure measured in proximity of the inlet and the outlet of the convergent. Once the experimental data was obtained, a fitting curve

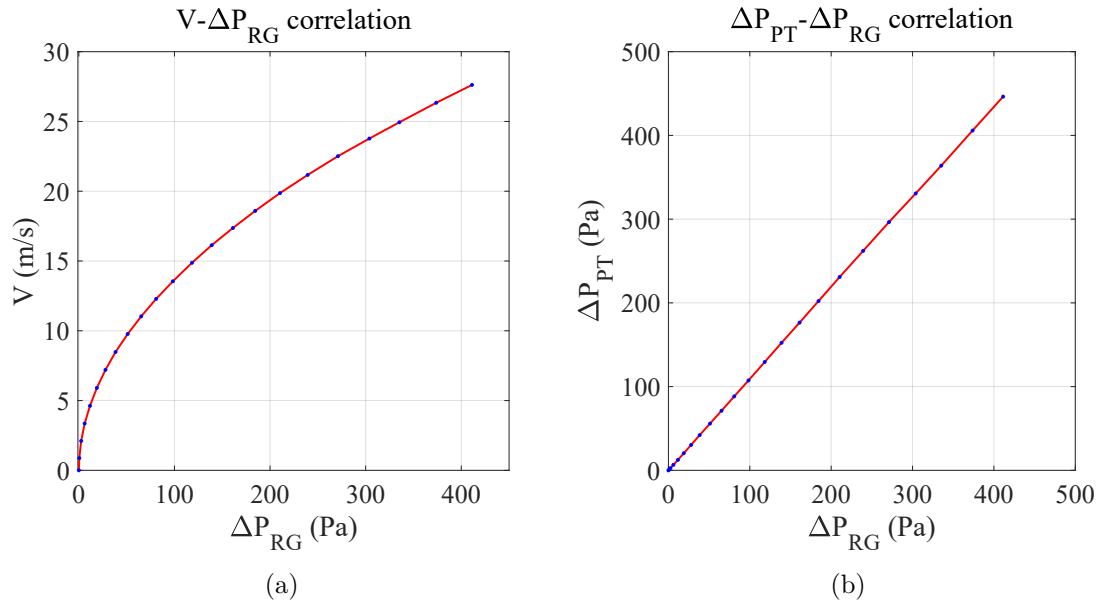


Fig. 3.2 Pressure and velocity correlations.

has been computed. In particular, the  $U - \Delta P_{RG}$  correlation can be expressed by the following expression:

$$U(\Delta P_{RG}) = \sqrt{1.8618 \cdot \Delta P_{RG}} \quad (3.1)$$

While  $\Delta P_{PT} - \Delta P_{RG}$  correlation can be expressed as:

$$\Delta P_{PT} = 1.0892 \cdot \Delta P_{RG} \quad (3.2)$$

### 3.3 Flow characteristics

In order to reach accurate and reliable results it is important to evaluate the flow characteristics of the wind tunnel, in particular in the test section, where the testing model is mounted. In this section we investigate the quality of the flow in terms of velocity profile, turbulence intensity profiles and turbulence power spectra.

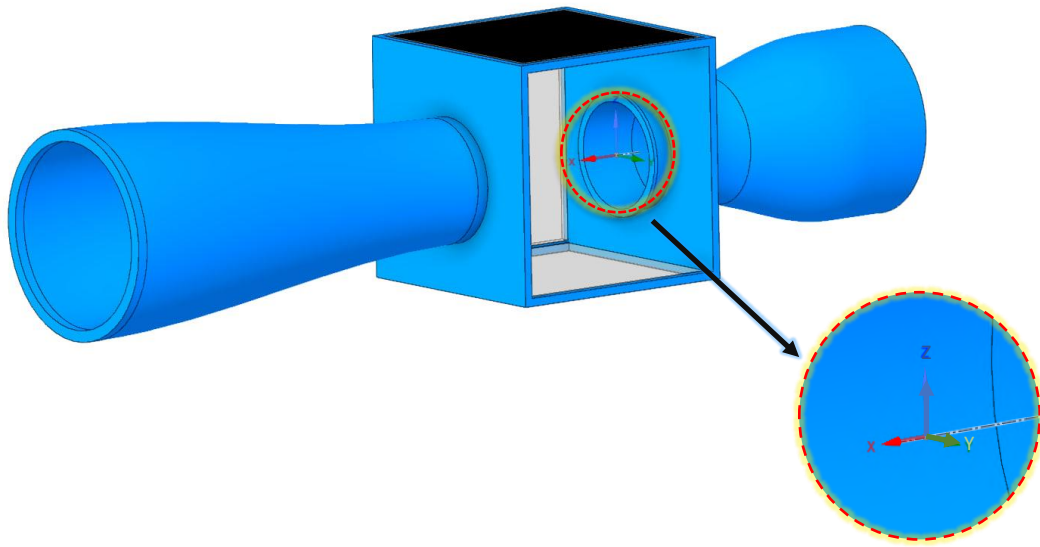


Fig. 3.3 Schematic of the wind tunnel and reference system. (red: x, blue: z, green: y).

The velocity profiles were obtained experimentally by using a hot-wire anemometer. In particular, the z and y profiles are derived for two different x positions in the test section, that are the outlet of the jet (position A) and the middle position respect to the test section (position B). To gain a better understanding, refer to figure 3.4.

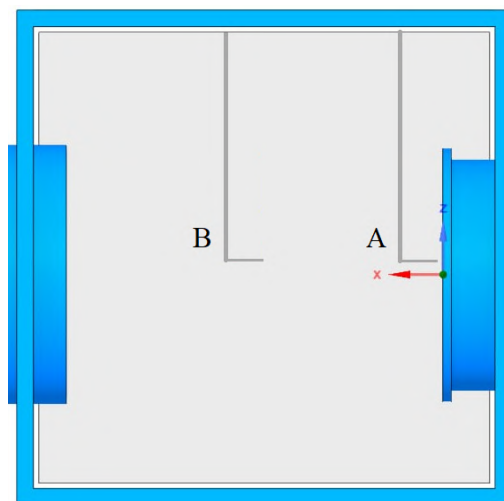


Fig. 3.4 Position A and B of the hot wire probe in the test section.

The velocity profiles in y and z direction were obtained by varying the distance of the hot-wire probe with respect to the x-z plane for the y profiles and to the x-y plane for the z profiles. The distance range in which the probe computed the velocity it is shown in figure 3.5 for both y and z profiles, and for position A and B. In particular, the range are:

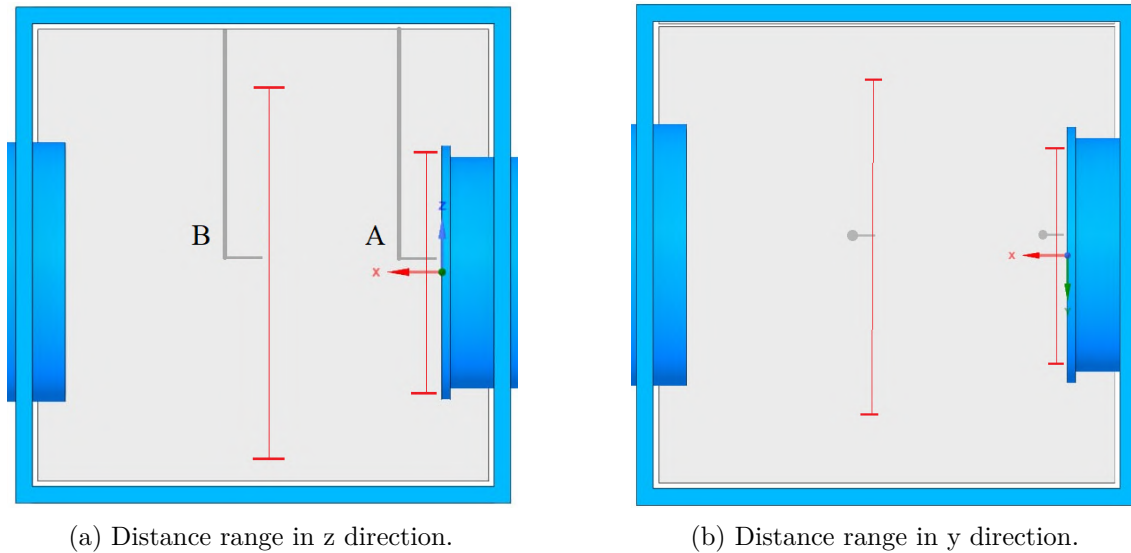


Fig. 3.5 Hot-wire probe operational distance range, in grey a schematic of the hot-wire probe.

- Position A:  $[-21.5 : 20.5]$  cm in the z direction and  $[-18 : 18]$  cm in the y direction;
- Position B:  $[-34 : 26]$  cm in the z direction and  $[-28 : 26]$  cm in the y direction;

In order to achieve reliable velocity profiles, the following procedure was adopted: Firstly the hot-wire calibration. In this phase we acquired the ring pressure values and then the voltage signal from the hot-wire. The acquisition time and frequency was settled to 60 seconds and 16.7 Hz for the pressure acquisition and 10 seconds and 25.6 kHz for the hot-wire acquisition. This phase was executed for the range of angular velocity of the fan, that is from 0 to 2200 round per minute, with an incremental step of 100 revolutions per minute. Once the signals were acquired, we calculated  $\Delta P_{RG}$  for each acquisition and computed an averaged wind speed. The same process of averaging was applied to the voltage signal from the hot-wire. In the end a 4<sup>th</sup> order polynomial was computed in order to fit the voltage-wind speed data obtained experimentally. Finally the hot-wire acquisition was performed. Once the hot-wire calibration was performed, the velocity profiles were obtained by varying the distance of the probe from the x-y plane and x-z plane by step of 2 cm. This process was executed for position A and B at a fan rotational speed of 500/900/1350/1800 revolutions per minute. In this case the hot-wire acquisition time was settled to 60 seconds, while the acquisition frequency remained unchanged with respect to the calibration process.

For a better comprehension of the results, here the following Reynolds decomposition is adopted:

$$U_i = \bar{U} + u' \quad (3.3)$$

where  $U_i$  is the instantaneous velocity,  $\bar{U}$  is the mean velocity and  $u'$  is the fluctuating part of the velocity field. The turbulence intensity ( $Ti$ ) is computed as follow:

$$Ti = \frac{(\overline{u'^2})^{1/2}}{\bar{U}} \quad (3.4)$$

As can be seen from figure 3.8, the turbulence intensity stays below 1% for a wide range, approximately 38 cm, in both y and z direction. Table 3.3 summarizes the flow characteristics in position A. In tables the quantity  $S$  represent the standard deviation of the velocity measures and it is computed as follow:

$$S = \sqrt{\frac{1}{N-1} \sum_{i=1}^N |U_i - \bar{U}|^2} \quad (3.5)$$

In equation 3.5,  $N$  represents the number of measures considered to evaluate the mean velocity, the mean turbulence intensity and the standard deviation. In this case  $N$  is 10, that are the points between -10 cm and 10 cm in both y and z profiles. This extent has been selected because the propeller will encounter the airstream within this specific range only. Some considerations are made for velocity and turbulence profiles in both A (jet exit) and B (test section center) position. For completeness, in table 3.1 is reported the corresponding Reynolds Number, calculated as equation 3.6 for each rotational speed of the wind tunnel fan.

$$Re = \frac{\bar{U}D}{\nu} \quad (3.6)$$

Table 3.1 Reynolds numbers (D = 40 cm).

$\Omega$ (rpm)	$\bar{U}$ (m/s)	Re
500	5.87	156000
900	10.92	291200
1350	16.55	441330
1800	22.18	591470

The velocity profiles and turbulence profiles shown below have a similar trend to those already present in the literature, see for example [28]. Here, each color corresponds to a specific fan rotational speed: purple 500 rpm, orange 900 rpm, blue 1350 rpm and green 1800 rpm. The velocity profiles in position A appear very straight in a range of about 38 cm, in fact this region can be interpreted as the potential core of the jet, a particular region where the wind speed is uniform and irrotational. Outside of the potential core a wind speed reduction occurs, due to the

presence of the shear layer; this hypothesis is confirmed by an increase in magnitude of turbulence intensity.

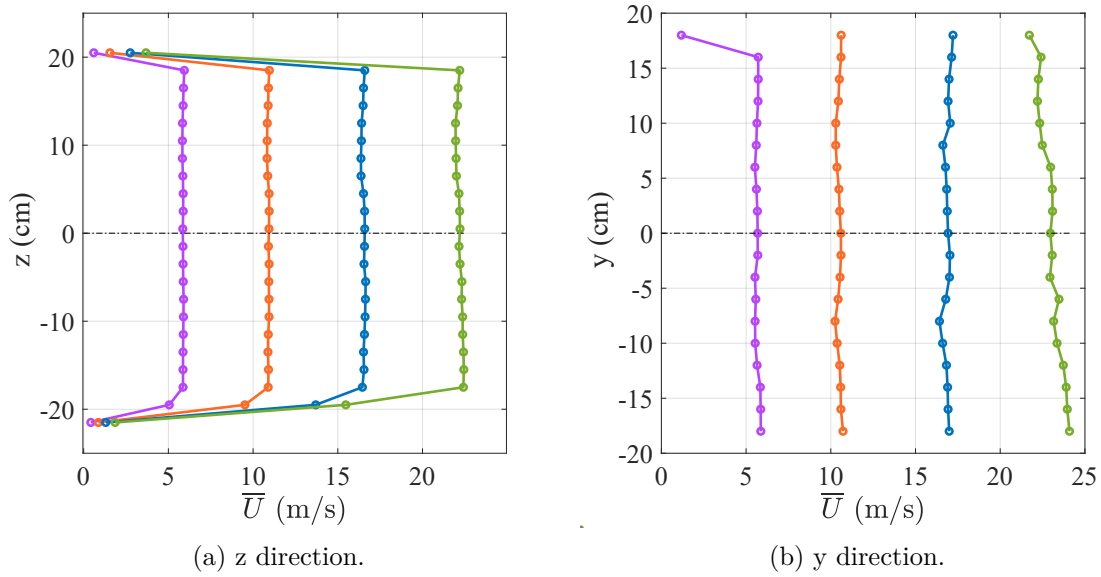


Fig. 3.6 Velocity profiles, position A (Purple: 500 rpm, orange: 900 rpm, blue: 1350 rpm, green: 1800 rpm).

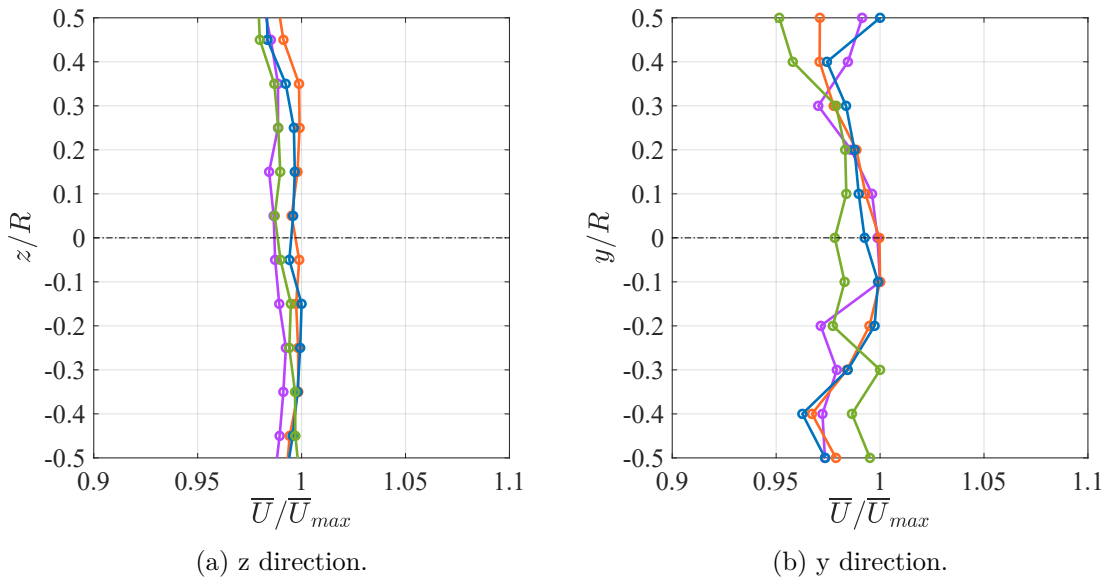


Fig. 3.7 Non-dimensional velocity profiles, position A (Purple: 500 rpm, orange: 900 rpm, blue: 1350 rpm, green: 1800 rpm).

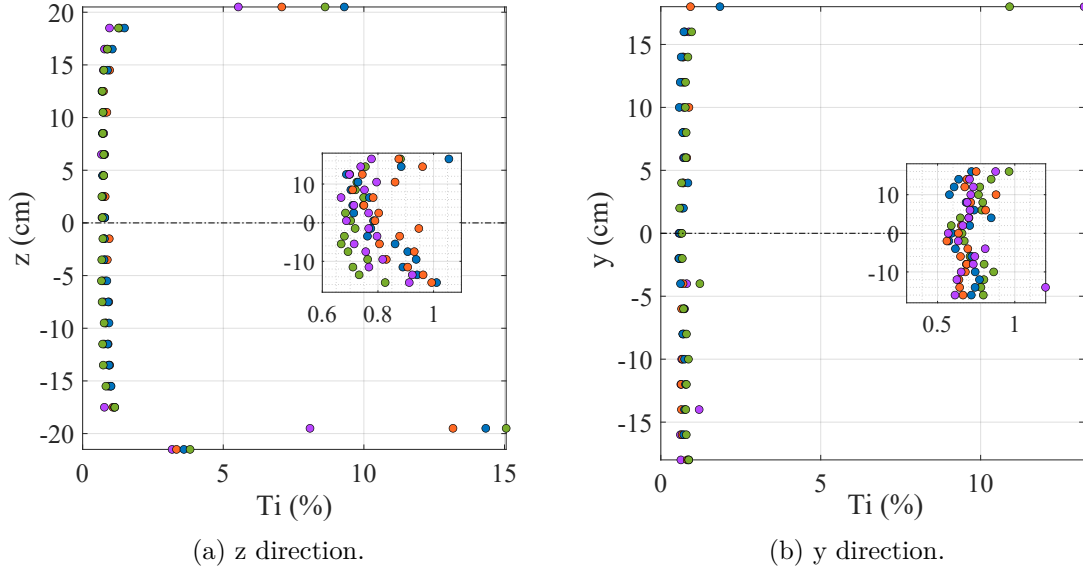


Fig. 3.8 Turbulence intensity profiles, position A (Purple: 500 rpm, orange: 900 rpm, blue: 1350 rpm, green: 1800 rpm).

Table 3.2 Summary of the flow characteristics in A

$\Omega$ (rpm)	z direction			y direction		
	$\bar{U}$ (m/s)	S (m/s)	$\bar{Ti}$ (%)	$\bar{U}$ (m/s)	S (m/s)	$\bar{Ti}$ (%)
500	5.87	0.011	0.707	5.61	0.072	0.689
900	10.92	0.031	0.768	10.51	0.087	0.673
1350	16.55	0.086	0.822	16.89	0.102	0.685
1800	22.18	0.098	0.730	23.01	0.182	0.755

The same considerations made for position A can be extended to the profiles in position B. The geometry of the velocity and turbulence profiles slightly change from those in position A (figures 3.9, 3.11), this difference is mainly due to the increased distance from the outlet of the jet, from where the potential core progressively contracts reducing its width. In this case the velocity profile appears well straight in a range of about 26 cm, and the turbulence intensity remains under 2% in a range of about 20 cm. These results highlight an increase in turbulence intensity away from the jet exit.

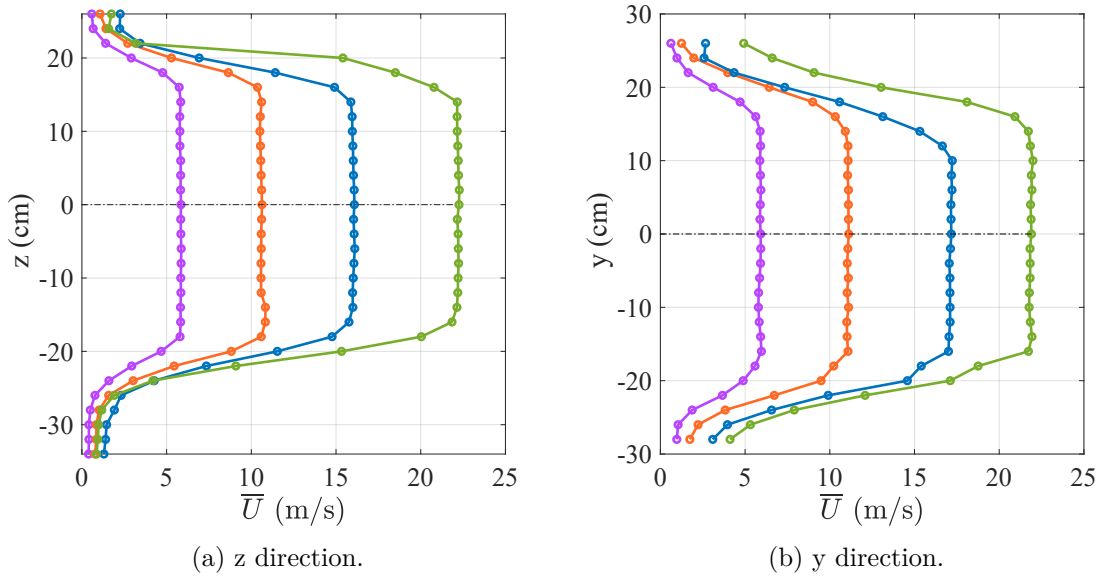


Fig. 3.9 Velocity profiles, position B (Purple: 500 rpm, orange: 900 rpm, blue: 1350 rpm, green: 1800 rpm).

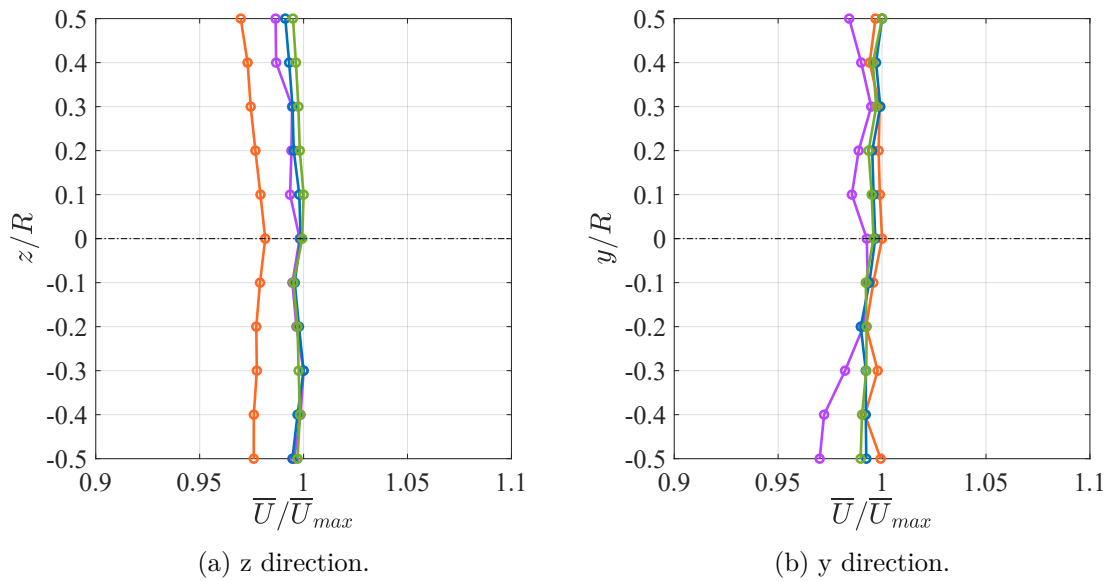


Fig. 3.10 Non-dimensional velocity profiles, position B (Purple: 500 rpm, orange: 900 rpm, blue: 1350 rpm, green: 1800 rpm).

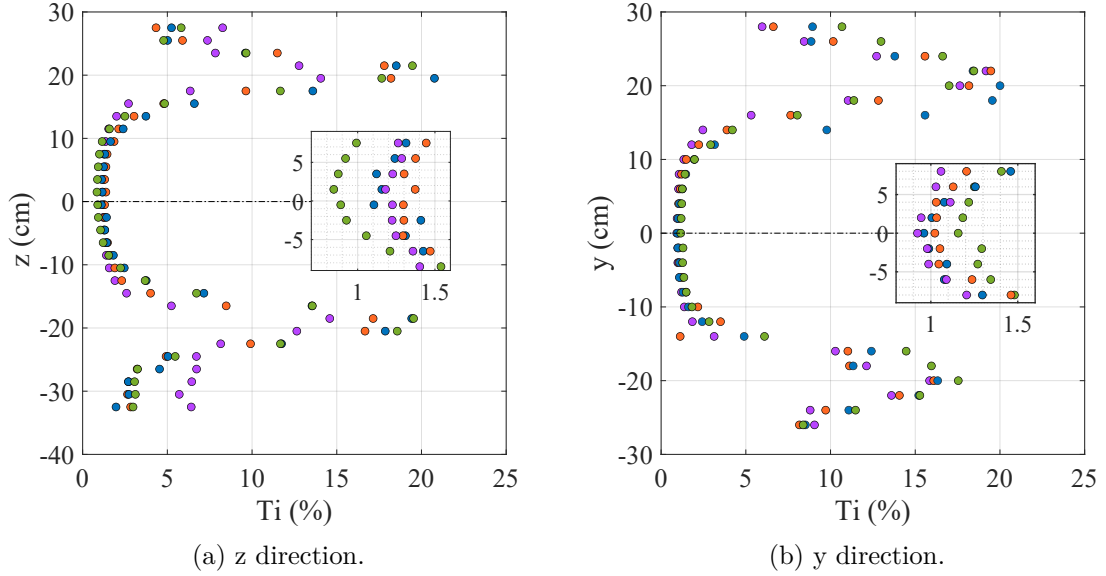


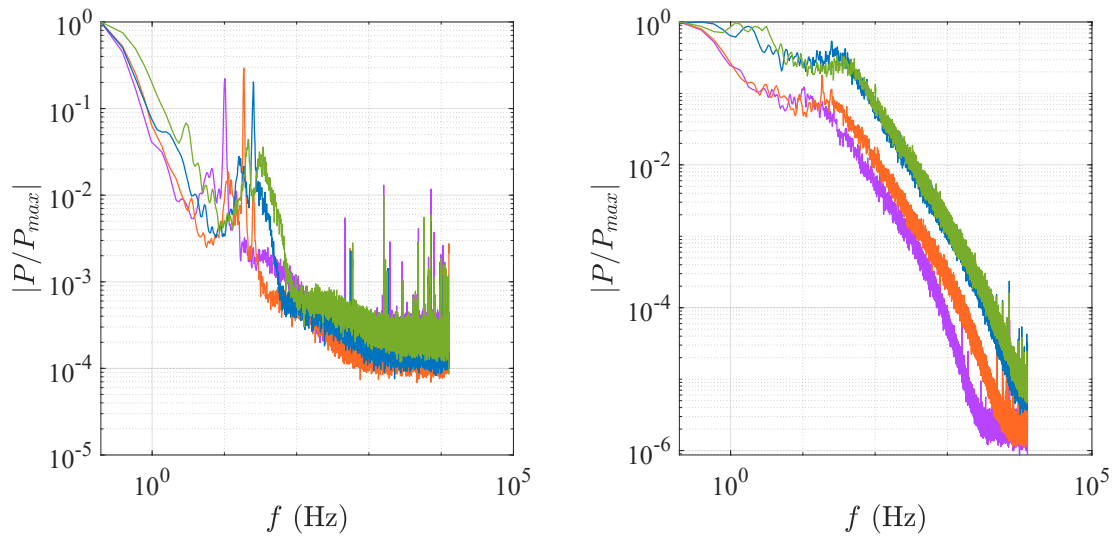
Fig. 3.11 Turbulence intensity profiles, position B (Purple: 500 rpm, orange: 900 rpm, blue: 1350 rpm, green: 1800 rpm).

Table 3.3 Flow characteristics in B

$\Omega$ (rpm)	z direction			y direction		
	$\bar{U}$ (m/s)	S (m/s)	$\overline{Ti}$ (%)	$\bar{U}$ (m/s)	S (m/s)	$\overline{Ti}$ (%)
500	5.84	0.014	1.249	5.90	0.027	1.009
900	10.59	0.024	1.343	11.09	0.029	1.079
1350	16.06	0.031	1.252	16.55	0.053	1.065
1800	22.22	0.038	0.961	21.87	0.043	1.245

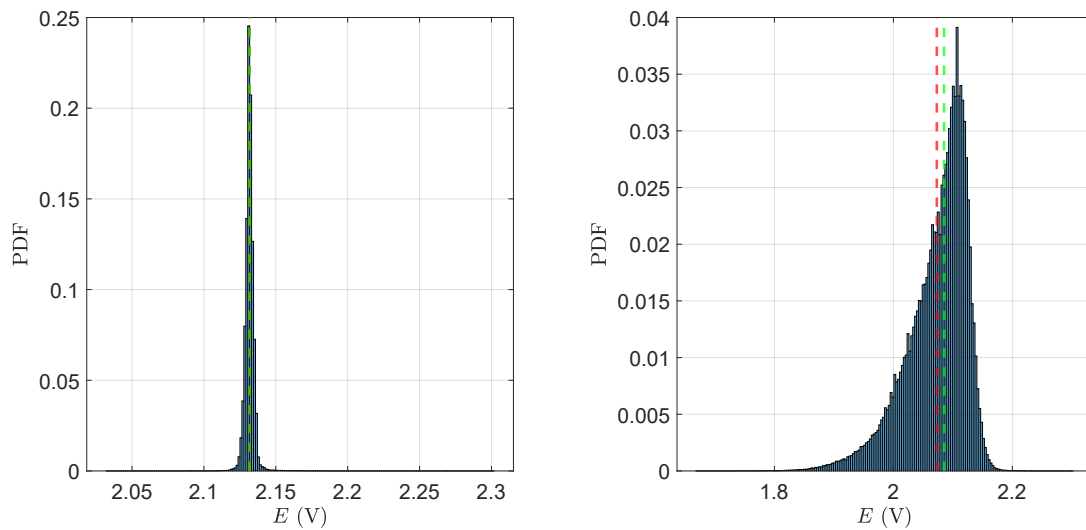
Below are shown the turbulence velocity spectra obtained at position B, focusing specifically on the potential core of the jet and the shear layer region, covering all the velocity values mentioned earlier. The values have been normalized with respect to the maximum power obtained, in order to make the trends comparable. In more detail, figure 3.12 (a) shows the spectrum at a point within the potential core. In this case, a rapid decrease in power is observed even at low frequencies, highlighting the absence of particularly large and energetic turbulent structures in the flow. The peaks, on the other hand, represent the rotational frequency of the wind tunnel fan blades. Observing figure 3.12 (b), it is possible to notice a classic trend of a turbulent spectrum, characterized by a plateau at low frequencies, indicative of large scales, and a rapid descent with a slope of  $-5/3$ , representative of the inertial sub-range. Alongside the spectra, probability density functions have been provided for the same points, but this time only for a specific rotational speed value, that is 500 rpm. Along with the probability density functions, to better characterize the

distribution, some characteristic parameters such as skewness and flatness have been calculated.



(a) Turbulence power spectra in the potential core region. (b) Turbulence power spectra in the shear layer core region.

Fig. 3.12 Turbulence power spectra, position B (Purple: 500 rpm, orange: 900 rpm, blue: 1350 rpm, green: 1800 rpm).



(a) PDF potential core. In red the mean, in green the median of the data. (b) PDF shear layer. In red the mean, in green the median of the data.

Fig. 3.13 Probability density function, 500 rpm.

In particular, skewness and flatness are defined as follow:

$$S = \frac{\overline{u^3}}{(\overline{u^2})^{3/2}} \tag{3.7}$$

$$F = \frac{\overline{u'^4}}{(\overline{u'^2})^2} \quad (3.8)$$

By analyzing the distribution in the potential core, it can be seen that it is very steep and peaked around the mean, these results further highlight how turbulence is very low in the potential core. Whereas in the case of the shear layer, the skewness is negative equal to -1.18, while the flatness is positive with a value of 4.83, indicating a flatter distribution characterized by signal intermittency and so turbulent motion.

### 3.4 Considerations on the flow quality and model positioning

The purpose of characterizing the flow in the wind tunnel was to guide the model positioning in the test section and to ensure that certain critical flow quality parameters, such as the turbulence intensity and the flow uniformity, were satisfactory for our purpose. The results highlight a large potential core zone with an average turbulence intensity below 1%. The velocity profiles, particularly the non-dimensional profiles shown in Figure 3.14, demonstrate a uniform flow throughout the region affected by the presence of the examined propeller, both along the y-direction and the z-direction.

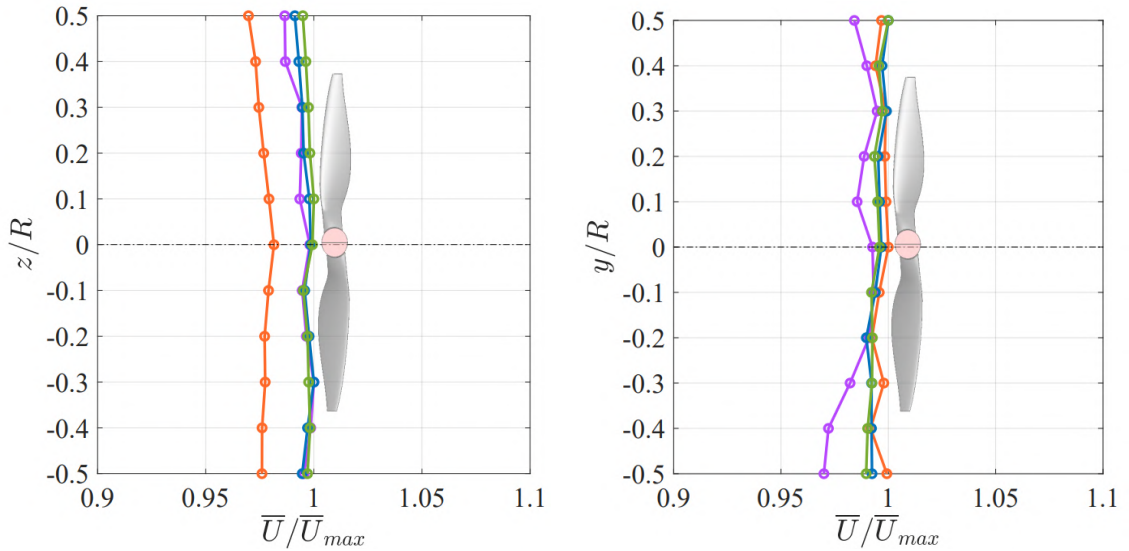


Fig. 3.14 Non-dimensional mean velocity profiles in center test section compared with propeller size.

In conclusion, the decision to position the rotor and the entire setup in the central region of the test section was based on careful consideration. The choice was deemed reasonable due to the favorable flow quality observed in that specific zone, along with the convenient accessibility it offered for the PIV setup. These factors

played a crucial role in ensuring reliable and accurate measurements throughout the experimental process.

# Chapter 4

## Results

### 4.1 Introduction

In this chapter both experimental and numerical results will be discussed. In particular, in section 4.2.1 a comparison of Thrust and Torque between numerical and experimental analysis, for the hovering condition, is presented. Finally, in section 4.2.3 are reported the mean fields in the wake.

### 4.2 Hovering performance

In the present section the hovering performance at various Reynolds numbers will be investigated. In particular, in subsection 4.2.1 the influence of the Reynolds number on the thrust and torque will be analyzed, in subsection 4.2.2 the distribution of the wall shear stress on the blade will be used to investigate separated flow regions; finally, in subsection 4.2.3 the effect of the Reynolds number on the wake topology and mean flow field quantities will be discussed.

#### 4.2.1 Thrust and Torque

Thrust and torque results, both numerical and experimental, at different rotational speeds are discussed and compared. In figure 4.1, thrust (left) and torque (right) are shown as a function of rotational speed of the propeller. From these figures it is possible to notice a good agreement between numerical and experimental data. Table 4.1 summarizes the relative error of the numerical value with respect to the experimental ones.

Table 4.1 Numerical vs. experimental comparison for thrust and torque prediction.  $\Omega$  is the rotational speed,  $T_e$  is the thrust obtained experimentally and  $T_n$  is the thrust obtained numerically. The same nomenclature is applied for the torque  $Q$ .

$\Omega$ [rpm]	$T_e$ [N]	$T_n$ [N]	$\epsilon_T$ [%]	$Q_e$ [Nm]	$Q_n$ [Nm]	$\epsilon_Q$ [%]
2000	0.0559	0.0630	12.7	8.001e-4	8.825e-4	10.2
3610	0.2093	0.2181	4.15	0.0027	0.0029	5.99
7020	0.8544	0.8708	1.91	0.0104	0.0104	0.44

Observing table 4.1 it is possible to see an increase in  $\epsilon_T$  (thrust error) and  $\epsilon_Q$  (torque error) while decreasing the rotational speed of the propeller, this behaviour can be attributed to the large uncertainty of the load and torque cell at these operational regimes.

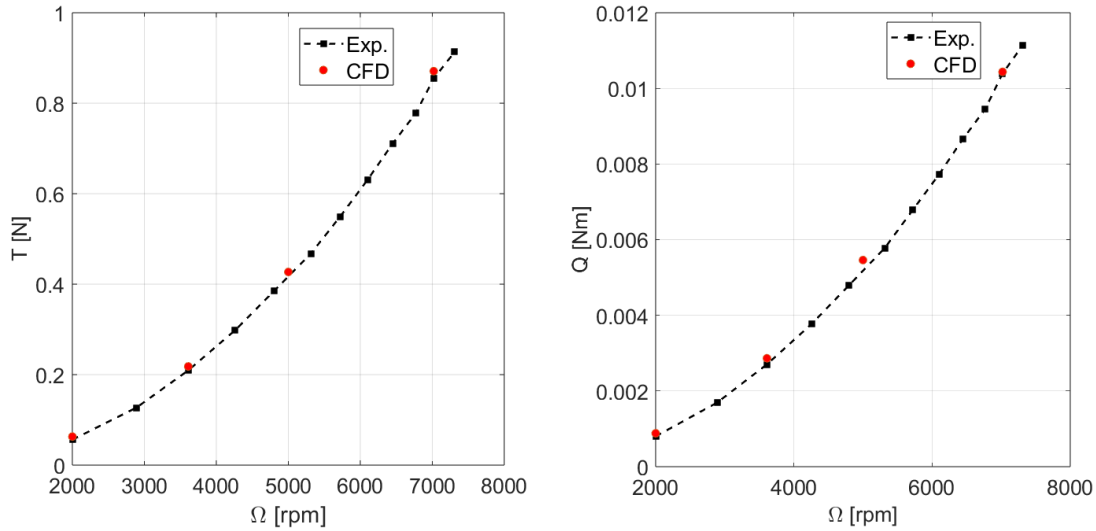


Fig. 4.1 Thrust and torque as a function of rotational speed.

Thrust and torque values can be normalized in order to estimate the thrust coefficient (eq. 4.1) and the torque coefficient (eq. 4.2). Another important parameter is the power coefficient, defined in eq. 4.3.

$$C_T = \frac{T}{\rho D^4 (\Omega/60)^2} \quad (4.1)$$

$$C_Q = \frac{Q}{\rho D^5 (\Omega/60)^2} \quad (4.2)$$

$$C_P = \frac{2\pi \frac{\Omega}{60} Q}{\rho D^5 (\Omega/60)^3} = \frac{P}{\rho D^5 (\Omega/60)^3} \quad (4.3)$$

In the literature some authors prefer to make their considerations with  $C_Q$ , while others with  $C_P$ , but they are both a measure of the power consumption of the propeller. In this thesis the  $C_Q$  is preferred.

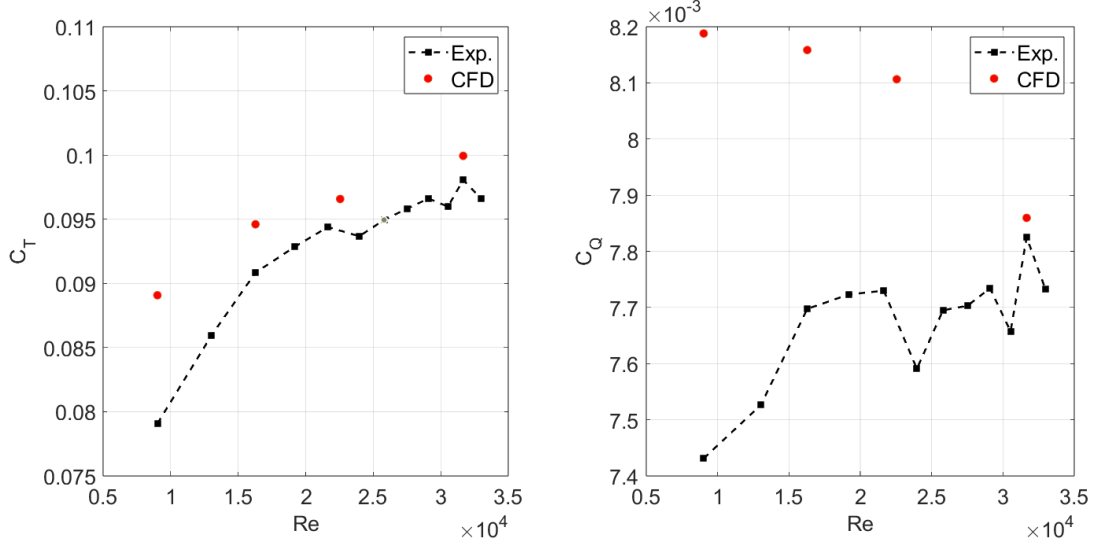


Fig. 4.2 Thrust and torque coefficients as a function of Reynolds number.

The forces acting on a single blade element at a radius  $r$  from the propeller center of rotation, are presented as:

$$dT = dL \cos(\phi + \alpha_i) - dD \sin(\phi + \alpha_i) \quad (4.4)$$

$$dQ = r [dL \sin(\phi + \alpha_i) + dD \cos(\phi + \alpha_i)] \quad (4.5)$$

Equations 4.4 and 4.5 derive from the blade element theory. In this theory the blade is divided into infinite elements along the radius, as represented in figure 4.3. Each element contributes to the integral forces and moments acting on the blade.

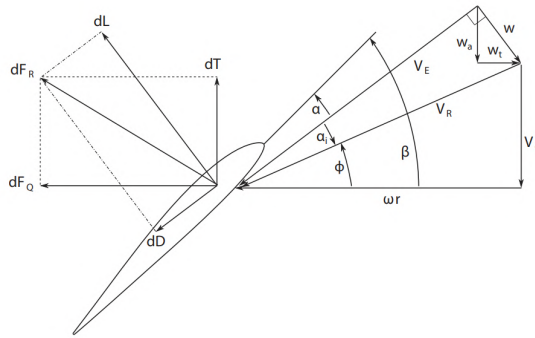


Fig. 4.3 Blade element [14].

It is known that an increase in the Reynolds number, and so the rotational speed of the propeller, will increase the lift coefficient (until stall occurs) and decrease the drag coefficient of a generic airfoil of the blade. Referring to equation 4.4, both an increase in  $C_L$  and a decrease in  $C_D$  is beneficial for the thrust coefficient, this is also supported by figure 4.2 (left) which shows the  $C_T$  as a function of the Reynolds number obtained numerically and experimentally. As it can be seen, the Reynolds effect on the  $C_T$  is more pronounced at low rotational speeds. Increasing the rotational speed the  $C_T$  grows, but then seems to reach an asymptotic value around 0.1. Regarding the torque coefficient, and so the power consumption, a decrease in drag is beneficial, but this is not true for an increase in lift. From figure 4.2 (right) it is possible to see an increase in  $C_Q$  for the experimental data and a decrease for the numerical ones with increasing the Reynolds number. This different behaviour can be attributed to the substantial difference between numerical and experimental approaches: in the latter the blade is a physical entity. In fact, during the experiments an important bending of the blades was noticed; this bending could cause an increase of the twist of the blade, with the final result of an increase in the pitch. This pitch increase cause an increase in  $C_L$  and  $C_D$  and so, recalling eq. 4.5, the final effect of an increase in  $C_Q$ .

For a better understanding of the performance of the propeller in hover at different Reynolds numbers, the  $C_T$  and  $C_Q$  distributions along the blade radius are reported in figure 4.4.

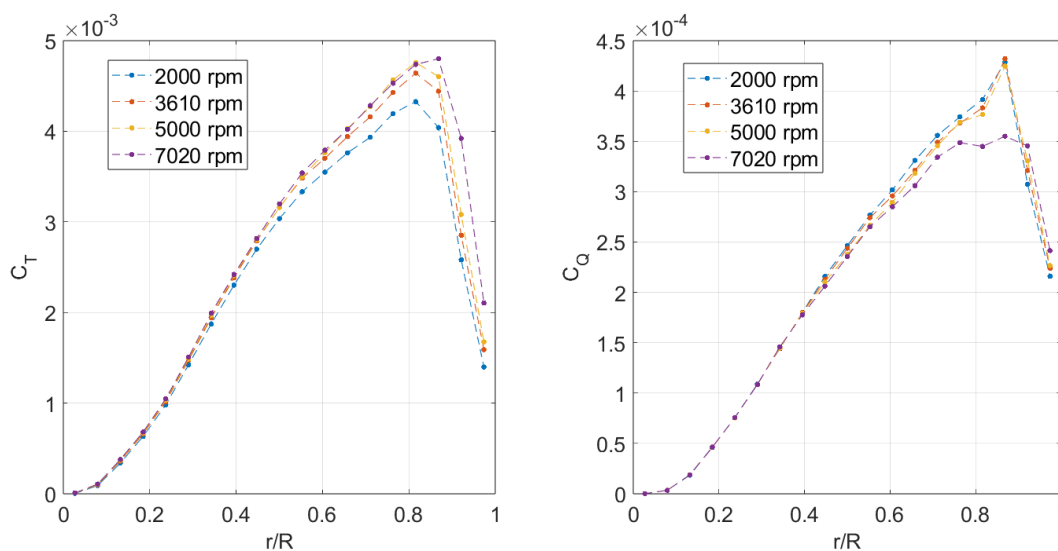


Fig. 4.4  $C_T$  (left) and  $C_Q$  (right) distribution along the half-span.

As it can be seen, the thrust and torque coefficients increase along the propeller radius until approximately 85% of the radius, where a maximum is reached. The increase in  $C_T$  can be attributed to the linear increase in radial velocity, and so the

Reynolds number, and by the presence of the tip vortex that increase the incidence for that specific section of the blade. These considerations can also explain the increase in  $C_T$  increasing the rotational velocity. After the maximum, the  $C_T$  collapses quickly due to the stall of the blade near the tip. The behaviour of the torque coefficient along the blade semi-span follows a similar trend, in this case at lower Reynolds the blade experiences an higher  $C_Q$  for almost all of the sections considered.

A better comprehension of the trends reported above can be achieved analyzing the lift and drag coefficient distribution along the blade. For this reason it is essential to determine the inflow angle distribution ( $\phi + \alpha_i$  in figure 4.3). For this purpose, a method for the prediction of the inflow angle has been used [15]. This method is based on the analysis of the velocity flowfield from the CFD computation. The idea is to obtain the induced axial velocity at the rotor plane using several planes upstream and downstream of the propeller disk. In particular, four planes perpendicular to the propeller axis of rotation (2 upstream and 2 downstream) have been selected. Each plane was discretized in many annulus and then each annulus has been averaged in terms of axial velocity. Once the axial velocities are known for all of the discretized and averaged planes (now we have a line), the values at the rotor plane can be estimated by using the Lagrangian Polynomial interpolation. A schematic of the method is reported in figure 4.5

$$V_{ax}(z_0) = \sum_{i=1}^N \left[ V_{ax}(z_i) \left( \prod_{j=1, j \neq i}^N \frac{z_0 - z_j}{z_i - z_j} \right) \right] \quad (4.6)$$

In this case  $V_{ax}(z_0)$  is the axial velocity value at the disk.

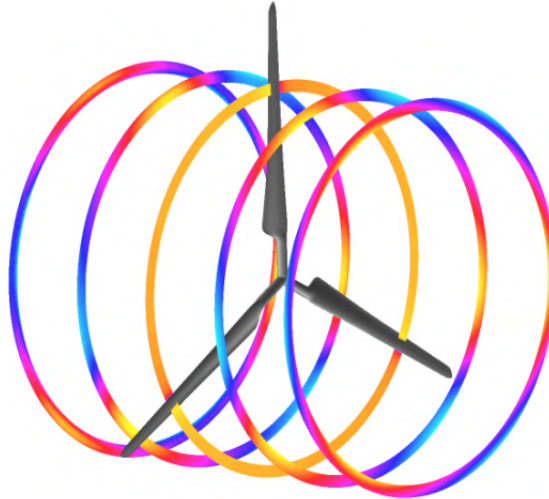


Fig. 4.5 Schematic of the method [15].

The axial velocity distribution at the disk then has been used for computing the inflow angle  $\phi + \alpha_i$ . The distribution of the inflow angle along the blade semi-span is reported in figure 4.6

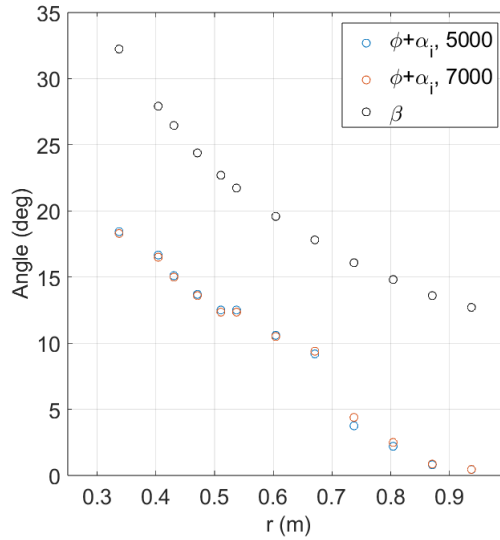


Fig. 4.6 Inflow angle in Hover for 5000 and 7000 rpm.

Once the inflow angle has been computed, it is easy to obtain the lift and drag coefficient distribution along the blade. The infinitesimal lift and drag for each discretized portion of the blade:

$$dL = \frac{1}{2}\rho W(r)^2 Cl c(r) dr \quad (4.7)$$

$$dD = \frac{1}{2}\rho W(r)^2 Cd c(r) dr \quad (4.8)$$

Where  $W(r)$ :

$$W(r) = \sqrt{(\Omega r)^2 + V_{ax}^2} \quad (4.9)$$

And finally the lift and drag coefficients:

$$Cl = \frac{dL}{0.5\rho W(r)^2 c(r) dr} \quad (4.10)$$

$$Cd = \frac{dD}{0.5\rho W(r)^2 c(r) dr} \quad (4.11)$$

In this case, we already have  $dT$  (infinitesimal thrust) and  $dF_Q$  (infinitesimal force responsible of torque), we can use these values for determining  $dD$  and  $dL$ :

$$dD = dF_Q \cos(\phi + \alpha_i) - dT \sin(\phi + \alpha_i) \quad (4.12)$$

$$dL = \frac{dT + dD \sin(\phi + \alpha_i)}{\cos(\phi + \alpha_i)} \quad (4.13)$$

By substituting these values in eq. 4.10 and 4.11 we can compute  $C_l$  and  $C_d$  along the blade span.

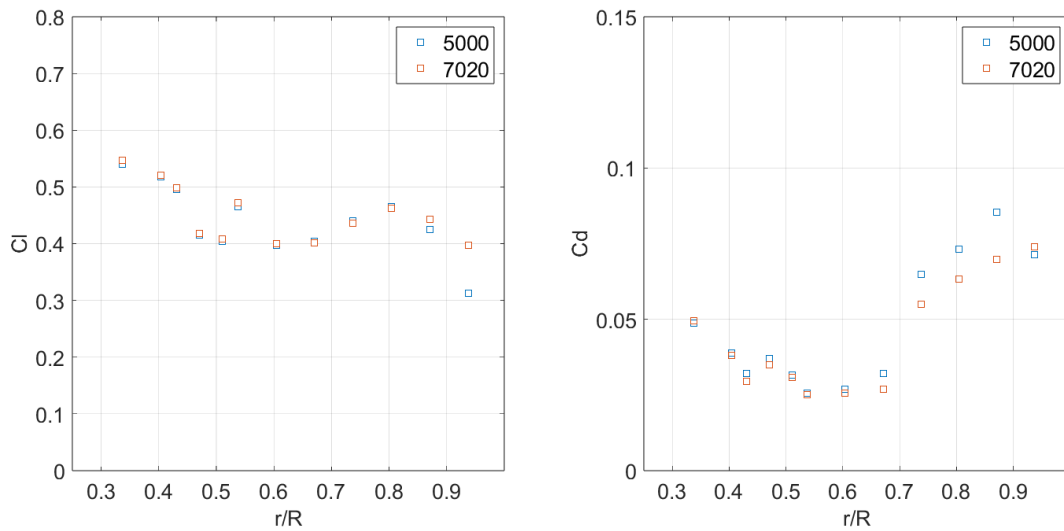


Fig. 4.7  $C_l$  and  $C_d$  distributions along the blade span for different rotational speed.

Observing figures 4.7 it is confirmed that an increase in the Reynolds number reduces the  $C_d$  along the blade, while the  $C_l$  is nearly constant. The trend in  $C_l$  and  $C_d$  confirms the hypothesis of an increase in thrust coefficient and a reduction in torque coefficient increasing the Reynolds number.

A reduction in thrust and an increase in power as the Reynolds number decreases results in a reduced efficiency for a propeller. In fact, as previously explained, a decrease in the Reynolds number causes a decrease in the lift coefficient and an increase in the drag coefficient of the generic airfoil of the blade. This sensitivity with the Reynolds number can be attributed to the behaviour of the boundary layer; at this regimes a laminar separation bubble is formed on the low pressure side of the blade. The size of the laminar separation bubble will affect these coefficients, in particular, the bubble grows in size as the Reynolds number decreases. The investigation of the influence of the separation bubble on the performance of the propeller will be discussed in the next section.

### 4.2.2 Wall flow features

In this section the influence of the Reynolds number on the rotor performance in hover is investigated. A typical parameter used for investigate the performance of a rotor is the power loading (PL) defined in chapter 2 and here recalled:

$$PL = \frac{T}{P} \quad (4.14)$$

$$PL_{id} = \left( \frac{T}{2\rho A} \right)^{-1/2} \quad (4.15)$$

Where A is the disk area, and  $PL_{id}$  the ideal power loading. Figure 4.8 shows the power loading as a function of disk loading ( $TD=T/A$ ).

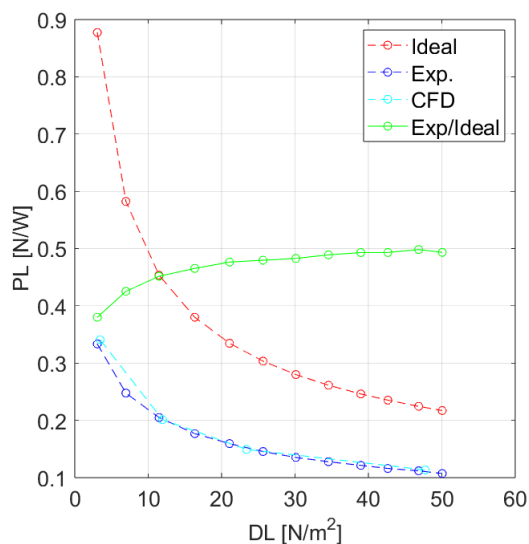


Fig. 4.8 Power loading as a function of disk loading.

As it can be seen, the ratio between experimental and ideal power loading highlights a negative trend reducing the disk loading, i.e the thrust. This behaviour can be attributed to an increase in power consumption at low Reynolds regimes, due to the viscous effects.

The hypothesis of a power increase due to viscous effects can be supported by analyzing the wall shear stress distribution on the blade surface; this quantity can be used for the identification of separated flow regions. Figures 4.9, 4.10 and 4.11 shows the wall shear stress distribution in the chord direction for upper and lower surface of the blade, at different rotational velocities. Observing the figures, it can be noticed a region where the flow is separated from the blade surface. In the 2000 rpm case, the flow separates and then it is unable to reattach due to the low kinetic energy of the flow. Increasing the rotational velocity, the flow separates and then reattaches in the portion of the blade from the root to mid-span. The extension of the reattachment

region seems to increase with the rotational speed, and so the Reynolds number. Regarding the lower surface, for these conditions, the flow is always attached to the surface.

For a better comprehension of the wall shear stress distribution in the x direction, three locations along the span has been selected: one near the root, one in the mid and one close to the tip, as can be seen in figure 4.12. Figures 4.13, 4.14 and 4.15 show the results for 2000 rpm and 7020 rpm only.

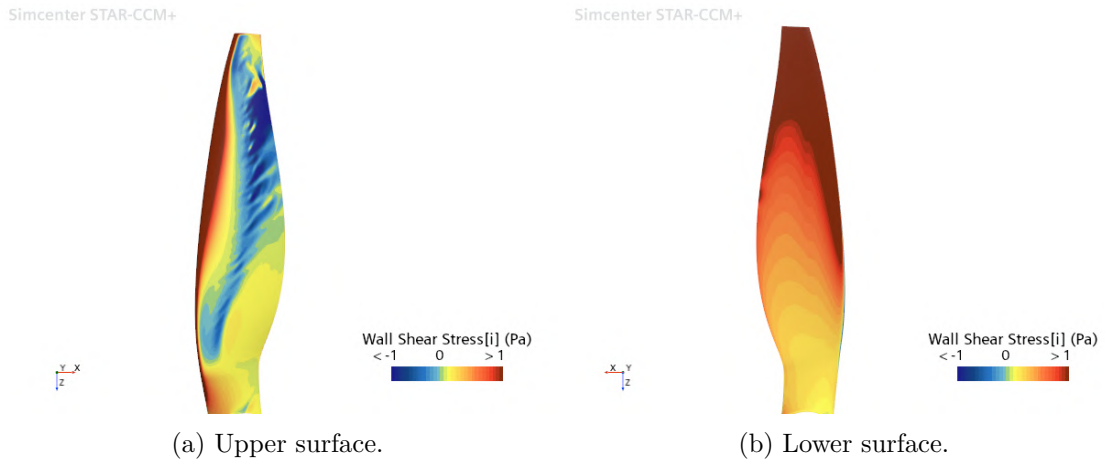


Fig. 4.9 Wall shear stress, 2000 rpm.

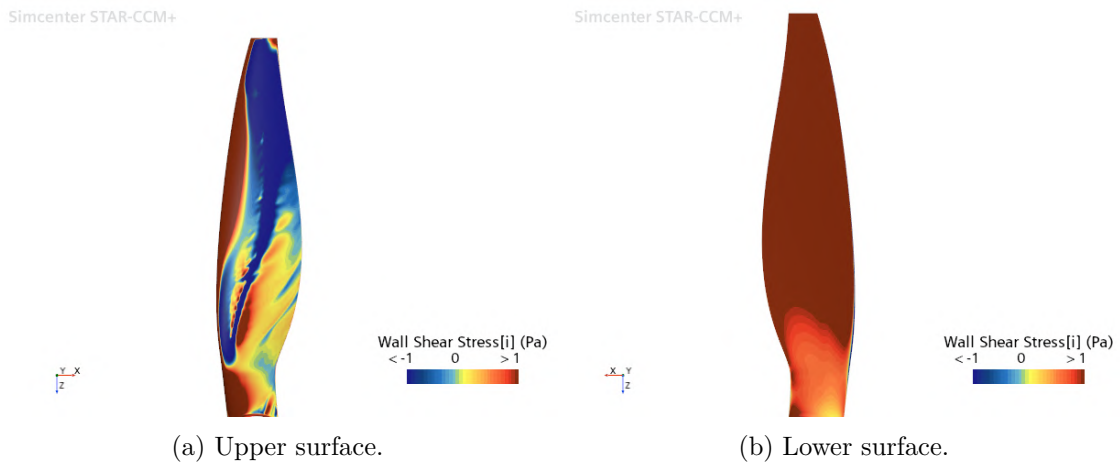


Fig. 4.10 Wall shear stress, 5000 rpm.

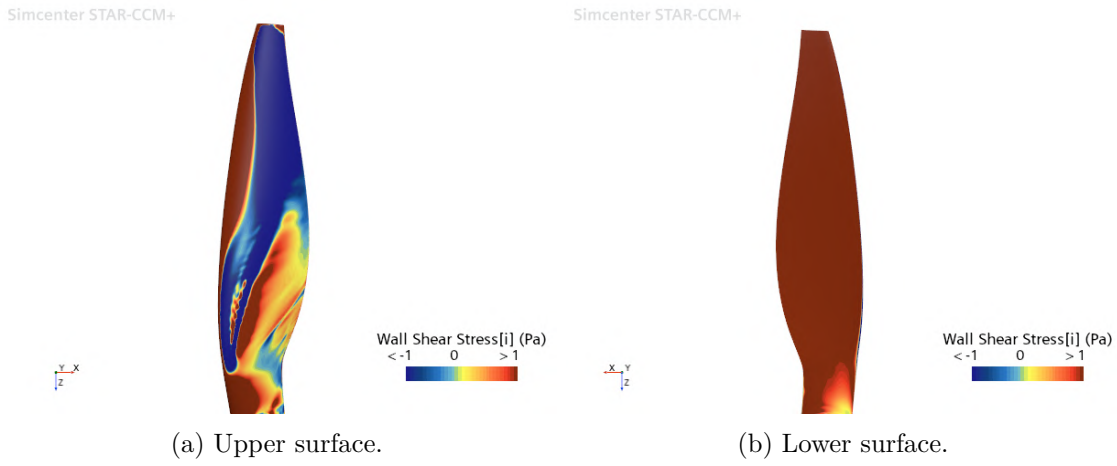


Fig. 4.11 Wall shear stress, 7020 rpm.

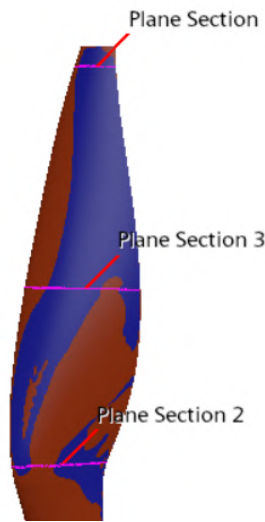


Fig. 4.12 Planes location along the blade span.

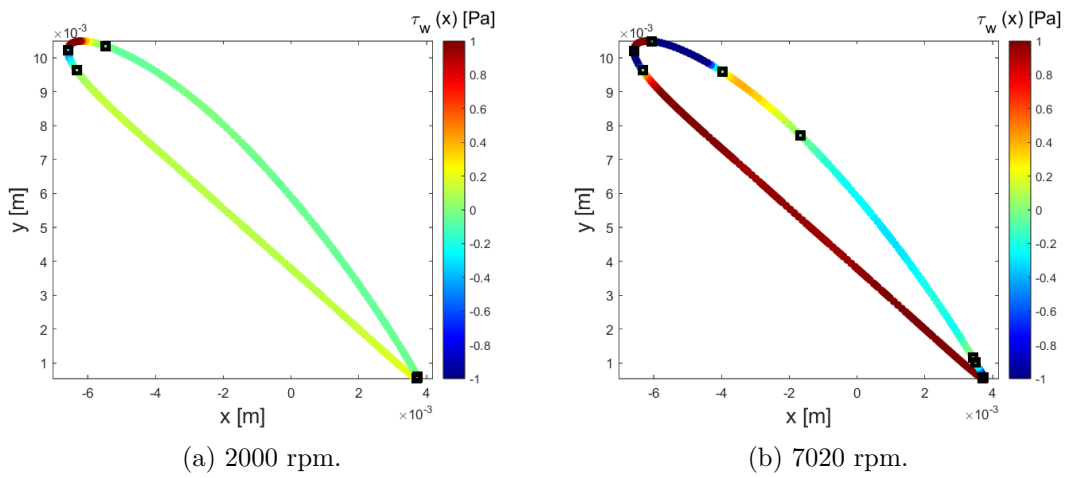


Fig. 4.13 Wall shear stress (x direction) at the root.

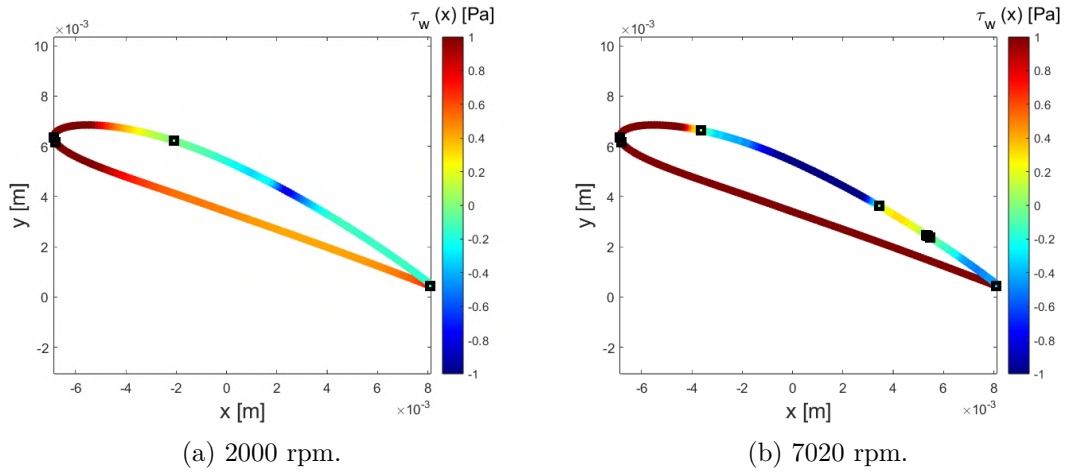


Fig. 4.14 Wall shear stress (x direction) at mid-span.

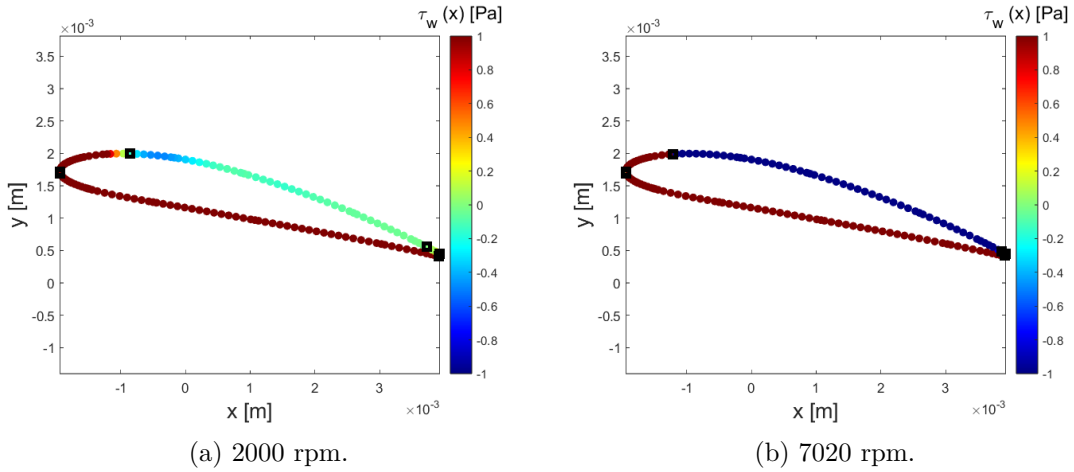


Fig. 4.15 Wall shear stress (x direction) at the tip.

In figures 4.13, 4.14 and 4.15 the black squares represent the locations where the wall shear stress changes sign. A change in sign allows to locate not only the separation of the flow and the reattachment, but also the stagnation point of the airfoil.

Observing figures 4.13 to 4.15 it is possible to recognize some trends. In particular, at low Reynolds (low rotational speed), the flow separates and then it is unable to reattach. On the contrary, for the higher Reynolds number, the flow separates and then reattaches. The extension of the reattachment region depends on the Reynolds number, this is confirmed also by analyzing different rotational speeds. A bigger extension of the reattachment region means a smaller separation bubble and so lower viscous effects. As it can be seen in the figures the flow seems to experience a bigger separation near the tip, this behaviour can be due to the influence of the tip vortex in this particular region of the blade. Another aspect that can be observed is that at the lower Reynolds numbers the separation point on the upper surface is more far away

from the leading edge with respect to the higher Reynolds condition. This behaviour seems to be contradictory; in fact, at higher Reynolds the boundary layer should be more energetic with respect to the low Reynolds condition and so the flow should remain attached for a longer distance before the separation. In this latter condition the boundary layer separation could occur in a laminar condition, but this behaviour cannot be predicted in these analyses because of the turbulence model adopted, in this case full-turbulent. So a possible explanation is that the boundary layers for both low and high Reynolds number are turbulent, but in the high Reynolds condition (higher rotational speed) the adverse pressure gradient is bigger, causing the flow to separate earlier. These considerations are also in agreement with the over prediction of the thrust with respect to the experimental data, in particular at low Reynolds number where a laminar boundary layer could exist, while at higher Reynolds an asymptotic condition is expected to be reached. This is in part confirmed by the behaviour of the  $C_T$  with the Reynolds number, commented in the previous section and with the lower error in thrust and torque prediction with respect to experimental data.

The wider separation region with reducing the Reynolds number it is confirmed by figure 4.16.

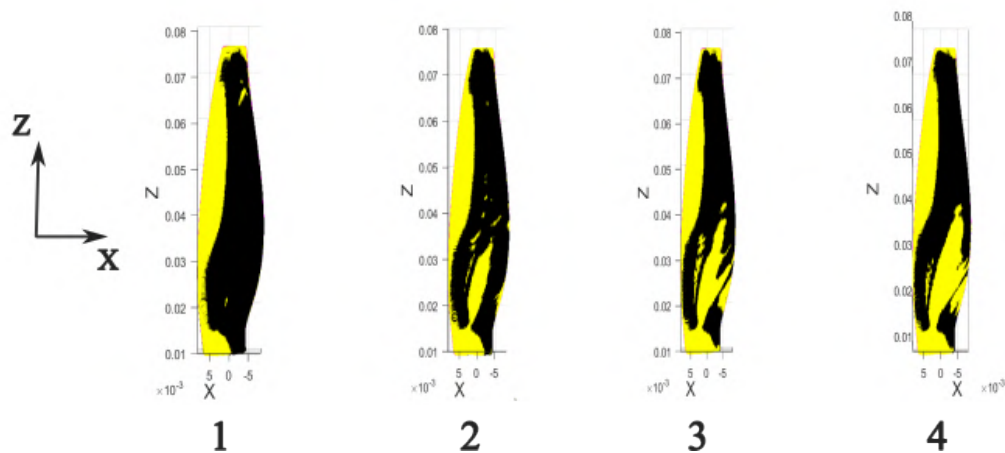


Fig. 4.16 Separated flow region (black) on the upper surface. 1: 2000 rpm, 2: 3610 rpm, 3: 5000 rpm and 4: 7020 rpm.

As it can be seen the area of separated flow, highlighted in black, reduces with increasing the Reynolds number, while the reattachment area increases. This trend confirms the tendency of the  $PL/PL_{id}$  of figure 4.8 to increase with the Reynolds number, until an asymptotic value of 0.5 is reached, indicating a reduction in parasitic drag.

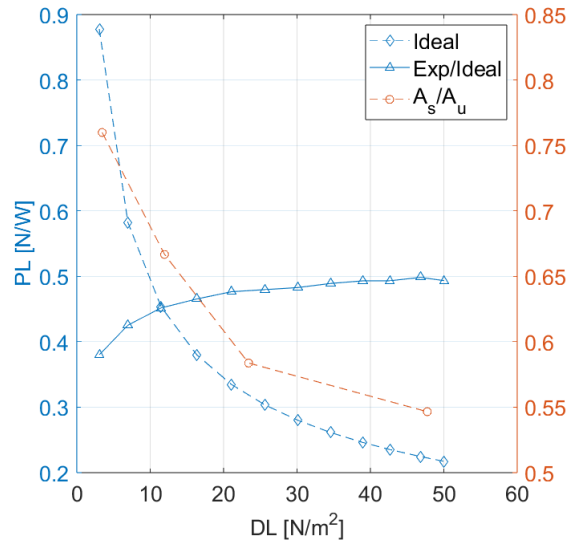


Fig. 4.17 Ratio between separated flow area and total upper surface area ( $A_s/A_u$ ) as a function of disk loading.

In figure 4.17 it is shown the reduction of separated area with respect to the total area of the upper surface increasing the disk loading, i.e the thrust. This reduction in separated flow area could be responsible for the increase of  $PL/PL_{id}$ , indicating a reduction in parasitic drag; this reduction is more pronounced for lower Reynolds, while increasing the Reynolds the curve seems to follow an asymptote, in agreement with previous considerations.

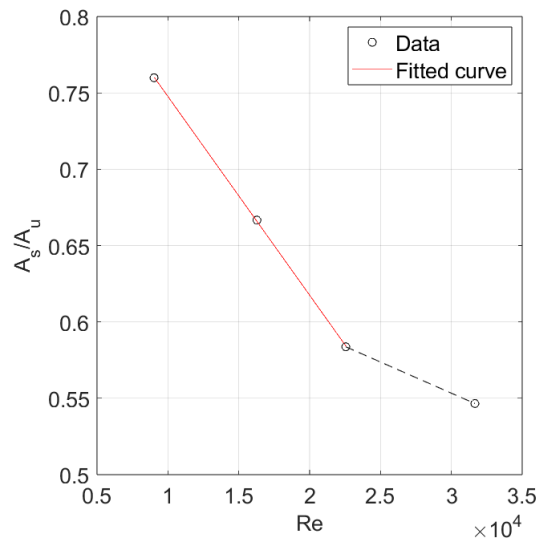


Fig. 4.18  $A_s/A_u$  function of Reynolds number.

Observing figure 4.18, the values of  $A_s/A_u$  follow a linear variation with respect to the Reynolds number in the range 2000-5000 rpm, after that range a non linear behaviour occur.

### 4.2.3 Wake topology

The experimental analysis was carried out at various Reynolds numbers. The aim was to investigate the influence of the Reynolds number on the propeller topology and mean flow field quantities. The analyses were conducted at different rotational speeds, that are 3000, 5000, 7000 and 9000 revolutions per minute. The corresponding Reynolds numbers are listed in table 4.2.

Table 4.2 Test cases in hover.

$\Omega$ [rpm]	$Re$
3000	13530
5000	22550
7000	31571
9000	40591

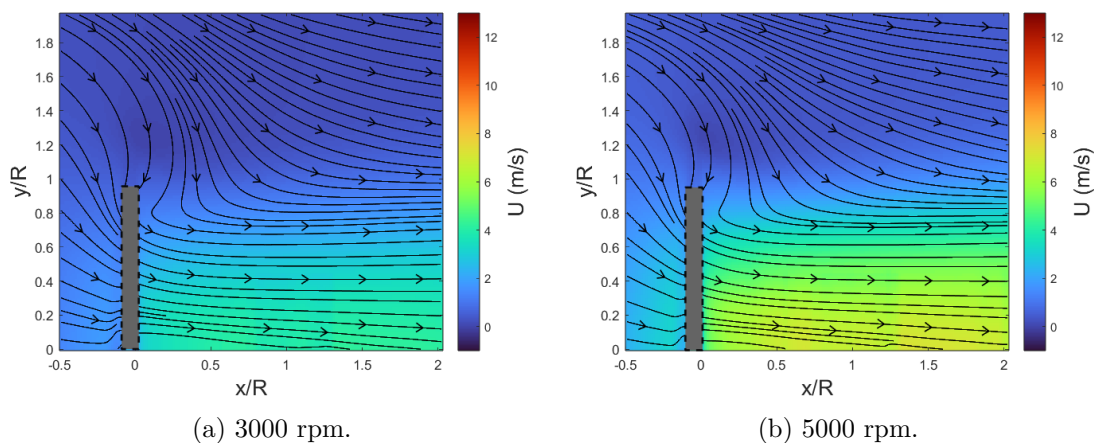


Fig. 4.19 Mean axial velocity flow field (PIV).

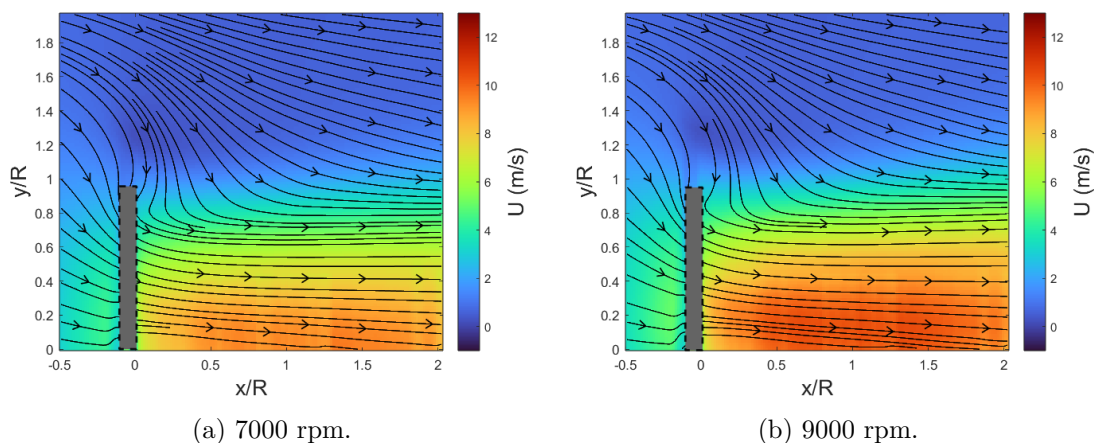


Fig. 4.20 Mean axial velocity flow field (PIV).

Figures 4.19 and 4.20 show the mean axial speed ( $x$  direction) in hover condition at different rotational speed. It is clearly visible (as expected) an increase of the mean axial velocity with increasing the rotational speed of the propeller. Increasing the rotational speed it is also possible to notice an increase in suction due to the higher pressure difference across the propeller disk. Observing the  $U$  velocity profiles for different  $x/R$  values (figures 4.21 and 4.22) we can see an increase in  $y/R$  with increasing  $x/R$  and so, physically, an increase in the transverse dimension of the wake, whereas the rotational speed seems to not have an influence on the wake transverse dimension.

Examining more in detail the velocity profiles, we can see that the maximum velocity in the  $x/R$  direction is not directly proportional to the  $x/R$  coordinate. In fact, we can see a maximum for  $x/R = 1$  and for  $y/R$  between 0.3 and 0.4. Computing the axial velocity with respect to  $x/R$  for a fixed  $y/R$  position, as in figure 4.23, we can see that the axial velocity grows until  $x/R = 1$  and then slowly decreases far in the wake.

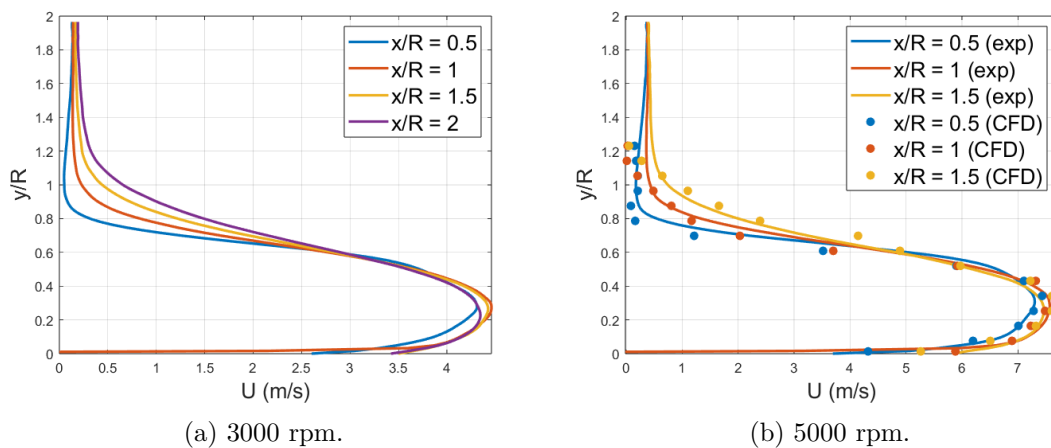


Fig. 4.21 Mean axial velocity profiles.

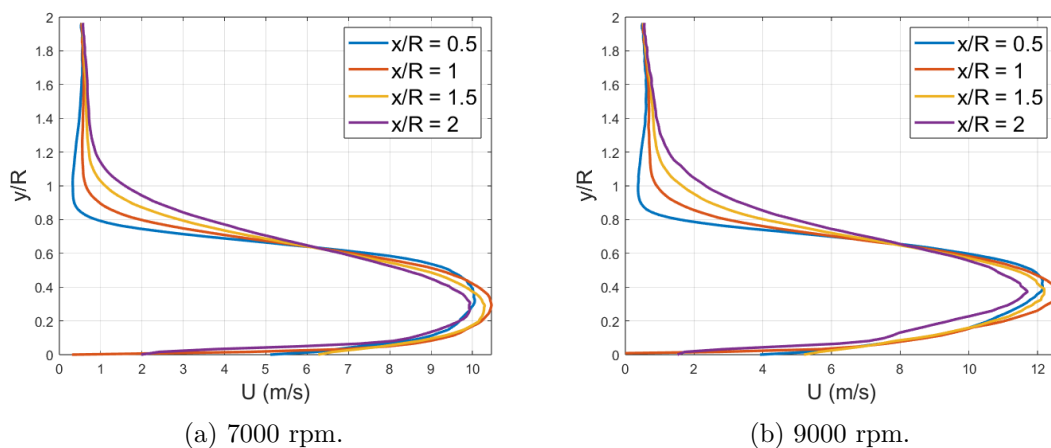


Fig. 4.22 Mean axial velocity profiles.

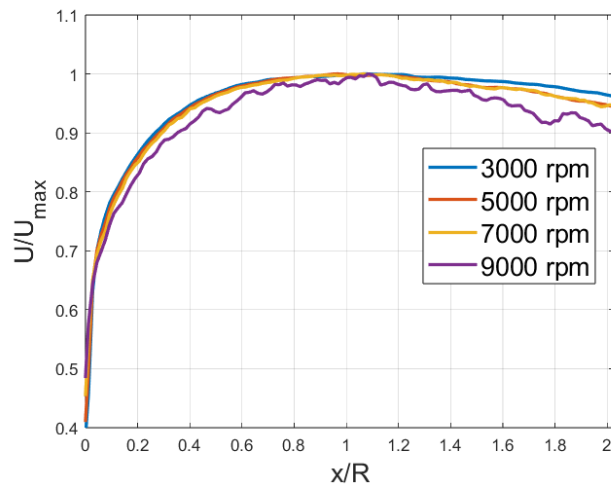


Fig. 4.23  $U/U_{max}$  as a function of  $x/R$  for a fixed  $y/R$  coordinate equal to 0.3.

This behaviour in the axial speed can be attributed to the effect of the wake contraction in the *near wake* region. In fact, due to the momentum conservation, if the wake reduces its width the velocity should increase. On the contrary, after  $x/R = 1$  the wake become wider and so the velocity decreases. Another factor that could affect the induced velocity in the wake is the tip vortex. It is possible that after a certain distance downstream in the wake, the tip vortex reduces its strength, and so induces a smaller velocity in the wake, until it dissipates causing the wake to grow in size. These considerations can be supported by analyzing the vorticity out of the plane  $\omega_z$ , the Reynolds shear stress  $\overline{u'v'}$  and the turbulent kinetic energy in the wake  $E_k$ .

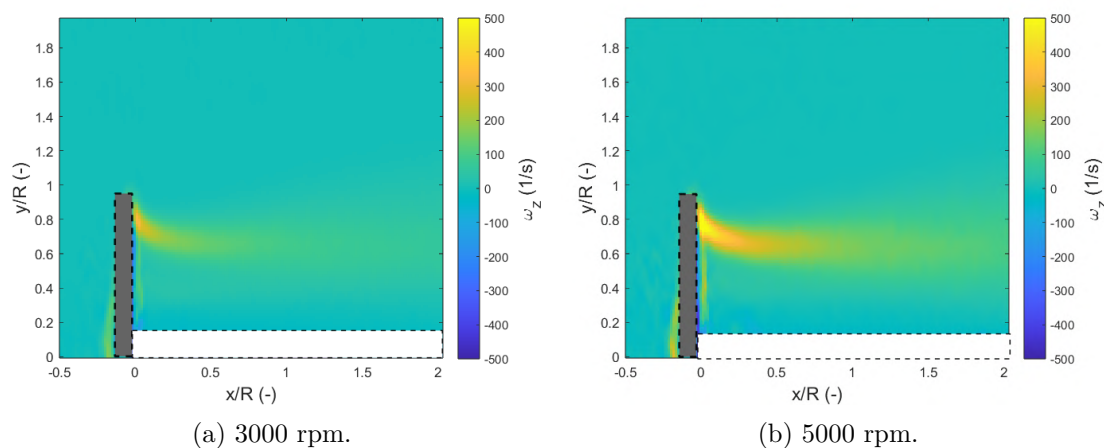


Fig. 4.24 Mean out of plane vorticity field (PIV).

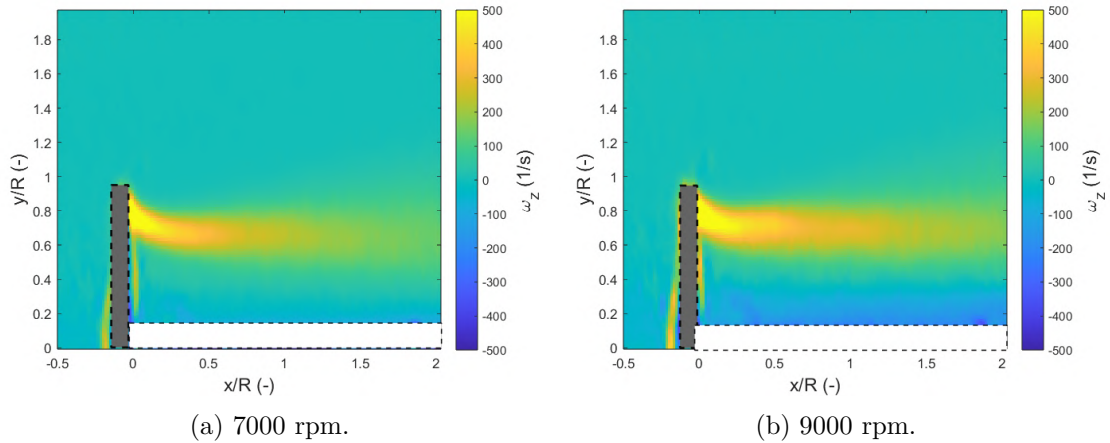


Fig. 4.25 Mean out of plane vorticity field (PIV).

Observing the vorticity distributions in figures 4.26 and 4.27, the vorticity magnitude increases with the rotational speed, due to the increase in strength of the tip vortex. The vorticity peak, for all of the tested rotational speeds it is close to the blade, where the tip vortex is formed and then the magnitude decreases with increasing the downstream distance due to the breakdown and then the dissipation of these structures.

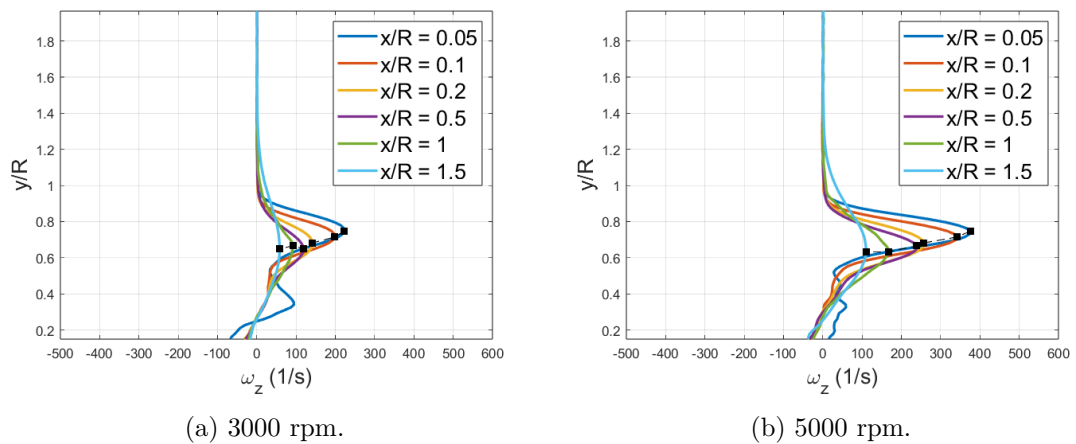


Fig. 4.26 Mean out of plane vorticity profiles. Black square represent the maximum vorticity.

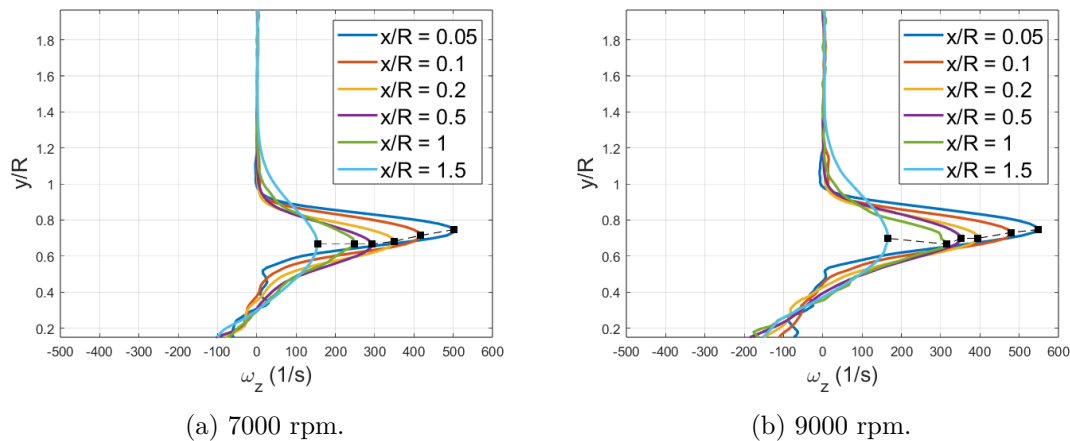


Fig. 4.27 Mean out of plane vorticity profiles. Black square represent the maximum vorticity.

Figures 4.26 and 4.27 better explain the wake topology and the evolution of the tip vortices downstream in the wake. For all of the rotational velocities analyzed and close to the propeller disk ( $X/R = 0.05$ ), a local maxima of positive vorticity  $\omega_z$  is located at approximately 80% of the blade radius. This result is an evidence of a zone where the tip vortex remains for a longer time, until the next blade passes, causing the vortex to convect downstream. This hypothesis can also explain the increase in  $C_T$  for that portion of the blade, as previously explained and shown in figure 4.4. Observing the vorticity profiles it is possible to notice a region of negative vorticity, this can be caused by the vortex sheet shed by the inner part of the blade, the hub and by the presence of the rotor support.

Increasing  $x/R$  the positive vorticity peak reduces its value due to the evolution of the tip vortex in the wake, which loses strength. The reduction in vorticity is accompanied by a shift of the vorticity peak at lower  $y/R$ , as expected.

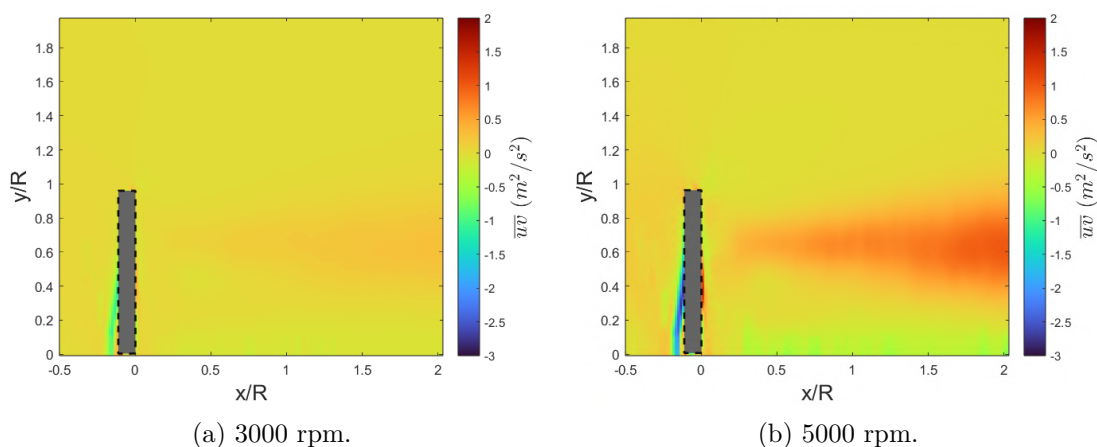


Fig. 4.28 Reynolds stresses (PIV).

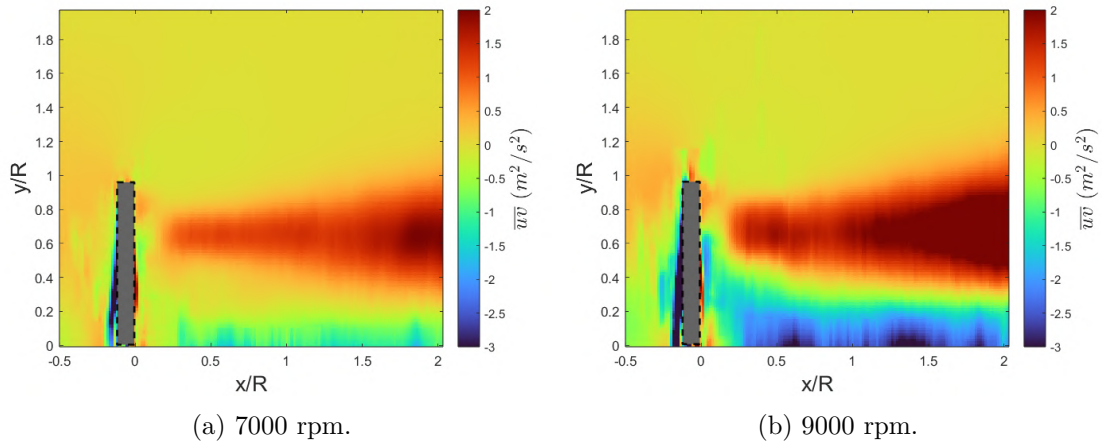


Fig. 4.29 Reynolds stresses (PIV).

As it can be seen in figures 4.28 and 4.29, an increase in rotational speed corresponds to an increase in the  $\overline{u'v'}$  component of the Reynolds stress tensor. Larger values of shear stress are located in the shear layer region. Increasing the distance from the propeller disk  $\overline{u'v'}$  increases. This behaviour is opposite to what was observed for the mean vorticity  $\omega_z$ , and makes one think that the tip vortex, evolving downstream, becomes unstable and eventually experiences a break down that increases the turbulence in the wake. In fact, even so the turbulence is a phenomenon characterized by high vorticity fluctuations, the mean vorticity can approach a null value. The increase in rotational speed has the effect of an higher  $\overline{u'v'}$  magnitude due to the fact that the tip vortices are more energetic with respect to low rotational speeds, and so, when they break up the turbulence is characterized by more severe velocity fluctuations.

## 4.3 Axial inflow performance

In this section the performance of the propeller with axial velocity inflow of 3 m/s, 6 m/s and 9 m/s will be investigated and compared with respect to the hovering condition. Here, the axial freestream velocity will be denoted with  $U_\infty$ .

### 4.3.1 Thrust and Torque

Figure 4.30 shows the  $C_T$  and  $C_Q$  as a function of the advance ratio, defined as:

$$J = \frac{U_\infty}{\Omega/60 \cdot D} \quad (4.16)$$

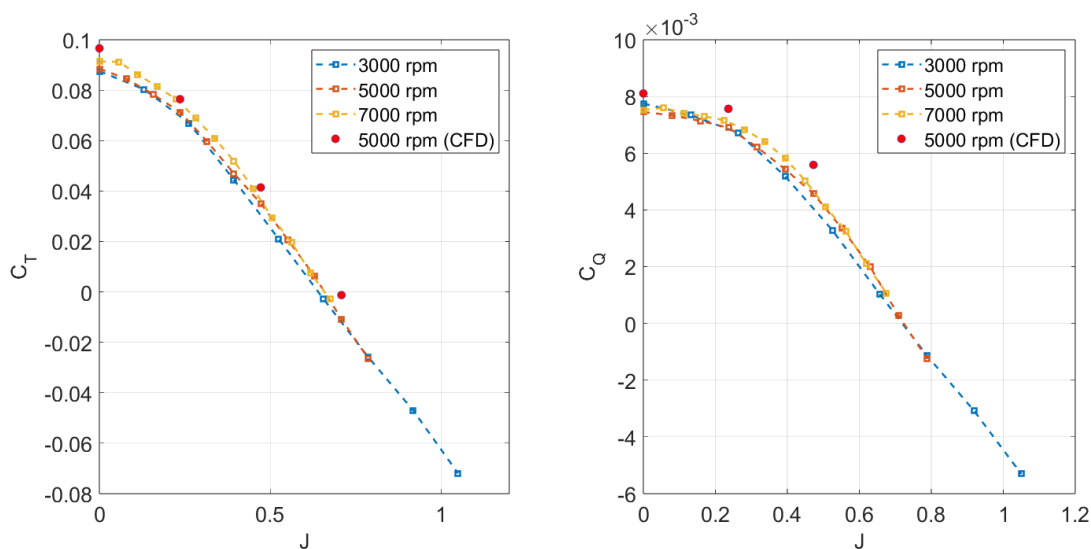


Fig. 4.30 Thrust and torque coefficients as a function of the advance ratio.

From the figure it can be seen the influence of the advance ratio on the  $C_T$  and  $C_Q$  of the propeller and the effect of the Reynolds number. Increasing the Reynolds number the  $C_T$  increases almost constantly with increasing  $J$ . On the contrary, the effect of the Reynolds on the  $C_Q$  is that for low advance ratios an increase in the  $Re$  causes a reduction in  $C_Q$ , but for higher advance ratios the tendency is the opposite. As discussed for the hover performance, an increase in the Reynolds number causes an increase in the lift coefficient and a decrease for the drag coefficient. Both of these contributes are benefical for increasing the  $C_T$ . For the torque coefficient, a decrease in drag coefficient is benefical, while an increase in lift coefficient is not. Observing figure 4.30 (right) it is possible to assume that at low advance ratios the decrease in drag coefficient, increasing the Reynolds number, is greater with respect to higher

advance ratios and the increase in lift is smaller at low advance ratios with respect to higher  $J$ . With these considerations one can conclude that at low advance ratios an increase in the Reynolds number is beneficial for the power consumption, but this is not true at high advance ratios. For a better comprehension of the phenomenon, the efficiency of the propeller with respect to  $J$ , at various  $Re$ , is shown in figure 4.31. The efficiency of a propeller is defined as:

$$\eta = \frac{C_T}{C_P} J \quad (4.17)$$

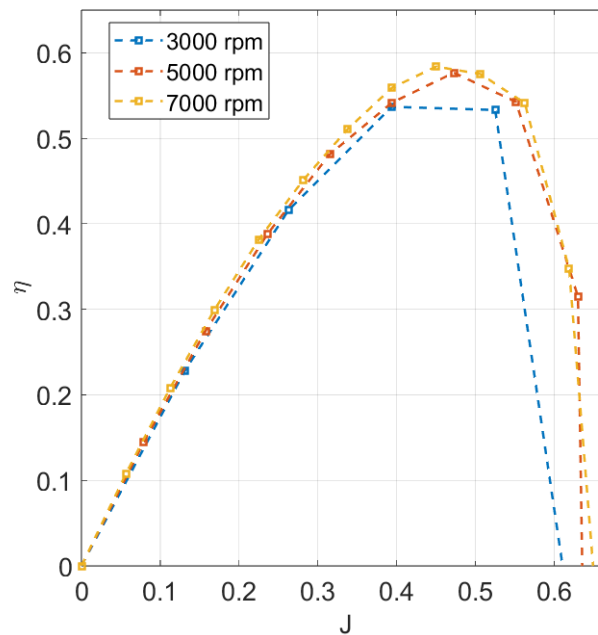


Fig. 4.31 Efficiency of the propeller.

For high advance ratios the effect of the Reynolds number is more remarkable, the high Reynolds condition lead to a more efficient propeller. This behaviour can be attributed to increase in thrust, that overcome the increase in torque. For  $\eta = 0$  the curves cut the axis in order from lower to higher Reynolds. This is due to the ability of the high Reynolds propeller to produce higher  $C_T$  at higher advance ratios. Figure 4.32 shows the  $C_T$  and  $C_Q$  distribution along the blade radius. Increasing  $J$ , the maximum  $C_T$  reduces its value and shifts inboard of the blade. This shift could be caused by a different inflow distribution and by the fact that the tip vortex is convected more rapidly in the wake. A similar behaviour it's observed for the  $C_Q$  distribution. The reduction in  $C_T$  and  $C_Q$  can be attributed to a reduction in  $C_L$  and  $C_D$  caused by an increase in the inflow angle  $\phi$  in figure 4.3 and so a reduction in angle of attack  $\alpha$ . These consideration are also supported observing the static pressure distribution on the upper surface of the blade, in fact as can be seen in

figure 4.33, increasing  $J$  the static pressure decreases in module, causing a reduction in  $\Delta p$  across the propeller disk.

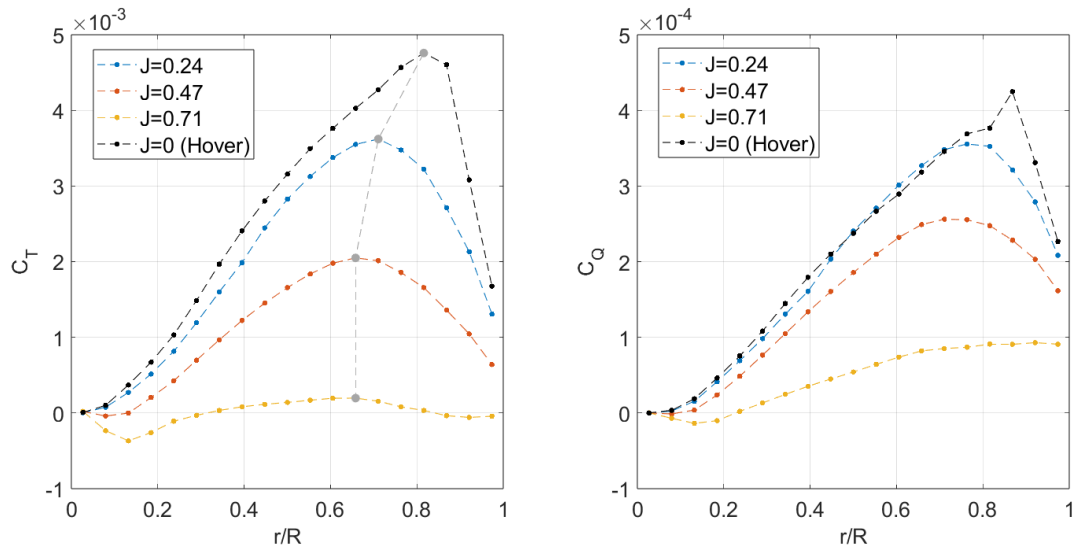


Fig. 4.32 Thrust and torque coefficients along the blade as a function of the advance ratio (CFD).

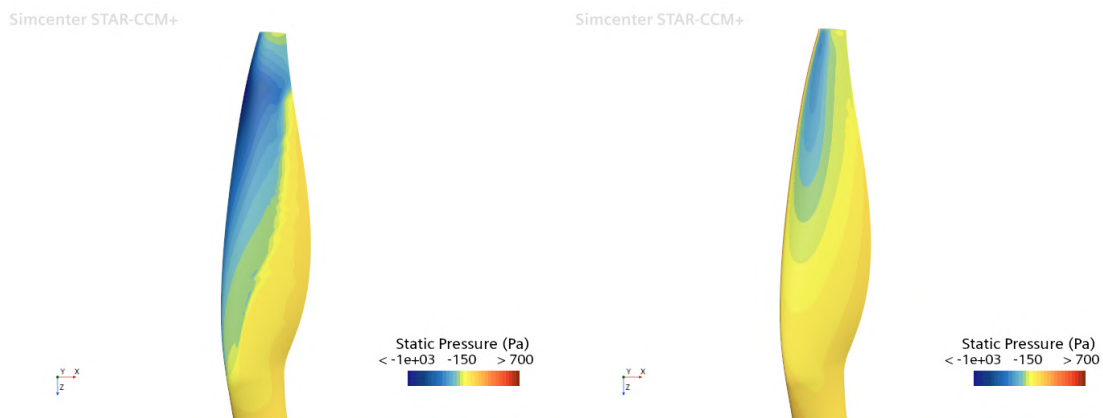


Fig. 4.33 Thrust and torque coefficients along the blade as a function of the advance ratio (CFD).

For supporting the considerations above the  $C_l$  and  $C_d$  distribution along the blade has been calculated, as already done for the hovering case. The method used for the estimation of the inflow angle  $(\phi + \alpha_i)$  is the same presented in the hovering section.

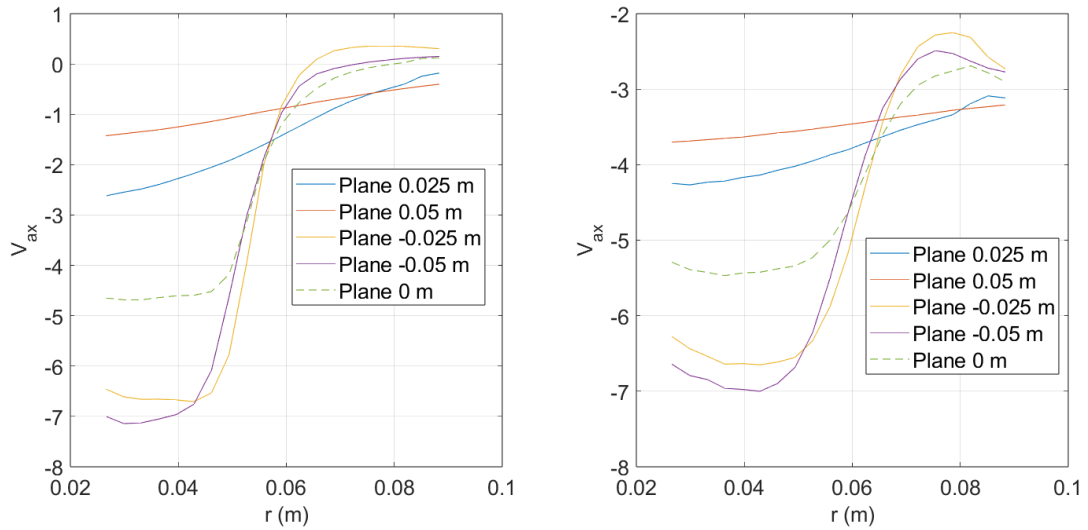


Fig. 4.34 Axial velocity interpolation, hover (left),  $J=0.24$  right.

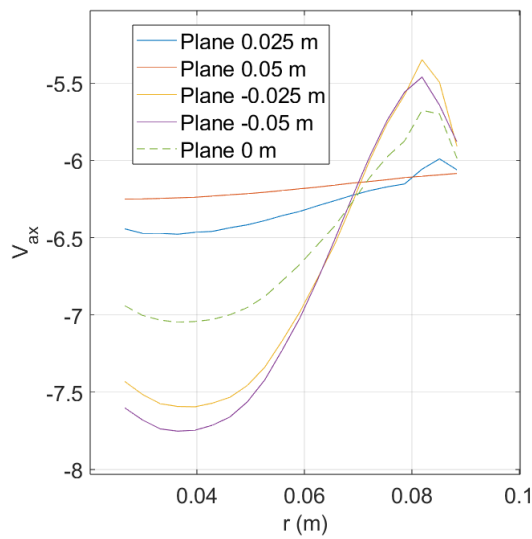


Fig. 4.35 Axial velocity interpolation,  $J=0.47$ .

Figures 4.34 and 4.35 show the results of the interpolation. The axial velocity distribution at the disk then has been used for computing the inflow angle  $\phi + \alpha_i$ . The distribution of the inflow angle along the blade semi-span is reported in figure 4.36

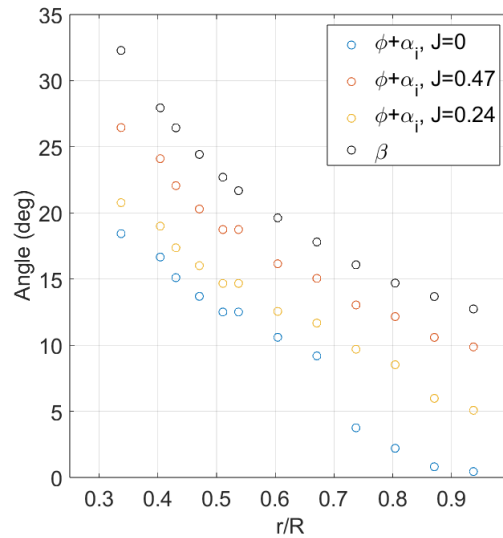


Fig. 4.36 Inflow angle

As can be seen,  $\phi + \alpha_i$  increases with  $J$ , and so the incidence decreases. Furthermore, the angle  $\phi + \alpha_i$  follows the trend of  $\beta$ , that's because increasing the distance from the hub the local tangential velocity ( $\Omega r$ ) increases and so the effect is to reduce the angle  $\phi + \alpha_i$ . Once  $\phi + \alpha_i$  is computed, the  $C_l$  and  $C_d$  along the blade are easy to calculate.

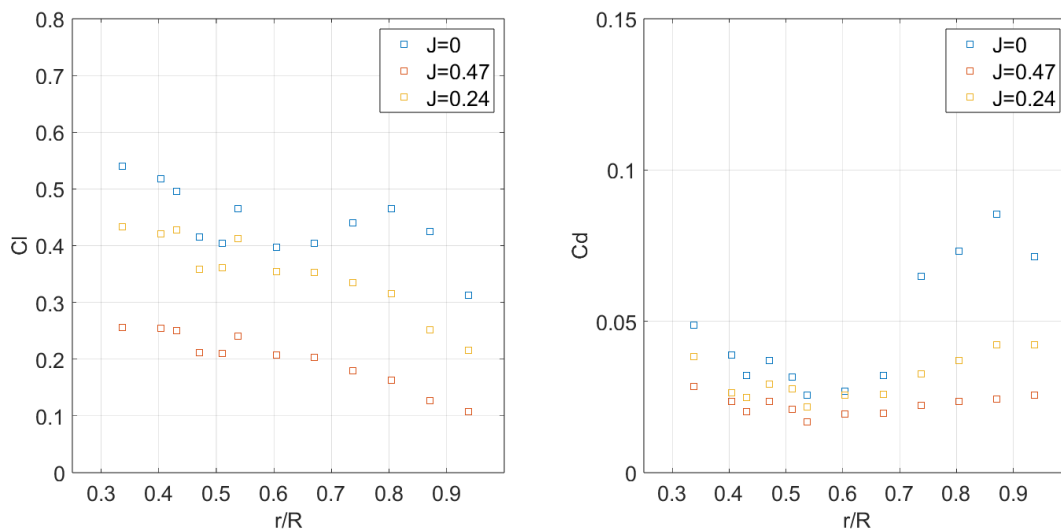


Fig. 4.37  $C_l$  and  $C_d$  distributions along the blade span for different  $J$ .

Figure 4.37 shows the  $C_l$  and  $C_d$  distribution on the blade semi-span. Increasing  $J$ , both  $C_l$  and  $C_d$  decrease, this could justify the trend of  $C_T$  and  $C_Q$  in figure 4.30. The reduction in  $C_l$  and  $C_d$  are justified by the increase in  $\phi + \alpha_i$  with  $J$ , which causes a reduction in incidence of the airfoil. Another important noticeable aspect

it is the local peak in  $C_t$  at 80% of the propeller radius in the hovering case. This can be attributed to the increase in incidence due to the upwash induced by the tip vortex. This could be observed also in figure 4.34 (left), where a positive velocity near the tip is present.

For a better comprehension of the physical phenomenon responsible of the trends reported above, the wall features will be discussed. The next subsection presents the results obtained by CFD. Although when looking at the graphs above, the numerical data deviates from the experimental data, CFD and experiments report the same trend; this could mean that the physical phenomenon is the same.

### 4.3.2 Wall flow features

Figures 4.38 and 4.39 shows the wall shear stress in x-direction for different advance ratio at 5000 rpm. As can be seen, the advance ratio has a beneficial effect on flow separated regions, with a reduction in separated flow area ( $A_s$ ) increasing  $J$ .

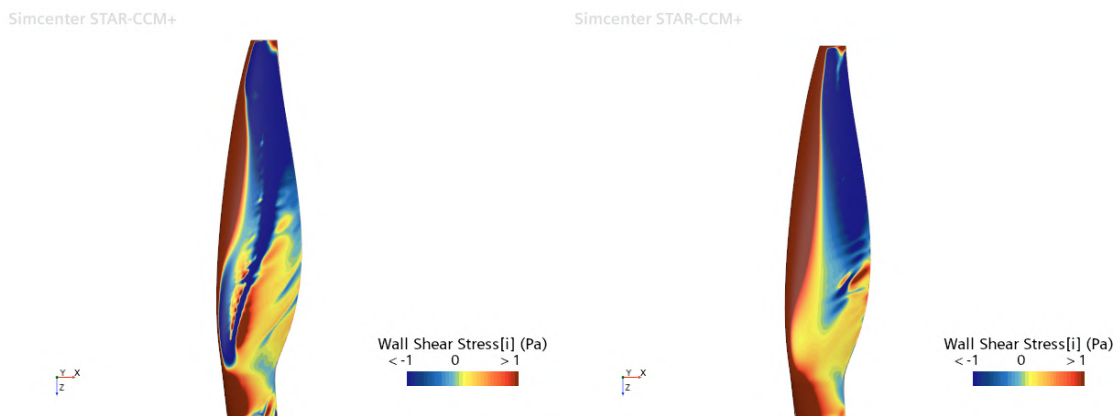


Fig. 4.38 Wall shear stress for  $J=0$  (left) and  $J=0.24$  (right) at 5000 rpm.

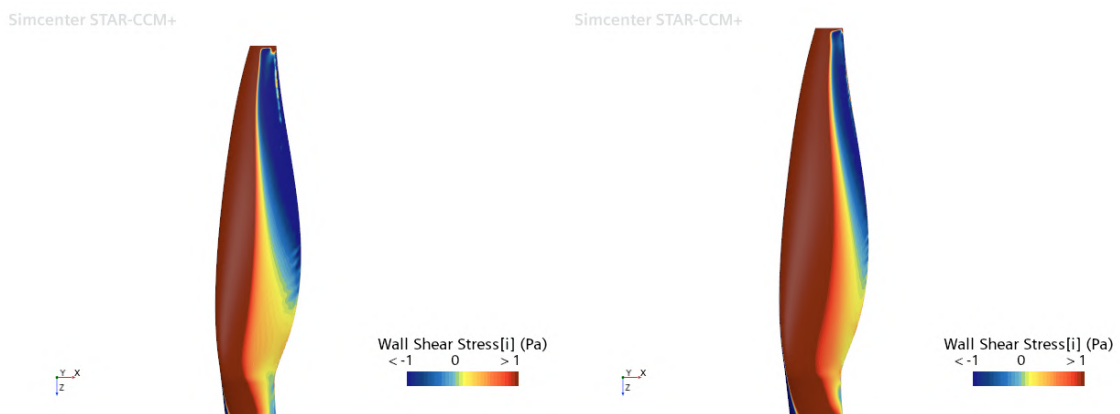


Fig. 4.39 Wall shear stress for  $J=0.47$  (left) and  $J=0.71$  (right) at 5000 rpm.

So, in terms of power consumption, an increase in  $J$  reduces the separated flow regions on the blade surface, this has the effect of a reduction in drag and so in torque, as explained previously. Figure 4.40 shows the trend of reduction in separated area for different  $J$  at fixed rotational speed, while figure 4.41 shows the ratio  $A_s/A_u$  (separated area/upper surface area) with respect to  $J$ . On the same diagram it is reported the  $C_Q$  as a function on  $J$ , which has a similar trend of  $A_s/A_u$ , reinforcing the idea of a decrease in  $C_D$  and  $C_L$  caused by a bigger inflow angle.

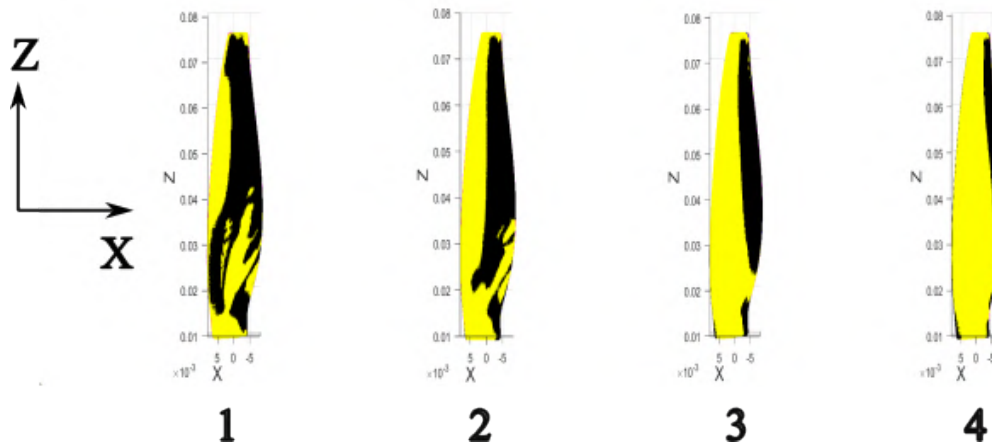


Fig. 4.40 Separated flow regions (black) at 5000 rpm. 1:  $J=0$ , 2:  $J=0.24$ , 3:  $J=0.47$ , 4:  $J=0.71$ .

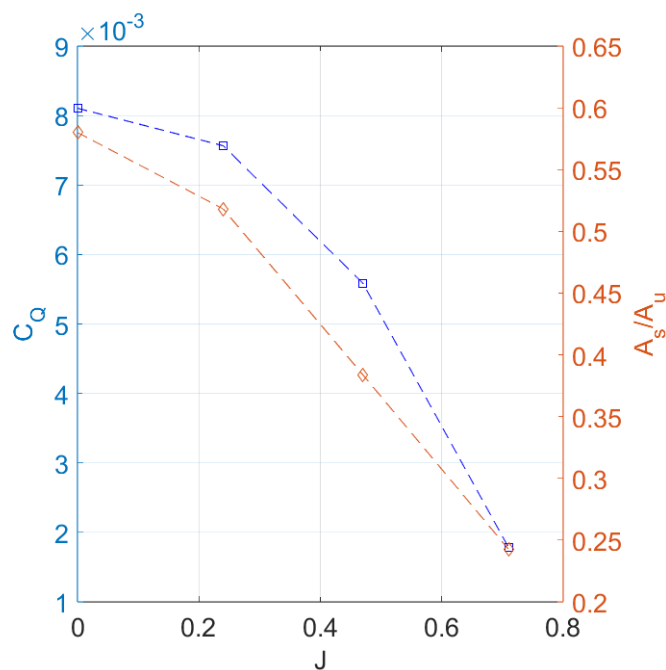


Fig. 4.41 Effect of  $J$  on separated flow regions and  $C_Q$ .

## 4.4 Cross-flow performance

### 4.4.1 Wake topology

In this section the wake topology of the propeller in cross-flow conditions was investigated by means of PIV. Figures 4.42 and 4.43 shows the mean axial velocity fields obtained experimentally with 1 m/s of cross-flow. The effect of the cross-flow velocity is to distort the wake, the distortion is more pronounced for low rotational velocities, that's because in these conditions the cross-flow velocity is of the same order of magnitude of the maximum velocity in the wake.

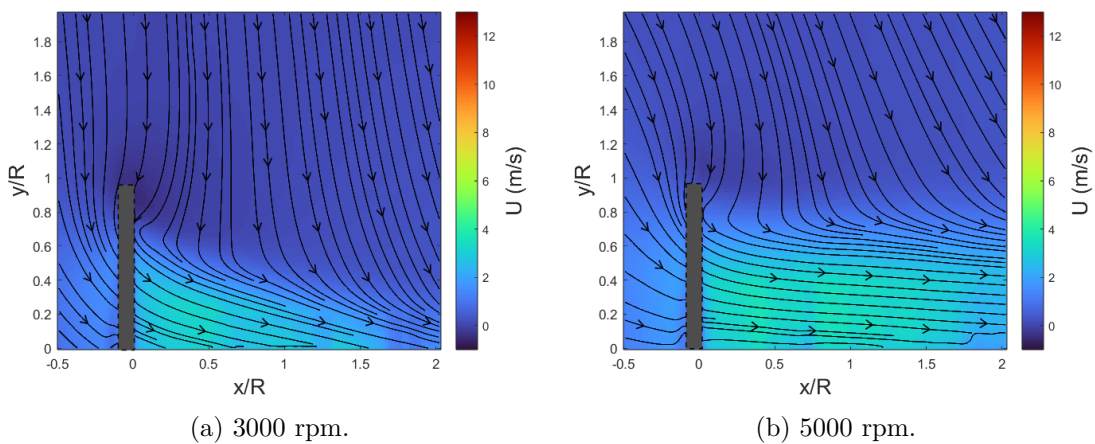


Fig. 4.42 Mean axial velocity flow field (PIV), 1 m/s cross-flow.

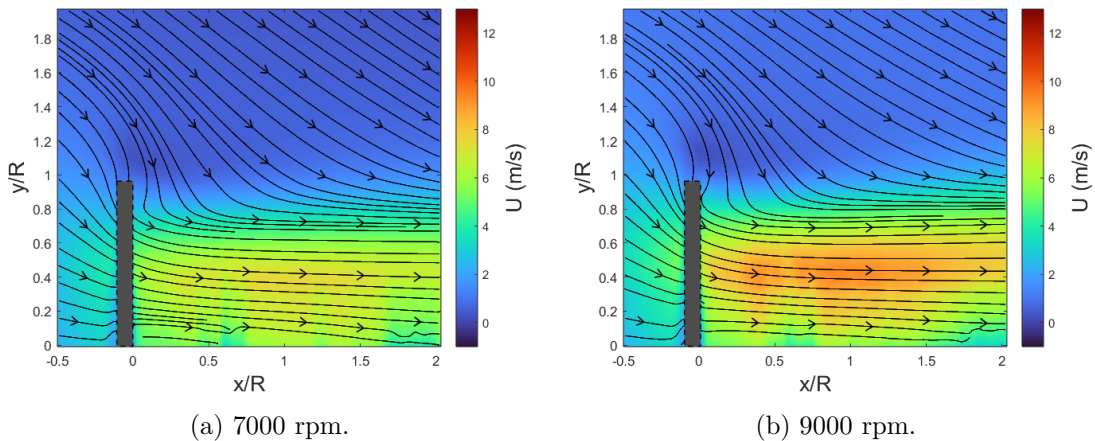


Fig. 4.43 Mean axial velocity flow field (PIV), 1 m/s cross-flow.

With respect to the hovering case, the maximum velocity in the wake is lower in magnitude. This behaviour can be attributed to the non symmetric inflow condition of the two blades, this condition could cause a reduction in  $\Delta p$  across the propeller disk. So, the effect of the cross-flow is double: a distortion of the wake and a

reduction in mean axial velocity by a decreased  $\Delta p$ , in fact, the reduction of mean axial velocity could not be attributed to fluid dynamics effects inside of the wake, because the wake itself (the stream tube) it is not permeable to external flow.

Increasing the cross-flow velocity, all of these effects become more pronounced, as shown in figure 4.44 and 4.45. For a better comprehension of the wake topology variation with respect to the cross-flow velocities, the velocity profiles of mean axial velocity in the wake has been reported in figure 4.46 and 4.47, with respect to the hovering case (dashed line).

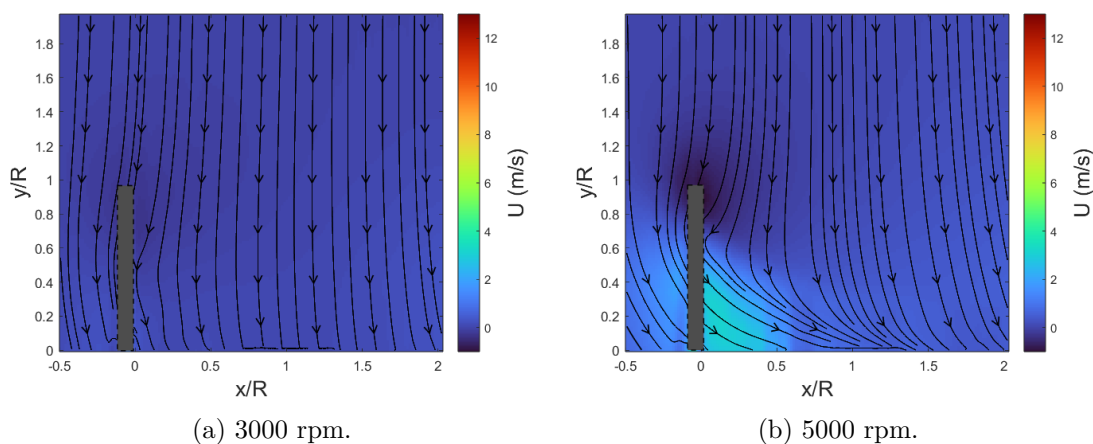


Fig. 4.44 Mean axial velocity flow field (PIV), 3 m/s cross-flow.

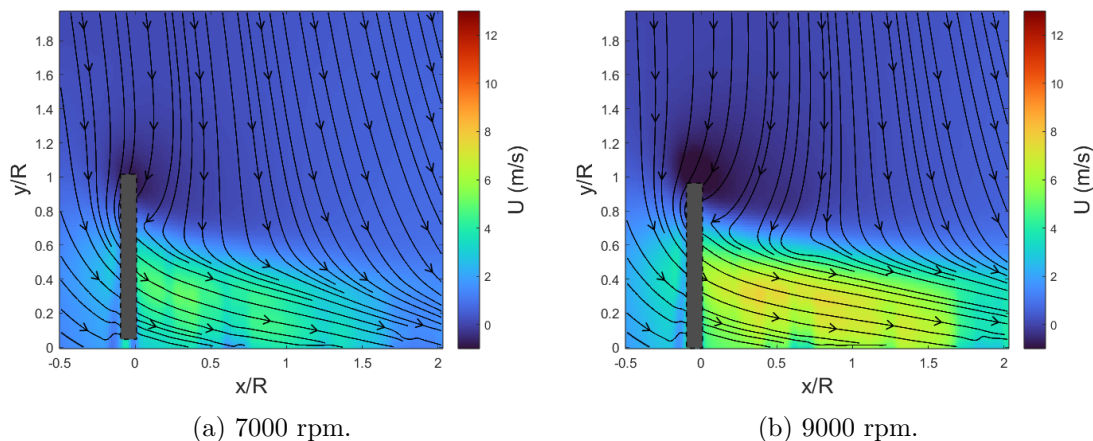


Fig. 4.45 Mean axial velocity flow field (PIV), 3 m/s cross-flow.

Observing the velocity profiles, the hypothesis of a non-permeable wake is partially confirmed by the fact that the profiles have a similar trend with respect to the hovering case (black dashed lines).

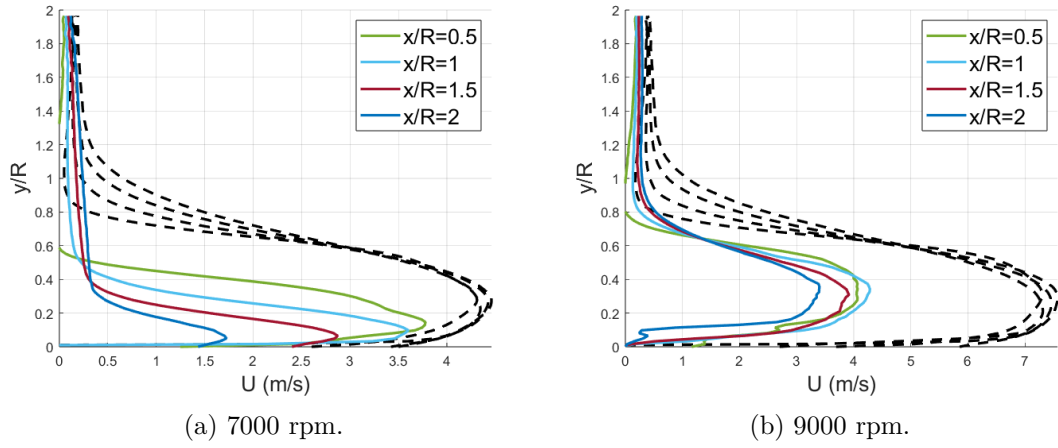


Fig. 4.46 Mean axial velocity profiles, 3 m/s cross-flow.

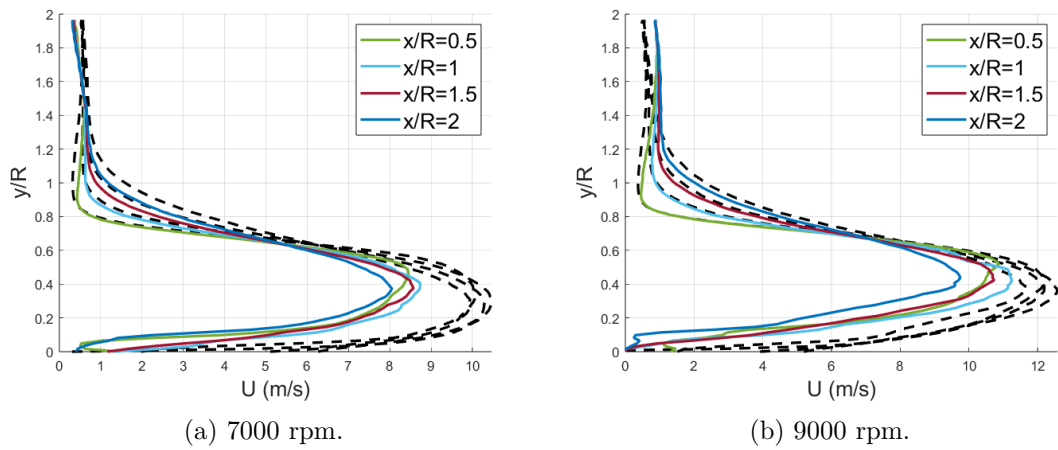


Fig. 4.47 Mean axial velocity profiles, 3 m/s cross-flow.

# Chapter 5

## Conclusions

In this thesis, the effect of the Reynolds number and the advance ratio on the performance of a small-scaled propeller has been studied both experimentally and numerically. We have seen that decreasing the Reynolds number, the propeller experiences a performance degradation due to the increase in parasitic drag. The numerical data are in agreement with the experimental ones, with an error on thrust and torque prediction that increases reducing the Reynolds number. The higher error with respect to experimental data at low Reynolds numbers underline the limitations of using a Fully-turbulent model in regimes where the boundary layer on the blade could be partially laminar; for this reason a Transitional model could provide more accurate results.

# References

- [1] Hassanalian and Abdelkefi. Classifications, applications, and design challenges of drones: A review. *Progress in aerospace sciences*, 91:99–131, 2017.
- [2] Yoon, Diaz, Boyd, Chan, and Theodore. Computational aerodynamic modeling of small quadcopter vehicles. *AHS Forum* 73, 2017.
- [3] Komerath, Smith, and Tung. A review of rotor wake physics and modeling. *Journal of the American Helicopter Society*, 56:022006, 2011.
- [4] John Seddon. *Basic Helicopter Aerodynamics*. John Wiley Sons, 2010.
- [5] Landgrebe. The wake geometry of a hovering helicopter rotor and its influence on rotor performance. Annual National Forum of the American Helicopter Society, 1972.
- [6] Leishman. Measurements of the aperiodic wake of a hovering rotor. *Experiments in Fluids*, 25:352–361, 1998.
- [7] Bohorquez, Samuel, Sirohi, Pines, and Rudd. Design, analysis and hover performance of a rotary wing micro air vehicle. 2003.
- [8] Winslow, Otsuka, Govindarajan, and Chopra. Basic understanding of airfoil characteristics at low reynolds numbers. *Journal of Aircraft*, 2017.
- [9] Bohorquez and Pines. Hover performance of rotor blades at low reynolds numbers for rotary wing micro air vehicles. 2nd AIAA "Unmanned Unlimited" Systems, Technologies, and Operations — Aerospace, 2003.
- [10] Ramasamy, Johnson, and Leishman. Understanding the aerodynamic efficiency of a hovering micro-rotor. American Helicopter Society International Specialists' Meeting on Unmanned Aerial Vehicles, 2008.
- [11] Smirnov and Menter. Sensitization of the sst turbulence model to rotation and curvature by applying the spalart–shur correction term. *Journal of Turbomachinery*, 131:041010–1, 2009.
- [12] Gordillo, Santos, Mejia, Collazos, and Escobar. Numerical and experimental estimation of the efficiency of a quadcopter rotor operating at hover. *Energies*, 12:261, 2015.
- [13] Louriero, Oliveira, Hallak, Bastos, Rocha, Delmonte, and Lemonge. Evaluation of low fidelity and cfd methods for the aerodynamic performance of a small propeller. *Aerospace Science and Technology*, 108:106402, 2021.
- [14] Deters, Ananda, and Selig. Reynolds number effects on the performance of small-scale propellers. American Institute of Aeronautics and Astronautics, 2014.

- 
- [15] Guntur and Sorensen. An evaluation of several methods of determining the local angle of attack on wind turbine blades. *Journal of physics: Conference series*, 2014.
- [16] Lee, Leishman, and Ramasamy. Fluid dynamics of interacting blade tip vortices with a ground plane. *Journal of the American Helicopter Society*, 55:022005, 2010.
- [17] Ayamga, Akaba, and Nyaaba. Multifaceted applicability of drones: A review. 2021.
- [18] Prothin, Fernandez Escudero, Douè, and Jardin. Aerodynamics of mav rotors in ground and corner effect. *International Journal of Micro Air Vehicles*, 11:1–13, 2019.
- [19] NASA, McKinsey & Company, Ascension Global, Crown Consulting, and Georgia Tech. Urban air mobility (uam) market study. NASA report, 2018.
- [20] Young. Conceptual design aspects of three general sub-classes of multi-rotor configurations: Distributed, modular, and heterogeneous. NASA technical report, 2015.
- [21] McAlister. Rotor wake development during the first revolution. Annual National Forum of the American Helicopter Society, 2004.
- [22] Hein and Chopra. Hover performance of a micro air vehicle: Rotors at low reynolds number. e International Specialists’ Meeting Unmanned Rotorcraft: Design, Control and Testing, 2007.
- [23] Strawn, Caradonna, and Duque. 30 years of rotorcraft computational fluid dynamics research and development. Annual National Forum of the American Helicopter Society, 2005.
- [24] Gordillo, Escobar, and Mejia. Influence of the reynolds number on the aerodynamic performance of a small rotor. *Aerospace*, 10:130, 2023.
- [25] Stajuda, Karczewki, Obidowski, and Jozwik. Development of a cfd model for propeller simulation. *Mechanics and Mechanical Engineering*, 20:579–593, 2016.
- [26] Willhelm. Rotating flow simulations with openfoam. *International Journal of Aeronautical Science Aerospace Research (IJASAR)*, S1:001:1–7, 2015.
- [27] Liu, Lin, and Purimitla. Wake field studies of tidal current turbines with different numerical methods. *Ocean Engineering*, 117:383–397, 2016.
- [28] Tourn, Pallarès, Cuesta, and Paulsen. Characterization of a new open jet wind tunnel to optimize and test vertical axis wind turbines. 2017.



# Appendix A

## Images

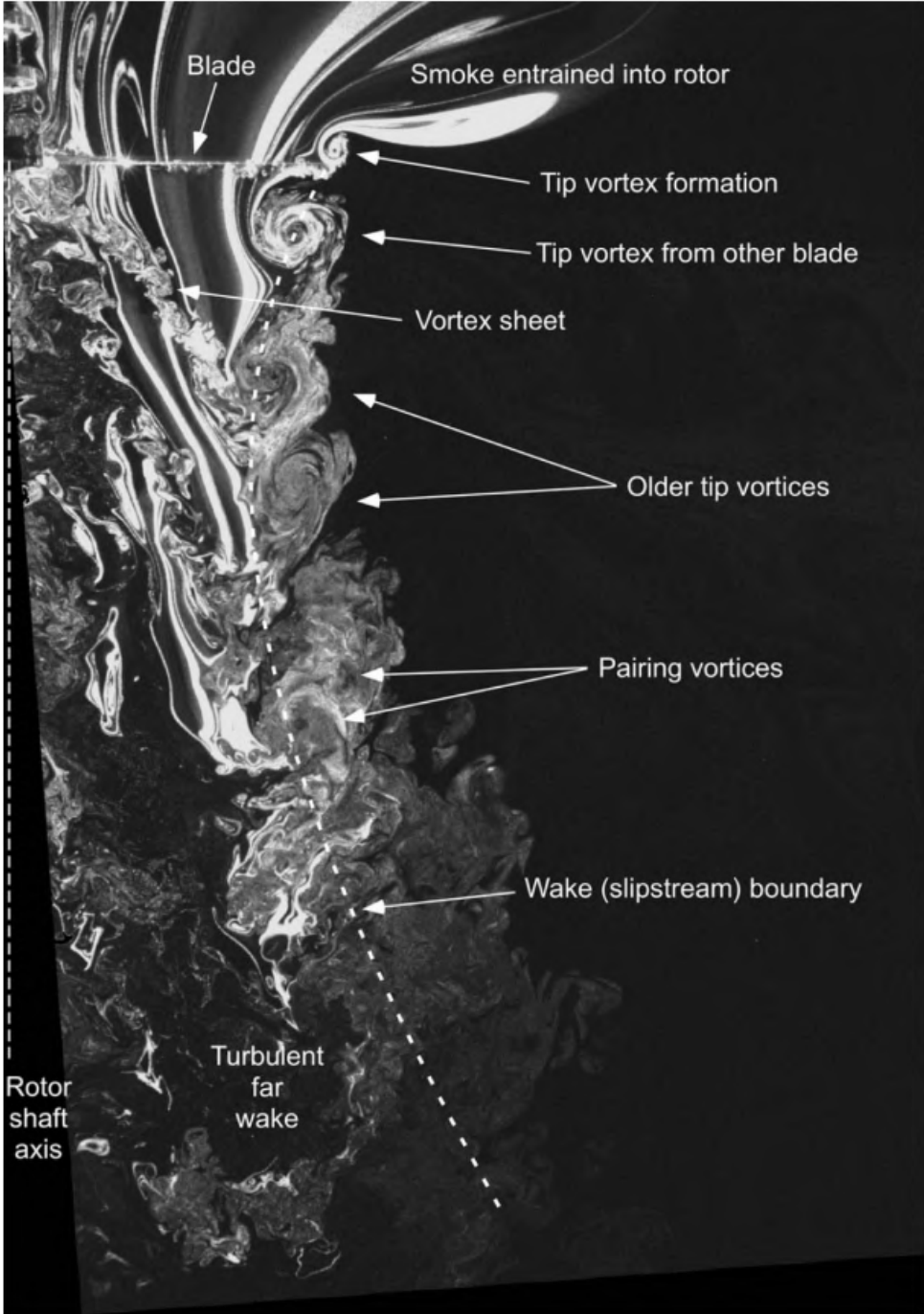


Fig. A.1 Representative flow visualization of the rotor wake in hover [16].